

COLD ATOMS IN DISSIPATIVE OPTICAL LATTICES

G. GRYNBERG, C. ROBILLIARD



ELSEVIER

AMSTERDAM – LONDON – NEW YORK – OXFORD – PARIS – SHANNON – TOKYO



ELSEVIER

Physics Reports 355 (2001) 335–451

PHYSICS REPORTS

www.elsevier.com/locate/physrep

Cold atoms in dissipative optical lattices

G. Grynberg^{a,*}, C. Robilliard^b

^a*Laboratoire Kastler Brossel, Département de Physique de l'Ecole Normale Supérieure,
24 rue Lhomond, F-75231 Paris Cedex 05, France*

^b*Laboratoire Collisions, Agrégats, Réactivité, IRSAMC, Université Paul Sabatier,
118 Route de Narbonne, F-31062 Toulouse Cedex 4, France*

Received October 2000; editor: J. Eichler

Contents

1. Introduction	337	5.1. General considerations on probe transmission	383
2. A classical approach to optical lattices	338	5.2. Raman transitions between eigenstates of the light-shift Hamiltonian	384
2.1. Atom with an elastically bound electron in a standing wave	339	5.3. Raman transitions associated with the vibrational motion	385
2.2. One-dimensional lattices	340	5.4. Propagating excitation. The Brillouin-like resonance	392
2.3. Two-dimensional periodic lattices	342	5.5. Stimulated Rayleigh resonances—relaxation of nonpropagative modes	395
2.4. Quasiperiodic lattices	348	5.6. Coherent transients—another method to study the elementary excitations	398
2.5. Three-dimensional lattices	349	5.7. Intense probe beam	401
3. Sisyphus cooling in optical lattices	354	6. Temperature, fluorescence and imaging methods	404
3.1. The one-dimensional model	355	6.1. Temperature	404
3.2. Kinetic temperature	362	6.2. Fluorescence	407
3.3. Generalization to higher dimensions	368	6.3. Spatial diffusion	410
3.4. Bright lattices and grey molasses	372	7. Bragg scattering and four-wave mixing in optical lattices	413
3.5. Universality of Sisyphus cooling	375	7.1. Basics of Bragg scattering	414
4. Theoretical methods	377	7.2. Bragg scattering and four-wave mixing	415
4.1. Generalized optical Bloch equations	378		
4.2. The band method	380		
4.3. Semi-classical Monte-Carlo simulation	381		
4.4. The Monte-Carlo wavefunction approach	382		
5. Probe transmission spectroscopy: vibration, propagation and relaxation	383		

*Corresponding author. Fax: +3333-45-350076.

E-mail address: grynberg@physique.ens.fr (G. Grynberg).

7.3. The Debye–Waller factor—sensitivity to atomic localization	418	9.4. The asymmetric optical lattice: an analogue to molecular motors	433
7.4. Backaction of the localized atoms on the lattice beams	420	10. Nanolithography	436
8. Atomic interactions in optical lattices	423	10.1. The principles of atomic nanolithography	437
8.1. Light-induced interactions in optical lattices	423	10.2. Experimental achievements	437
8.2. Study of collisions	424	10.3. Latest research directions	439
9. Effect of a magnetic field	426	11. Conclusion	439
9.1. Paramagnetism	426	Acknowledgements	440
9.2. Antidot lattices	428	Appendix A. Index of notations	440
9.3. Lattice in momentum space	431	References	443

Abstract

We present a review of the work done with dissipative optical lattices so far. A dissipative optical lattice is achieved when a light field provides both velocity damping and spatial periodicity of the atomic density. We introduce the geometric properties of optical lattices using a classical model for the atoms. We discuss the Sisyphus cooling mechanism and its extension to different optical lattices, and we present the main theoretical approaches used to describe the atomic dynamics in optical lattices. The major experimental tools and studies are then discussed. This includes pump–probe spectroscopy, experiments based on fluorescence, Bragg scattering and studies of atomic interactions. We also present different phenomena occurring in the presence of an additional static magnetic field. Atomic nanolithography is finally briefly discussed as an application of optical lattices. © 2001 Elsevier Science B.V. All rights reserved.

PACS: 32.80.Lg; 32.80.Pj; 32.60.+i

Keywords: Laser cooling; Optical lattices

1. Introduction

Optical lattices consist of arrays of atoms bound by light. They officially came to the world in 1991–1992, when two groups observed signals originating from atoms spatially ordered in a standing wave [1–3]. In those experiments, light has two effects, firstly to attract the atoms around points located on a periodic lattice having a spatial period on the order of the optical wavelength, and secondly to cool down the atoms. In fact, optical lattices were conceived a few years earlier by Dalibard and Cohen-Tannoudji [4] and independently by Chu and his group [5] when they proposed their famous model to interpret the sub-Doppler cooling recently discovered by Phillips and his group [6]. They showed indeed that two counter-propagating laser beams having crossed linear polarizations can be used to damp the atomic velocity along their axis of propagation and to achieve very low temperatures. Although the fact that atoms should be regularly distributed along the standing wave is a byproduct of their model, this point was not much considered before 1991. In fact, the initial effort was mainly focused on the study of the distribution in momentum space rather than in real space. The atomic dynamics in such a light field was thus rather neglected. However, in 1990, Westbrook et al. [7] observed that the emission peak of laser cooled atoms was much narrower than the Doppler width, and this was a very serious indication that the atoms are bound around some points where they oscillate (Dicke narrowing [8]). The light field configuration used by Westbrook et al. consists of three pairs of cross-polarized counter-propagating beams, one along each axis, which allows velocity damping along any direction. Such a field configuration was called *molasses* by Chu et al. [9] because of the friction force that slows down the atoms. In fact, optical molasses and optical lattices are very often two sides of the same object. This object is named molasses when one considers velocity damping and momentum distribution, and lattice when the distribution in real space is investigated.

To be more precise, those objects that provide both *velocity damping* and *spatial periodicity* can be called “dissipative optical lattices” and their description is the main topic of this review. These dissipative optical lattices are obtained by tuning the incident beams in the neighbourhood of an atomic resonance. By contrast, when the beams frequency is far from any resonance, the velocity damping is no longer efficient but it is still possible to obtain a periodic atomic structure provided that the atoms are cooled by an independent method. These other lattices are usually called “far off-resonant optical lattices” and their properties will be reviewed in a forthcoming paper. The light field configuration used to obtain atomic optical lattices can also be adapted to achieve periodic patterns of mesoscopic objects. Many properties of these “mesoscopic optical lattices” are similar to those of “far off-resonant optical lattices” because in both cases, the main effect of the interaction between light and matter is to create a periodic dipole force originating from the dynamic Stark effect (see [10], Section II-E). These mesoscopic optical lattices provide a simple and elegant visual demonstration of the lattice structure [11]. They also provide a link with advanced technology [12].

All these lattices share a common feature: the lattice structure and the translation symmetries only depend on the directions of the laser beams [13,14]. Another general result concerns the topography of the electromagnetic forces field. This topography is independent of the phases of the laser beams when the minimum number of beams is used, and this number is equal to the dimensionality of the lattice plus 1 [13]. For instance, a phase-independent three-dimensional

lattice is obtained with four beams. These results are introduced in Section 2 using the classical description of atoms with an elastically bound electron. This model system is used here to describe the general geometric properties of optical lattices. It can often be applied to the far off-resonant and mesoscopic lattices with only minor modifications.

The cooling in dissipative optical lattices originates from the *Sisyphus effect* [15]. This process relying on the polarization gradient of the laser field is described in Section 3. The starting point is the famous one-dimensional “ $\text{lin} \perp \text{lin}$ ” configuration for a transition connecting levels having angular momenta $J_g = 1/2$ and $J_e = 3/2$ [16]. Several extensions of this model system are presented: to higher dimensions, to other beam configurations, to other transitions. In particular, transitions accommodating an internal dark state [17] provide a Sisyphus mechanism with significantly reduced fluorescence.

The main theoretical methods used to predict the behaviour of the atoms in an optical lattice are presented in Section 4. They range from approaches where the external degrees of freedom are described in the framework of classical mechanics to more sophisticated methods where a full quantum mechanical treatment is used.

Several experimental methods were used to study the properties of atoms in an optical lattice. We start by describing probe transmission spectroscopy (Section 5). This method was applied successfully to several problems, and in particular the study of the vibration of atoms around their equilibrium position and the demonstration of atomic propagating modes. In Section 6, we describe methods involving fluorescence or imaging. These methods were used in particular to measure atomic kinetic temperature and atomic spatial diffusion. Because of the periodic variation of the atomic density in an optical lattice, Bragg scattering can also be used. This technique and its applications are presented in Section 7. Although the separation between Sections 5–7 is perfectly consistent with respect to the experimental approach, it should be emphasized that the same physical phenomenon (atomic vibration for instance) can often be studied by different methods. Therefore, these sections are tightly connected.

The next two sections deal with perturbative effects. First, we discuss atom-atom interactions and collision processes in an optical lattice (Section 8). Second, we describe several phenomena occurring when an optical lattice is submitted to a static magnetic field (Section 9). This section covers a broad domain which includes paramagnetism, antidot lattices and atomic motors.

The last section is devoted to the applications of the optical lattices concepts to nanolithography (Section 10). Experiments showing regular patterns of atoms deposited on a surface are presented.

Under many circumstances, we have inserted comments in the core of the text. These comments can be skipped in a first reading. They generally concern more elaborate subjects that should be of interest mainly for those working in laser cooling and for those outside this field who want to deepen their knowledge on a particular point. An index of the notations used in the paper is presented in Appendix A.

2. A classical approach to optical lattices

Although optical lattices were mostly developed and studied in the context of sub-Doppler cooling of atoms which requires a quantum description of the internal degrees of freedom,

a classical approach performed in the spirit of the dipole force caused by field amplitude variations can be useful as a first step. In particular, the basis of optical lattices crystallography can be derived from such an approach. The conclusions of this section can also be readily applied to the case of the far-detuned traps for many atoms.

2.1. Atom with an elastically bound electron in a standing wave

In this section, we consider the classical model of an atom with an elastically bound electron and we show that the force acting on the atom has a component that derives from a potential. We will show that this dipole potential is proportional to the field intensity.

The position of the electron in the atomic frame is \mathbf{r}_e and its resonance frequency is ω_0 . We denote by \mathbf{R} the position of the atomic centre of mass and we assume that the atom is immersed in a standing wave

$$\mathbf{E}(\mathbf{r}, t) = E_0(\mathbf{r}) \operatorname{Re}[\boldsymbol{\varepsilon} \exp - i(\omega t - \phi)] . \quad (1)$$

In this section we assume that the polarization $\boldsymbol{\varepsilon}$ can be space dependent, but not the phase ϕ . The electric dipole interaction between the atom and the field is

$$V_{\text{AL}} = -q_e \mathbf{r}_e \cdot \mathbf{E}(\mathbf{R}, t) , \quad (2)$$

where q_e is the electron charge. By solving the dynamics equation for the electron, we find for the steady state value of the electric dipole moment $\mathbf{d} = q_e \mathbf{r}_e$

$$\mathbf{d} = \operatorname{Re}[\varepsilon_0 \alpha_0 E_0(\mathbf{R}) \boldsymbol{\varepsilon} \exp - i(\omega t - \phi)] , \quad (3)$$

with the following value for the polarizability α_0 :

$$\alpha_0 = - \frac{q_e^2}{2m_e \omega \varepsilon_0} \frac{1}{\Delta + i\Gamma/2} . \quad (4)$$

In this expression m_e is the electron mass, $\Delta = \omega - \omega_0$ the detuning from resonance and Γ the classical radiative width [19]. The force \mathbf{F}' acting on the atom is obtained by averaging $-\nabla_{\mathbf{R}} V_{\text{AL}} = \sum_{i=x,y,z} d_i \nabla_{\mathbf{R}} E_i$ over a time long compared to $2\pi/\omega$.

$$\mathbf{F}' = \frac{\varepsilon_0}{2} \alpha'_0 E_0(\mathbf{R}) \nabla_{\mathbf{R}} E_0(\mathbf{R}) , \quad (5)$$

where α'_0 is the real part of the polarizability ($\alpha_0 = \alpha'_0 + i\alpha''_0$). Eq. (5) shows that this force derives from a potential $U(\mathbf{R})$,

$$U(\mathbf{R}) = - \frac{\varepsilon_0}{4} \alpha'_0 E_0^2(\mathbf{R}) . \quad (6)$$

This is the classical prediction for the dynamic Stark effect. For a red detuning ($\Delta < 0$) of the incident field, the minima of the potential are found at points where the intensity is maximum. The atom is thus attracted towards the points of maximum intensity. By contrast, for a blue detuning ($\Delta > 0$) α'_0 is negative and the points of highest intensity correspond to maxima of the potential. The atom is then expelled from the high field intensity domains.

Comments: (i) When the saturation of the upper level is negligible, this model can be readily applied to a real atom on a transition connecting a ground state of angular momentum $J_g = 0$ to an excited state for which $J_e = 1$. More generally, it can be applied whenever the light-shift

effective Hamiltonian [18,20] is scalar. This is for example the case for a ground state of angular momentum $J_g = 1/2$ when the detunings from the $J_g = 1/2 \rightarrow J_e = 1/2$ and $J_g = 1/2 \rightarrow J_e = 3/2$ resonances are much larger than the fine structure of the excited state. If this condition is not fulfilled (i.e. the atom is excited either near a $J_g = 1/2 \rightarrow J_e = 1/2$ or near a $J_g = 1/2 \rightarrow J_e = 3/2$ transition) the light-shift Hamiltonian remains scalar if the light field polarization is linear (not necessarily in the same direction everywhere).

(ii) In the case where the phase ϕ is also space dependent, there is an additional contribution \mathbf{F}'' to the force which corresponds to the radiation pressure

$$\mathbf{F}'' = \frac{\varepsilon_0}{2} \alpha_0'' E_0^2(\mathbf{R}) \nabla_{\mathbf{R}} \phi(\mathbf{R}) . \quad (7)$$

This component of the force is associated to a transfer of momentum between the field and the atoms in a scattering process [21] (see also [10, Section V.C.2]).

In the general case, the total force acting on the atom is $\mathbf{F} = \mathbf{F}' + \mathbf{F}''$. In the situations where $E_0(\mathbf{R})$ and $\phi(\mathbf{R})$ exhibit variations having similar spatial scales, the ratio \mathbf{F}'/\mathbf{F}'' is on the order of $\alpha_0'/\alpha_0'' \sim |\Delta|/\Gamma$. If $|\Delta| \gg \Gamma$, the radiation pressure is then negligible compared to the dipole force.

(iii) In fact, the dipole force (Eq. (5)) was derived for a polarization $\boldsymbol{\varepsilon} = \sum_{i=x,y,z} f_i e^{i\phi_i} \mathbf{e}_i$ that verifies $\sum_i f_i^2 \nabla_{\mathbf{R}} \phi_i = 0$. If this condition is not fulfilled, $\nabla_{\mathbf{R}} \phi$ should be replaced by $\sum_i f_i^2 \nabla_{\mathbf{R}} \phi_i$ in the expression of the dissipative force (Eq. (7)).

(iv) If the field arises from the superposition of several beams of (real) amplitude E_i , polarization $\boldsymbol{\varepsilon}_i$, wavevector \mathbf{k}_i and phase ϕ_i , the dipole force and the dissipative force are, respectively, equal to

$$\mathbf{F}' = \varepsilon_0 \frac{\alpha_0'}{4} \sum_{l \neq j} i(\mathbf{k}_l - \mathbf{k}_j) E_l E_j (\boldsymbol{\varepsilon}_l \cdot \boldsymbol{\varepsilon}_j^*) e^{i[(\mathbf{k}_l - \mathbf{k}_j) \cdot \mathbf{R} + \phi_l - \phi_j]} , \quad (8)$$

$$\mathbf{F}'' = \varepsilon_0 \frac{\alpha_0''}{2} \sum_l E_l^2 \mathbf{k}_l + \varepsilon_0 \frac{\alpha_0''}{4} \sum_{l \neq j} (\mathbf{k}_l + \mathbf{k}_j) E_l E_j (\boldsymbol{\varepsilon}_l \cdot \boldsymbol{\varepsilon}_j^*) e^{i[(\mathbf{k}_l - \mathbf{k}_j) \cdot \mathbf{R} + \phi_l - \phi_j]} . \quad (9)$$

(v) The dipole potential $U(\mathbf{R})$ depends on the field intensity but not on its polarization because the atomic polarizability α_0 was assumed to be scalar.

2.2. One-dimensional lattices

We study in this section the dipole potential generated by two counter-propagating plane waves \mathbf{E}_1 and \mathbf{E}_2 having the same polarization $\boldsymbol{\varepsilon}$

$$\mathbf{E}_1(\mathbf{r}, t) = E_0 \operatorname{Re}[\boldsymbol{\varepsilon} \exp - i(\omega t - kz - \phi_1)] , \quad (10)$$

$$\mathbf{E}_2(\mathbf{r}, t) = E_0 \operatorname{Re}[\boldsymbol{\varepsilon} \exp - i(\omega t + kz - \phi_2)] . \quad (11)$$

The total field is then

$$\mathbf{E}(\mathbf{r}, t) = 2E_0 \cos\left(kz + \frac{\phi_1 - \phi_2}{2}\right) \operatorname{Re}\left[\boldsymbol{\varepsilon} \exp - i\left(\omega t - \frac{\phi_1 + \phi_2}{2}\right)\right] . \quad (12)$$

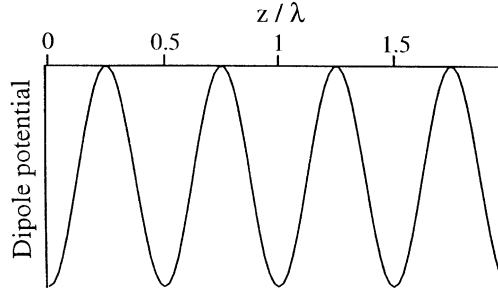


Fig. 1. Dipole potential for two counter-propagating beams of same polarization and frequency. The potential exhibits wells located periodically every $\lambda/2$.

Using Eq. (6), we find the following value for the dipole potential:

$$U(\mathbf{R}) = -\varepsilon_0 \alpha'_0 E_0^2 \cos^2 \left(kZ + \frac{\phi_1 - \phi_2}{2} \right). \quad (13)$$

The potential is periodic (Fig. 1) with a spatial periodicity $\lambda/2$ (λ being the wavelength of the incident field $\lambda = 2\pi/k$). It consists of a succession of potential wells, each having a depth $\varepsilon_0 |\alpha'_0| E_0^2$.

The possibility to trap atoms in such potential wells was considered by Lethokov et al. [22]. The typical range of potential depths available with usual lasers lies in the mK and sub-mK domain. To have an efficient trapping, it is thus necessary to get very cold atoms. In principle, the fields (10) and (11) that create the potential can also be used to cool the atoms. However the cooling mechanism (Doppler cooling [23]) which arises from the radiation pressure is generally not sufficient to achieve the very low temperatures required to trap the atoms. An external cooling mechanism is thus necessary. This can be obtained with additional laser beams using the polarization gradient cooling method that we describe in Section 3.

One of the interesting features of Eq. (13) is that the topography of the potential does not change under a variation of the phases ϕ_1 and ϕ_2 of the incident beams: a *phase variation* just induces a *translation* of the potential. More precisely, Eq. (12) shows that a phase shift corresponds to a space translation and a time translation. It is always possible, using the appropriate translations, to write the total electric field as $2E_0 \cos kz \operatorname{Re}[\varepsilon \exp - i\omega t]$. In this field configuration the number of independent phases (two) is equal to the number of possible translations.

Comments: (i) The topography of the potential is the same for red- and blue-detuned fields. However atoms are attracted to high intensity domains in the first case and to low intensity domains in the second case.

(ii) The channeling of atoms along the nodal lines of a blue-detuned standing wave was experimentally observed by Salomon et al. [24].

(iii) The dipole potential changes with the polarization of the counter-propagating beams. For instance, if these beams have crossed polarizations either linear (lin \perp lin configuration) or circular ($\sigma^+ - \sigma^-$ or corkscrew configuration), potential (6) is flat because the field intensity is space independent. We will see in Section 3 that this result does not hold when the ground

state is degenerate and the light-shift Hamiltonian is not scalar. In this case the polarization gradient creates a spatially modulated potential.

2.3. Two-dimensional periodic lattices

Several beam configurations can be used to generate a periodic 2D lattice. We first present (Section 2.3.1) a configuration with three travelling waves and we show that the corresponding dipole potential has a topography which is invariant under phase variations of the incident beams [13]. We then use crystallographic results to determine the symmetries of the lattice and we show how the primitive translations of the reciprocal lattice are deduced from the beam wavevectors [14] (Section 2.3.2). In the following section (Section 2.3.3) we study the configurations with two standing waves i.e. four travelling waves. Although more intuitive than the three-beam configuration, these configurations lead to dipole potentials the topography of which can depend on the relative phases of the beams [25]. Generally, the potentials appear as a periodic array of potential wells; however, it is also possible to generate a periodic array of antidots [26] (Section 2.3.4). Finally we show that the four-beam configuration allows to generate a superlattice [27], i.e. a periodic potential with two different spatial scales, microscopic potential wells being embedded in potential wells of much larger size (Section 2.3.5).

2.3.1. Phase-independent lattices: three-beam configuration

Consider the case of three waves \mathbf{E}_1 , \mathbf{E}_2 , \mathbf{E}_3 , of same polarization \mathbf{e}_z and wavevectors \mathbf{k}_1 , \mathbf{k}_2 , \mathbf{k}_3 , located in the xOy plane (Fig. 2a):

$$\mathbf{E}_i(\mathbf{r}, t) = E_0 \mathbf{e}_z \text{Re}[\exp - i(\omega t - \mathbf{k}_i \cdot \mathbf{r} - \phi_i)], \quad i = 1, 2, 3. \quad (14)$$

The dipole potential (6) associated with this field configuration is

$$U(\mathbf{R}) = -\frac{\varepsilon_0}{4} \alpha'_0 E_0^2 \left\{ 3 + 2 \sum_{i>j} \cos[(\mathbf{k}_i - \mathbf{k}_j) \cdot \mathbf{R} + \phi_i - \phi_j] \right\}. \quad (15)$$

The potential consists in a periodic array of two-dimensional wells, as shown by the plot of Fig. 2b obtained for a red detuning ($\alpha'_0 > 0$). Here again phase variations do not affect the topography of the potential but just lead to a global translation. This is because the potential U in Eq. (15) depends on two independent parameters, $(\phi_1 - \phi_2)$ and $(\phi_2 - \phi_3)$, which correspond to the two coordinates X_0 and Y_0 of a space translation. More precisely, the *three* phases ϕ_1 , ϕ_2 and ϕ_3 of the three-beam configuration are associated with *three* free parameters, namely the origin in time and space: this is why the topography of the potential is invariant under phase variations [13].

When the wavevectors \mathbf{k}_2 and \mathbf{k}_3 propagate in symmetric directions with respect to \mathbf{k}_1 :

$$\begin{aligned} \mathbf{k}_1 &= k \mathbf{e}_x, \\ \mathbf{k}_2 &= k[\mathbf{e}_x \cos \theta + \mathbf{e}_y \sin \theta], \\ \mathbf{k}_3 &= k[\mathbf{e}_x \cos \theta - \mathbf{e}_y \sin \theta], \end{aligned} \quad (16)$$

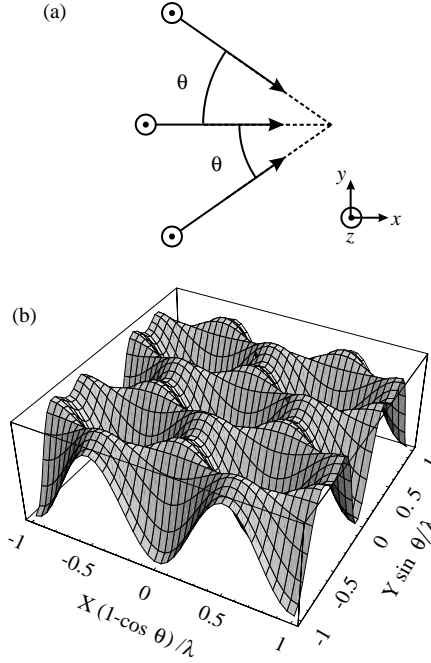


Fig. 2. (a) Three-beam configuration, (b) Dipole potential in the case of red detuned laser beams. This potential shows a periodic array of potential wells and its topography is not changed by phase variations of the incident beams.

the dipole potential deduced from (15) is

$$U(\mathbf{R}) = -\frac{\varepsilon_0}{4}\alpha'_0 E_0^2 \left[3 + 2\cos(2K_\perp Y + \phi_2 - \phi_3) + 4\cos\left(KX + \phi_1 - \frac{\phi_2 + \phi_3}{2}\right)\cos\left(K_\perp Y + \frac{\phi_2 - \phi_3}{2}\right) \right], \quad (17)$$

with $K_\perp = k \sin \theta$ and $K = k(1 - \cos \theta)$. The potential is periodic along the Oy and Ox directions with spatial periodicities $\lambda_\perp = \lambda/\sin \theta$ and $\Lambda = \lambda/(1 - \cos \theta)$, respectively. The symmetry of this potential generally corresponds to a centred rectangular lattice [14]. It becomes a hexagonal lattice for $\theta = \pi/3, 2\pi/3$ and a square lattice for $\theta = \pi/2$. The fact that the potential depends on two phase parameters $(\phi_2 - \phi_3)$ and $(\phi_1 - (\phi_2 + \phi_3)/2)$ corresponding to a translation along Oy and Ox , respectively, is particularly clear on Eq. (17).

Comments: (i) The three-beam configuration gives both a dipole force and a radiation pressure force.

(ii) In the general case where the beams have amplitudes E_i and polarizations ε_i which can be different, the dipole potential is equal to

$$U(\mathbf{R}) = -\frac{\varepsilon_0}{4}\alpha'_0 \left\{ \sum_i E_i^2 + \sum_{i \neq j} E_i E_j (\varepsilon_i \cdot \varepsilon_j^*) \exp i[(\mathbf{k}_i - \mathbf{k}_j) \cdot \mathbf{R} + \phi_i - \phi_j] \right\}. \quad (18)$$

It can be easily checked that the dipole force given by Eq. (8) is equal to $-\nabla_{\mathbf{R}} U(\mathbf{R})$.

2.3.2. Spatial periodicity and reciprocal lattice

Eq. (15) shows that the potential $U(\mathbf{R})$ is invariant under a space translation $\mathbf{R}_{mn} = m\mathbf{a}_1 + n\mathbf{a}_2$ ($m, n \in \mathbb{Z}$) with

$$(\mathbf{k}_1 - \mathbf{k}_2) \cdot \mathbf{a}_1 = 2\pi \quad (\mathbf{k}_1 - \mathbf{k}_3) \cdot \mathbf{a}_1 = 0, \quad (19)$$

$$(\mathbf{k}_1 - \mathbf{k}_2) \cdot \mathbf{a}_2 = 0 \quad (\mathbf{k}_1 - \mathbf{k}_3) \cdot \mathbf{a}_2 = 2\pi. \quad (20)$$

Spatial periodicity is generated through the basis vectors \mathbf{a}_1 and \mathbf{a}_2 . Eqs. (19) and (20) also show that the vectors $\mathbf{a}_1^\star = (\mathbf{k}_1 - \mathbf{k}_2)$ and $\mathbf{a}_2^\star = (\mathbf{k}_1 - \mathbf{k}_3)$ are primitive translations of the reciprocal lattice (they form a basis of the reciprocal lattice) [13]. In practice, it is straightforward to characterize the reciprocal lattice from the beam wavevectors, and the primitive translations of the lattice in real space are found from Eqs. (19) and (20).

The notion of reciprocal lattice is particularly useful in the context of *Bragg scattering* [28] (see also Section 7.1). Let us consider an ensemble of atoms immersed in the potential of Fig. 2 and assume that a probe beam with wavevector \mathbf{k}_p (not necessarily of frequency ω) is sent into the atomic cloud. Bragg diffraction occurs along directions \mathbf{k}_B such as

$$\mathbf{k}_B = \mathbf{k}_p + \mathbf{G}, \quad (21)$$

where $\mathbf{G} = p\mathbf{a}_1^\star + q\mathbf{a}_2^\star$ ($p, q \in \mathbb{Z}$) is a vector of the reciprocal lattice.

In fact, in nonlinear optics the origin of the coherent emission along \mathbf{k}_B will be credited to a multiwave-mixing process involving exchange of photons between the lattice beams. In this approach, Eq. (21) appears as a *phase-matching* condition [13] for the multiwave-mixing process:

$$\mathbf{k}_B = \mathbf{k}_p + (p + q)\mathbf{k}_1 - p\mathbf{k}_2 - q\mathbf{k}_3. \quad (22)$$

The scattering process has involved the absorption of $(p + q)$ photons in the beam \mathbf{E}_1 and the stimulated emission of p photons in the beam \mathbf{E}_2 and q photons in the beam \mathbf{E}_3 .

Comments: (i) From the comparison between the Bragg condition and the phase-matching condition, one can directly infer that the translation symmetries of the potential are imposed solely by the beam directions. For a three-beam configuration, $\mathbf{a}_1^\star = (\mathbf{k}_1 - \mathbf{k}_2)$ and $\mathbf{a}_2^\star = (\mathbf{k}_1 - \mathbf{k}_3)$ are primitive vectors of the reciprocal lattice whatever the fields amplitudes and polarizations. The determination of the lattice structure (oblique, rectangular, square, hexagonal) is thus determined by \mathbf{k}_1 , \mathbf{k}_2 , \mathbf{k}_3 . Of course, the shape of the potential inside a unit cell depends also on amplitudes and polarizations.

(ii) If the three wavevectors do not belong to the same plane, the dipole potential is still modulated only in two dimensions. This is because all the vectors of the reciprocal lattice belong to the plane P containing $\mathbf{a}_1^\star = (\mathbf{k}_1 - \mathbf{k}_2)$ and $\mathbf{a}_2^\star = (\mathbf{k}_1 - \mathbf{k}_3)$ (for example $\mathbf{k}_2 - \mathbf{k}_3 = \mathbf{a}_2^\star - \mathbf{a}_1^\star$). This implies that in real space, the potential does not exhibit any spatial modulation along the direction orthogonal to P . To achieve a real 3D potential, four beams at least are necessary.

(iii) Several choices for the primitive vectors in the reciprocal lattice are possible. Instead of \mathbf{a}_1^\star and \mathbf{a}_2^\star , one can for example choose $\mathbf{b}_1^\star = (\mathbf{k}_1 - \mathbf{k}_2)$ and $\mathbf{b}_2^\star = (\mathbf{k}_2 - \mathbf{k}_3)$.

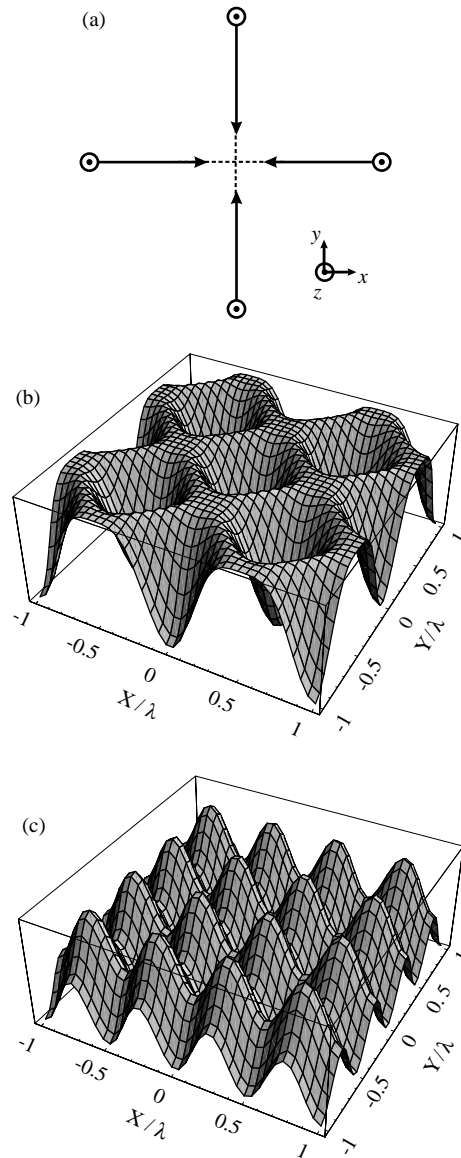


Fig. 3. (a) Beam configuration generating a phase-dependent 2D periodic lattice. The figure is drawn with $\mathbf{k}_1 \perp \mathbf{k}_2$. (b) Dipole potential for red detuned laser beams and $\phi_1 = \phi_2 = \phi_3 = \phi_4 = 0$. (c) Dipole potential for red detuned laser beams and $\phi_1 = \phi_3 = \pi/2$, $\phi_2 = \phi_4 = 0$.

2.3.3. Phase-dependent lattices

Consider now the case of four beams $\mathbf{E}_1, \mathbf{E}_2, \mathbf{E}_3, \mathbf{E}_4$ of same polarization \mathbf{e}_z and wavevectors $\mathbf{k}_1, \mathbf{k}_2, \mathbf{k}_3 = -\mathbf{k}_1, \mathbf{k}_4 = -\mathbf{k}_2$ (Fig. 3). The phases of the beams are, respectively, $\phi_1, \phi_2, \phi_3, \phi_4$. This situation corresponds to the interference of two 1D standing waves (studied in Section 2.2) but propagating along different axis. The dipole potential (6) for this

situation is

$$U(\mathbf{R}) = -\varepsilon_0 \alpha'_0 E_0^2 \left[\cos^2 \left(\mathbf{k}_1 \cdot \mathbf{R} + \frac{\phi_1 - \phi_3}{2} \right) + \cos^2 \left(\mathbf{k}_2 \cdot \mathbf{R} + \frac{\phi_2 - \phi_4}{2} \right) + 2 \cos \left(\frac{\phi_1 + \phi_3 - \phi_2 - \phi_4}{2} \right) \cos \left(\mathbf{k}_1 \cdot \mathbf{R} + \frac{\phi_1 - \phi_3}{2} \right) \cos \left(\mathbf{k}_2 \cdot \mathbf{R} + \frac{\phi_2 - \phi_4}{2} \right) \right]. \quad (23)$$

This potential is still periodic but it is no longer invariant under phase variations. This is because U depends on three independent parameters $(\phi_1 - \phi_3)$, $(\phi_2 - \phi_4)$ and $(\phi_1 + \phi_3 - \phi_2 - \phi_4)$ whereas a space translation can only cope with two. This phase dependence is clearly seen in Figs. 3b and c where we have plotted the potentials for red detuned beams, $\phi_1 - \phi_3 = \phi_2 - \phi_4 = 0$ and $(\phi_1 + \phi_3 - \phi_2 - \phi_4) = 0$ in Fig. 3b and $(\phi_1 + \phi_3 - \phi_2 - \phi_4) = \pi$ in Fig. 3c. In the four-beam situation, it is necessary to control the phases of the beams to keep the topography of the potential unchanged.

Comments: (i) With the three beams \mathbf{E}_1 , \mathbf{E}_2 , \mathbf{E}_3 one achieves a periodic potential and a set of primitive translations for the reciprocal lattice are $\mathbf{a}_1^* = \mathbf{k}_1 - \mathbf{k}_2$ and $\mathbf{a}_2^* = \mathbf{k}_1 - \mathbf{k}_3 = 2\mathbf{k}_1$. The addition of the beam \mathbf{E}_4 introduces a third possible primitive translation $\mathbf{a}_3^* = \mathbf{k}_1 - \mathbf{k}_4 = \mathbf{k}_1 + \mathbf{k}_2$. However \mathbf{a}_3^* belongs to the lattice generated by \mathbf{a}_1^* and \mathbf{a}_2^* because $\mathbf{a}_3^* = \mathbf{a}_2^* - \mathbf{a}_1^*$. This is why this four-beam lattice remains periodic. The configurations where \mathbf{a}_3^* cannot be expanded as a superposition of \mathbf{a}_1^* and \mathbf{a}_2^* with rational coefficients will be studied in Section 2.4.

(ii) Consider the three-beam configuration with $\mathbf{k}_1 = -\mathbf{k}_3 = k\mathbf{e}_x$ and $\mathbf{k}_2 = k\mathbf{e}_y$. This beam configuration generates a lattice with a square unit cell (see comment in Section 2.3.1). The same translational symmetry is found with the four-beam configuration, where a fourth beam is added along $\mathbf{k}_4 = -k\mathbf{e}_y$. If all the beams have the same phase and the same amplitude, a reflection symmetry is obtained in the three-beam case, but the lattice is invariant under a $\pi/2$ rotation only for the four-beam configuration. This example shows that the translation group of the lattice is determined by the incident beams wavevectors, but the potential may have additional symmetries. A similar distinction is encountered in crystallography where one can associate to each point of a Bravais lattice a basis of atoms with its own point-group symmetry [28,29].

(iii) The topography of 2D four-beam lattices is generally phase-dependent. However there are some exceptions to this rule. Consider the beam configuration where \mathbf{E}_1 and \mathbf{E}_3 are counter-propagating beams travelling along Ox and polarized along Oy , and \mathbf{E}_2 and \mathbf{E}_4 are counter-propagating beams travelling along Oy and polarized along Ox . The dipole potential for this situation is

$$U(\mathbf{R}) = -\varepsilon_0 \alpha'_0 E_0^2 \left[\cos^2 \left(kX + \frac{\phi_1 - \phi_3}{2} \right) + \cos^2 \left(kY + \frac{\phi_2 - \phi_4}{2} \right) \right]. \quad (24)$$

There are only two independent phase parameters in Eq. (24) and a phase variation just induces a translation of the potential without changing its topography.

Such a result is obtained because the two standing waves have orthogonal polarizations and the dipole potential only depends on the field intensity. The interference between the two standing waves is thus not crucial for the dipole potential. This property does not hold in the

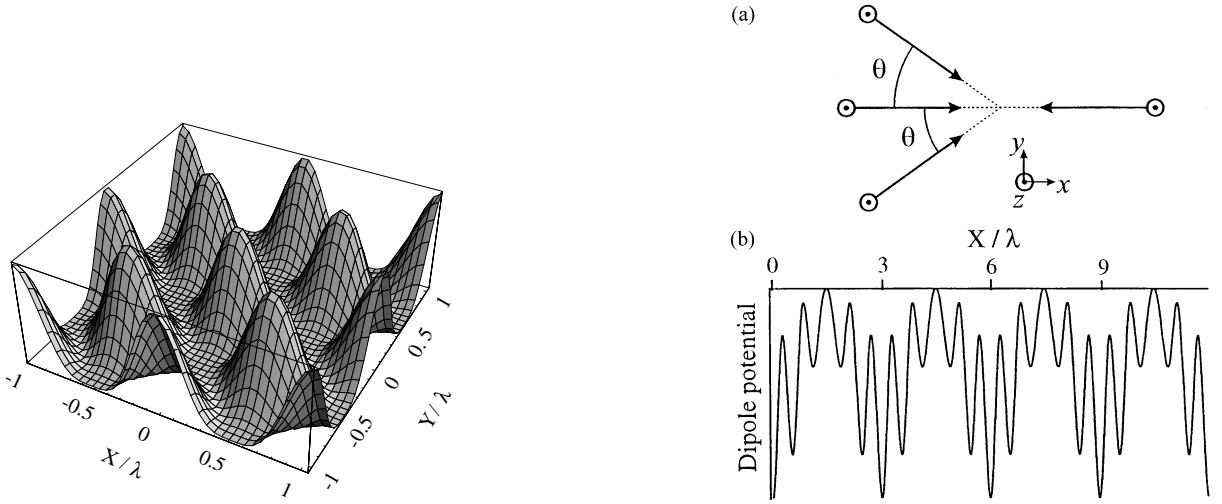


Fig. 4. Dipole potential for the four-beam configuration of Fig. 3 with $\phi_1 = \phi_2 = \phi_3 = \phi_4 = 0$. The beams are tuned on the blue side of the resonance. The shape of the potential corresponds to an antidot lattice.

Fig. 5. (a) Beam configuration. The angle θ is assume to be small ($\theta < \pi/2$) and $\cos \theta = 1 - 1/p$ with $p \in \mathbb{N}$. (b) Section of the dipole potential along the x -axis for $p=3$. The potential has a periodicity $p\lambda$ but a smaller structure with a dimension $\lambda/2$ is superimposed on the long range variation.

general case of a nonscalar light-shift Hamiltonian because the light-shifts then depend both on the intensity and on the polarization.

2.3.4. Antidot lattices

The potential shown in Fig. 3b for red-detuned beams ($\alpha'_0 > 0$) consists of a periodic array of potential wells. In the case of blue-detuned beams ($\alpha'_0 < 0$), and for the same values of the phases, one obtains a potential exhibiting antidots (Fig. 4). Instead of wells associated with localized minima of the potential, one finds here that the minima correspond to continuous lines. Because the atoms can move along these lines, the atomic dynamics is expected to be markedly different from that in a lattice exhibiting wells where the atoms can be trapped.

Comments: (i) In the general case, a 2D periodic potential exhibits both localized minima and maxima. There are thus both wells and antidots. If the potential wells are sufficiently deep, the trapping in the wells is however dominant in the atomic dynamics.

(ii) The notion of antidot lattices is obviously connected to the lattice dimensionality. There exists antidot lattices in 2D and 3D, but not in 1D where a description in terms of wells is always appropriate.

2.3.5. Superlattices

We consider again the case of four waves $\mathbf{E}_1, \mathbf{E}_2, \mathbf{E}_3, \mathbf{E}_4$ of same frequency and polarization \mathbf{e}_z , but the beam configuration (Fig. 5a) is obtained by adding a beam of wavevector $\mathbf{k}_4 = -k\mathbf{e}_x$ to the three-beam configuration of Eq. (16).

Assuming $\phi_1 = \phi_2 = \phi_3 = 0$ for the sake of simplicity, the dipole potential in this case is

$$U(\mathbf{R}) = -\varepsilon_0 \alpha'_0 E_0^2 \left\{ 1 + \frac{1}{2} \cos(2kX - \phi_4) + \frac{1}{2} \cos 2K_\perp Y + \cos K_\perp Y (\cos KX + \cos[(2k - K)X - \phi_4]) \right\}, \quad (25)$$

with $K_\perp = k \sin \theta$ and $K = k(1 - \cos \theta)$.

This potential is periodic along Oy with a periodicity $\lambda_\perp = \lambda/\sin \theta$, but along Ox , U is periodic only if $(1 - \cos \theta)$ is rational. This is because U is a combination of functions having different spatial periods along Ox . One spatial period is $\lambda/2$ and the other one is $\Lambda = \lambda/(1 - \cos \theta)$. We assume in this section that the potential is periodic. For instance, in the case where $(1 - \cos \theta) = 1/p$ ($p \in \mathbb{N}$), the periodicity of the potential along Ox is $p\lambda$. However, potential minima separated by a distance on the order of $\lambda/2$ are found along a x -section of the potential (see Fig. 5b). The coexistence of this small scale $\lambda/2$ with the large scale Λ is characteristic of a superlattice.

Comments: (i) If $(1 - \cos \theta) = q/p$, the periodicity along the x -axis is $p\lambda$ for q odd and $p\lambda/2$ for q even.

(ii) In principle (i.e. mathematically), a periodic lattice is found for any rational value q/p of $(1 - \cos \theta)$. However, from a physical point of view, there are some limitations originating for example from the size of the sample interacting with the beams. If the sample has a dimension L , the periodicity can be observed only if $p\lambda \ll L$.

(iii) If $(1 - \cos \theta)$ is not rational, the potential is called quasi-periodic. This type of potential will be considered in Section 2.4.

(iv) The connection between the three possible translation vectors of the reciprocal lattice $\mathbf{a}_1^\star = \mathbf{k}_1 - \mathbf{k}_2$, $\mathbf{a}_2^\star = \mathbf{k}_1 - \mathbf{k}_3$ and $\mathbf{a}_3^\star = \mathbf{k}_1 - \mathbf{k}_4$ is

$$(1 - \cos \theta) \mathbf{a}_3^\star = \mathbf{a}_1^\star + \mathbf{a}_2^\star. \quad (26)$$

When $(1 - \cos \theta) = q/p$ (and for instance p and q odd), a possible choice of primitive vectors in the reciprocal lattice is $\mathbf{c}_i^\star = ((a_i^\star)_X/q) \mathbf{e}_x + (a_i^\star)_Y \mathbf{e}_y$ ($i = 1, 2$). It can be easily checked that $\mathbf{a}_1^\star, \mathbf{a}_2^\star$ and \mathbf{a}_3^\star can be expanded on \mathbf{c}_1^\star and \mathbf{c}_2^\star with integer coefficients.

2.4. Quasiperiodic lattices

As illustrated by Eq. (25), the dipole potential generated by a 2D four-beam configuration often appears as a superposition of periodic functions with different periodicities. If the ratio of the periods is rational, the potential remains periodic (superlattices case). If the ratio is irrational, the potential is called quasiperiodic. Nevertheless, the quasiperiodic potential exhibits some long range order, as proved by the occurrence of discrete peaks in the Fourier transform of the potential.

The concept of quasiperiodic lattices has been investigated in great details [30–32] after the discovery of incommensurate phases [33] and quasicrystals [34] in solid-state physics. However the mathematical description has started earlier with the work of Bohr [35] on quasiperiodic functions, and it is this approach, in terms of continuous functions, that is more appropriate in the case of optical lattices.

Although nonperiodic, a quasiperiodic potential is for a physicist very similar to a periodic structure. In particular, there is a discrete but infinite set of translations T for which $U(X + T)$ and $U(X)$ are almost equal. This means that a sequence of potential wells found around some point in X_0 will be reproduced in an almost identical way in a large number of locations.

Under many circumstances, the quasiperiodic dipole potential U is also weakly dependent on the phase of the beams. When the phases ϕ_i change, a new potential U_ϕ is achieved which cannot be superimposed to the first one U through a translation. However, here again, any sequence of potential wells found in U will be also found almost identically around some other point in U_ϕ . This property (called “local isomorphism” [36,37]) explains why most physical results do not depend on the phases ϕ_i in a quasiperiodic potential [38].

Comments: (i) A 2D quasiperiodic potential is the section of a periodic potential in a higher dimension space [39]. For instance, the potential given by Eq. (25) is the section in the plane $Z = X - (\phi_4/2k)$ of the 3D periodic potential $U^{(3)}$

$$U^{(3)}(X, Y, Z) = -\varepsilon_0 \alpha'_0 E_0^2 \left\{ 1 + \frac{1}{2} \cos(2kZ) + \frac{1}{2} \cos 2K_\perp Y \right. \\ \left. + \cos K_\perp Y (\cos KX + \cos[2kZ - KX]) \right\} . \quad (27)$$

Indeed, changing the phase ϕ_4 results in a translation of the plane used for the cut. The local isomorphism means that all the 2D sections performed with a plane parallel to $Z = X$ are equivalent.

(ii) Because three beams are necessary to obtain a periodic potential in 2D and four beams in 3D, we may infer that the most general distribution of four beams in a plane corresponds to a quasiperiodic potential originating from the cut of a 3D periodic potential. In the case of five beams in a plane, the periodic potential should generally be found in a 4D space.

(iii) A particularly interesting example of a five-beam quasi-periodic lattice is found using five travelling waves (Fig. 6a) having wavevectors

$$\mathbf{k}_n = k \left[\mathbf{e}_x \cos \frac{2n\pi}{5} + \mathbf{e}_y \sin \frac{2n\pi}{5} \right] \quad (n = 0, \dots, 4) .$$

If all the beams have the same polarization \mathbf{e}_z and the same phase, the potential is invariant in a rotation of $2\pi/5$ around the origin. This potential is a 2D section of a 4D periodic potential and all the potentials obtained through phase variations are locally isomorphic. This potential has close connections with the Penrose tiling of the plane [40].

A potential having the same symmetry can be achieved using five standing waves instead (Fig. 6b). In this case there are 10 independent phases and the topography of the quasiperiodic potential depends on the relative phases.

2.5. Three-dimensional lattices

Most properties of 3D lattices are simple extensions of the results obtained in 2D. The presentation will thus be short. We first present the four-beam configurations (Section 2.5.1) which always lead to a periodic lattice with a phase-independent topography [13]. We then consider the lattices generated by a number of beams larger than 4 (Section 2.5.2) and we show that they can lead to periodic [41] or quasiperiodic [38] lattices depending on the beam

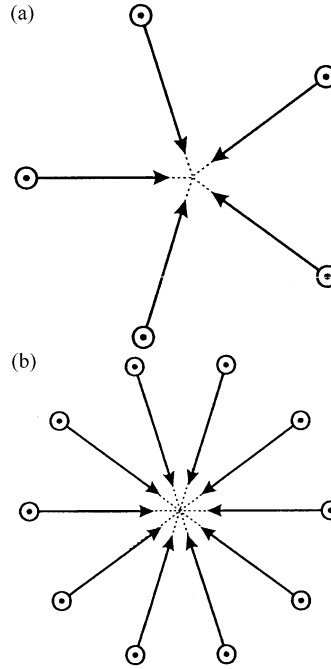


Fig. 6. (a) Five-beam configuration generating a quasi-periodic potential having a five-fold symmetry. (b) If standing waves are used instead of travelling waves, the potentials obtained through phase variations are no longer locally isomorphic.

wavevectors. In the last subsection (Section 2.5.3) we show that diffraction of the light by a periodic mask (Talbot effect [43–45]) can also be used to create a 3D lattice [46].

2.5.1. Phase-independent lattices: four-beam configurations

We consider an ensemble of four beams having wavevectors \mathbf{k}_i , amplitudes E_i and polarizations ε_i . The dipole potential for this configuration is given by Eq. (18) where the sum runs on $i = 1, \dots, 4$. This expression of U shows that the potential $U(\mathbf{R})$ is invariant under a space translation $\mathbf{R}_{mnp} = m\mathbf{a}_1 + n\mathbf{a}_2 + p\mathbf{a}_3$ ($m, n, p \in \mathbb{Z}$) with

$$\begin{aligned} (\mathbf{k}_1 - \mathbf{k}_2) \cdot \mathbf{a}_1 &= 2\pi, & (\mathbf{k}_1 - \mathbf{k}_3) \cdot \mathbf{a}_1 &= 0, & (\mathbf{k}_1 - \mathbf{k}_4) \cdot \mathbf{a}_1 &= 0, \\ (\mathbf{k}_1 - \mathbf{k}_2) \cdot \mathbf{a}_2 &= 0, & (\mathbf{k}_1 - \mathbf{k}_3) \cdot \mathbf{a}_2 &= 2\pi, & (\mathbf{k}_1 - \mathbf{k}_4) \cdot \mathbf{a}_2 &= 0, \\ (\mathbf{k}_1 - \mathbf{k}_2) \cdot \mathbf{a}_3 &= 0, & (\mathbf{k}_1 - \mathbf{k}_3) \cdot \mathbf{a}_3 &= 0, & (\mathbf{k}_1 - \mathbf{k}_4) \cdot \mathbf{a}_3 &= 2\pi. \end{aligned} \quad (28)$$

This set of equations shows that $\mathbf{a}_1^\star = (\mathbf{k}_1 - \mathbf{k}_2)$, $\mathbf{a}_2^\star = (\mathbf{k}_1 - \mathbf{k}_3)$ and $\mathbf{a}_3^\star = (\mathbf{k}_1 - \mathbf{k}_4)$ are primitive translations of the reciprocal lattice [13]. As in the 2D case, the reciprocal lattice is currently used to determine the lattice translation symmetries. The primitive translation vectors $\mathbf{a}_1, \mathbf{a}_2, \mathbf{a}_3$ in real space are then determined using (28) or equivalently [28,29].

$$\mathbf{a}_1 = 2\pi \frac{\mathbf{a}_2^\star \times \mathbf{a}_3^\star}{\mathbf{a}_1^\star \cdot (\mathbf{a}_2^\star \times \mathbf{a}_3^\star)}, \quad \mathbf{a}_2 = 2\pi \frac{\mathbf{a}_3^\star \times \mathbf{a}_1^\star}{\mathbf{a}_1^\star \cdot (\mathbf{a}_2^\star \times \mathbf{a}_3^\star)}, \quad \mathbf{a}_3 = 2\pi \frac{\mathbf{a}_1^\star \times \mathbf{a}_2^\star}{\mathbf{a}_1^\star \cdot (\mathbf{a}_2^\star \times \mathbf{a}_3^\star)}. \quad (29)$$

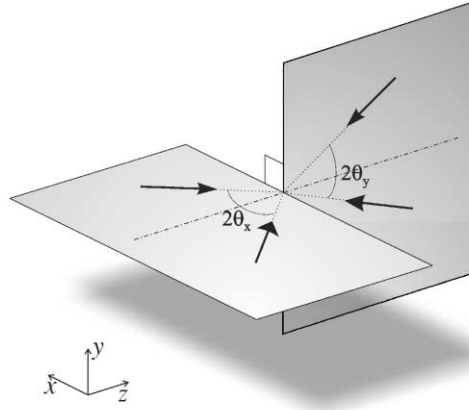


Fig. 7. Example of four-beam configuration. Two pairs of beams symmetrically located with respect of Oz propagate in the xOz and yOz planes, respectively.

The topography of these four-beam 3D lattices does not depend on the beam phases; a phase variation just leads to a translation of the potential (see comment (i)).

There are many possible four-beam configurations [14]. We describe here a configuration [42] that is often used. It consists of two beams propagating in the xOz plane, having wavevectors symmetrical with respect to Oz , and two other beams propagating in the yOz plane, with wavevectors symmetrical with respect to Oz (Fig. 7).

$$\begin{aligned} \mathbf{k}_1 &= k[\mathbf{e}_x \sin \theta_x + \mathbf{e}_z \cos \theta_x], & \mathbf{k}_2 &= k[-\mathbf{e}_x \sin \theta_x + \mathbf{e}_z \cos \theta_x], \\ \mathbf{k}_3 &= k[\mathbf{e}_y \sin \theta_y - \mathbf{e}_z \cos \theta_y], & \mathbf{k}_4 &= k[-\mathbf{e}_y \sin \theta_y - \mathbf{e}_z \cos \theta_y]. \end{aligned} \quad (30)$$

The knowledge of \mathbf{a}_1^* , \mathbf{a}_2^* , \mathbf{a}_3^* (or any other set of primitive translation vectors) allows to determine the lattice structure in the reciprocal space. Using the relationship between the structures in the reciprocal and direct spaces [28], the lattice in direct space can be determined. In the general case, the field configuration of Fig. 7 gives a face-centred orthorhombic lattice [14]. When $\theta_x = \theta_y = \theta$ the lattice is tetragonal. One finds a face-centred cubic lattice when $\theta = \arccos(1/\sqrt{5})$ and a body-centred cubic lattice when $\theta = \arccos(1/\sqrt{3})$.

More precisely, if we take $\mathbf{c}_1^* = \mathbf{k}_1 - \mathbf{k}_2$, $\mathbf{c}_2^* = \mathbf{k}_3 - \mathbf{k}_4$ and $\mathbf{c}_3^* = \mathbf{k}_1 - \mathbf{k}_3$ as a set of primitive vectors in the reciprocal space, the primitive translations \mathbf{c}_1 , \mathbf{c}_2 , \mathbf{c}_3 obtained using Eqs. (29) are equal to

$$\begin{aligned} \mathbf{c}_1 &= \frac{\lambda_x}{2} \mathbf{e}_x - \frac{\lambda_+}{4} \mathbf{e}_z, \\ \mathbf{c}_2 &= \frac{\lambda_y}{2} \mathbf{e}_y + \frac{\lambda_+}{4} \mathbf{e}_z, \\ \mathbf{c}_3 &= \frac{\lambda_+}{4} \mathbf{e}_z, \end{aligned} \quad (31)$$

with $\lambda_x = \lambda/\sin \theta_x$, $\lambda_y = \lambda/\sin \theta_y$ and $\lambda_+ = 2\lambda/(\cos \theta_x + \cos \theta_y)$.

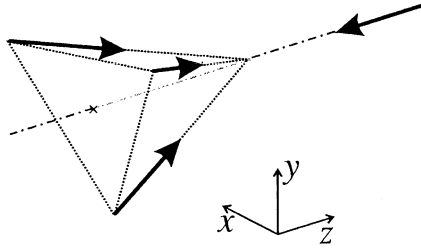


Fig. 8. Umbrella-like four-beam configuration.

Comments: (i) In the case of a four-beam 3D lattice, it is possible to cancel all the phases ϕ_i in expression (18) of the dipole potential through space translations. In fact, one can easily check that a translation $\mathbf{T} = \sum_{i=1,2,3} T_i \mathbf{a}_i$ where \mathbf{a}_i are the primitive translations defined by Eqs. (28) and $T_1 = -(\phi_1 - \phi_2)/2\pi$, $T_2 = -(\phi_1 - \phi_3)/2\pi$, $T_3 = -(\phi_1 - \phi_4)/2\pi$ gives such an expression of the potential.

(ii) The four-beam configurations usually give rise both to dipole and radiation pressure forces.

(iii) In the case where the set of primitive translations \mathbf{a}_1^* , \mathbf{a}_2^* and \mathbf{a}_3^* lie on the same plane, the potential is modulated along two directions only and the resulting potential may have a phase-dependent topography.

(iv) Another four-beam configuration has been used [13]. This umbrella-like configuration (Fig. 8) consists of one beam propagating along \mathbf{e}_z and three beams making the same angle θ with Oz and symmetrically located with respect to Oz (i.e. the beam configuration is invariant in a rotation of $2\pi/3$ around Oz). In the general case, the spatial periodicity of the potential corresponds to a trigonal lattice [14]. If the beams are propagating along the symmetry axis of a regular tetrahedron (i.e. when $\cos \theta = 1/3$), the lattice is cubic body-centred.

2.5.2. Configurations with more than four beams

Whereas all the four-beam configurations lead to the same class of potentials (periodic with a phase-independent topography), the situation is more complex when the configuration contains more than four beams. In the case of random beam directions, the potential will probably be quasiperiodic but it can be periodic (with possibly a superlattice structure) for some particular sets of wavevectors. Here again, an inspection of the lattice in the reciprocal space is generally useful to predict the lattice structure.

Consider a set of n beams ($n > 4$) with wavevectors \mathbf{k}_i . All the sites of the reciprocal lattice are obtained through a combination of $n - 1$ vectors $\mathbf{a}_1^* = \mathbf{k}_1 - \mathbf{k}_2, \dots, \mathbf{a}_{n-1}^* = \mathbf{k}_1 - \mathbf{k}_n$. If these vectors can be expanded along three of them with only rational coefficients, the lattice will be periodic and its topography will under most circumstances depend on the relative phases between the beams [41]. If this is not possible, the lattice is quasiperiodic [38]. We now describe the most widely used configuration with a number of beams larger than four. This is a six-beam configuration with three standing waves along the axis Ox , Oy and Oz (Fig. 9). The wavevectors of the six travelling waves are $\mathbf{k}_1 = k\mathbf{e}_x$, $\mathbf{k}_2 = k\mathbf{e}_y$, $\mathbf{k}_3 = k\mathbf{e}_z$, $\mathbf{k}_4 = -\mathbf{k}_1$, $\mathbf{k}_5 = -\mathbf{k}_2$ and $\mathbf{k}_6 = -\mathbf{k}_3$. The vectors \mathbf{a}_4^* and \mathbf{a}_5^* of the reciprocal lattice are respectively equal to $\mathbf{a}_3^* - \mathbf{a}_1^*$ and $\mathbf{a}_3^* - \mathbf{a}_2^*$. The potential generated by this beam configuration is thus periodic. A set of primitive

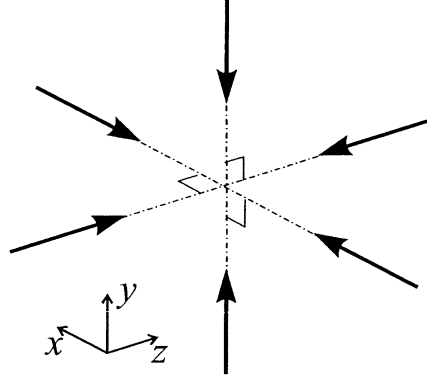


Fig. 9. The usual six-beam configuration consists of three standing waves along the three axis Ox, Oy, Oz .

translations is $\lambda \mathbf{e}_y, \lambda \mathbf{e}_z$ and $(\lambda/2)(\mathbf{e}_y + \mathbf{e}_z - \mathbf{e}_x)$, which shows that this is a cubic body-centred lattice.

Comment: Although the six-beam configuration of Fig. 9 generally leads to a potential with a phase-dependent topography, there are a few examples where the topography is phase-independent (for a scalar light-shift Hamiltonian). This is for instance the case if the beams \mathbf{E}_1 and \mathbf{E}_4 are y -polarized, the beams \mathbf{E}_2 and \mathbf{E}_5 z -polarized and the beams \mathbf{E}_3 and \mathbf{E}_6 x -polarized.

2.5.3. Talbot lattices

When a plane wave is sent through a mask displaying a periodic pattern, in many cases the transmitted field at a finite distance from the mask reproduces periodically the pattern of the mask. This is the Talbot effect [43–45] which can be used to achieve a periodic 3D lattice [46,47].

Consider a periodic mask in the $z=0$ plane with two independent primitive translations \mathbf{a}_1 and \mathbf{a}_2 . Because of the periodicity, the transmitted field just behind the mask can be expanded in Fourier series

$$\mathbf{E}(x, y, 0, t) = \text{Re} \left\{ \sum_{m,n \in \mathbb{Z}} E_{mn} \boldsymbol{\varepsilon} \exp i[(m\mathbf{a}_1^* + n\mathbf{a}_2^*) \cdot \mathbf{r}_\perp - \omega t] \right\}, \quad (32)$$

where $\boldsymbol{\varepsilon}$ is the beam polarization, \mathbf{a}_1^* and \mathbf{a}_2^* are primitive translations in the reciprocal space and $\mathbf{r}_\perp = x\mathbf{e}_x + y\mathbf{e}_y$.

After propagation the field becomes

$$\mathbf{E}(x, y, z, t) = \text{Re} \left\{ \sum_{m,n \in \mathbb{Z}} E_{mn} \boldsymbol{\varepsilon} \exp i[(m\mathbf{a}_1^* + n\mathbf{a}_2^*) \cdot \mathbf{r}_\perp + k'_{mn}z - \omega t] \right\}, \quad (33)$$

with (in the limit $m\mathbf{a}_1^*, n\mathbf{a}_2^* \ll k$)

$$k'_{mn} = k - \frac{1}{2k} [m^2(a_1^*)^2 + n^2(a_2^*)^2 + 2mna_1^* \cdot a_2^*]. \quad (34)$$

If it is possible to define k_T such as

$$\frac{(a_1^\star)^2}{2k} = p_1 k_T, \quad \frac{(a_2^\star)^2}{2k} = p_2 k_T, \quad \frac{(\mathbf{a}_1^\star \cdot \mathbf{a}_2^\star)^2}{k} = p k_T \quad \text{with } p_1, p_2, p \in \mathbb{Z} \quad (35)$$

then the distribution of the field intensity is identical in the planes $z=0$ and $z=q(2\pi/k_T)$, q being an integer. The dipole potential generated by this field is thus periodic with spatial periods a_1 and a_2 in the xOy plane and $z_T = (2\pi/k_T)$ along Oz . Note that z_T corresponds to the largest value of k_T for which Eqs. (35) are fulfilled.

Comments: (i) In the case of a square lattice ($\mathbf{a}_1^\star \cdot \mathbf{a}_2^\star = 0$ and $a_1^\star = a_2^\star = 2\pi/a_M$ where a_M is the spatial period of the mask), the Talbot period z_T is $z_T = 2a_M^2/\lambda$.

In this case, a supplementary translational symmetry of the dipole potential U is found using Eqs. (33) and (34):

$$U(\mathbf{R}_\perp, Z) = U\left(\mathbf{R}_\perp + \frac{\mathbf{a}_1 + \mathbf{a}_2}{2}, Z + \frac{z_T}{2}\right). \quad (36)$$

(ii) In the case of a hexagonal lattice ($\mathbf{a}_1^\star \cdot \mathbf{a}_2^\star = (a_1^\star)^2/2$ and $a_1^\star = a_2^\star = 4\pi/a_M\sqrt{3}$ where a_M is the spatial period of the mask), the Talbot period is $z_T = 3a_M^2/2\lambda$.

(iii) The Talbot lattice is closely connected to the lattices generated by several beams. Indeed the field given by Eq. (33) can be considered as the superposition of several beams having wavevectors \mathbf{k}_{mn} equal to $k'_{mn}\mathbf{e}_z + m\mathbf{a}_1^\star + n\mathbf{a}_2^\star$ and (complex) amplitudes E_{mn} . However the relationship between the phases of these beams is precisely determined by the transmission function of the mask and thus the topography of the potential is not sensitive to the phases.

(iv) In the case where the mask has a random transmission (i.e. is a diffuser), the transmitted light is a speckle field and one achieves a disordered dipole potential [47,48].

3. Sisyphus cooling in optical lattices

The potential depths that can be achieved in an optical lattice are so small that the trapping of atoms generally requires to cool them at very low temperatures. Fortunately, the same laser beams can often be used to create the lattice and to cool the atoms. This result is not surprising because one of the major cooling mechanism makes use of the topography of the optical potential to dissipate energy. In the Sisyphus effect [4,5,15], the atoms lose their kinetic energy because they continuously climb potential hills. In the first subsection (Section 3.1) we present the 1D $\text{lin} \perp \text{lin}$ configuration, the famous configuration used for the first analysis of the Sisyphus effect. We then present a rough estimate of the temperature in the case of a $J_g = 1/2 \rightarrow J_e = 3/2$ transition (Section 3.2) and we show that a significant fraction of the atoms are trapped in potential wells. Extensions of this configuration to 2D and 3D are presented in Section 3.3. Sisyphus cooling in dark or grey lattices is described in Section 3.4 and several configurations that differ from the $\text{lin} \perp \text{lin}$ case are finally presented in Section 3.5.

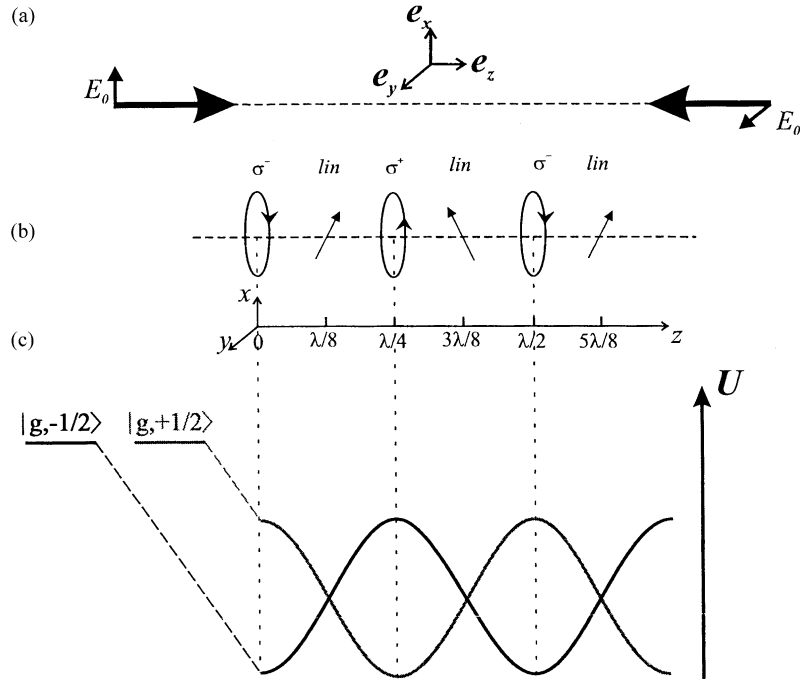


Fig. 10. (a) One-dimensional $\text{lin} \perp \text{lin}$ configuration. Two beams with cross-polarized linear polarizations are counter-propagating along the Oz axis. (b) The total field exhibits a polarization gradient with a $\lambda/2$ periodicity. (c) Light-shifts for a $J_g = 1/2 \rightarrow J_c = 3/2$ transition. The spatial modulation of the light-shifts originates from the polarization gradient. The extrema of the light-shift correspond to points where the polarization is circular. The figure drawn for $\Delta < 0$ shows that, because of optical pumping, the lowest sublevel (i.e. having the largest negative light-shift) also has the largest population.

3.1. The one-dimensional model

3.1.1. Field configuration: linearly cross-polarized counter-propagating beams

We describe here the traditional $\text{lin} \perp \text{lin}$ configuration used to explain the Sisyphe cooling [16]. Because of its simplicity it is also the starting point for the study of higher dimensional configurations. The 1D configuration consists of two counter-propagating beams having the same frequency ω and the same amplitude E_0 and crossed linear polarizations \mathbf{e}_x and \mathbf{e}_y (Fig. 10a). By an appropriate translation in phase and in time, it is possible to eliminate the phases of the beams (see Section 2.2) and the total electric field can be written as

$$\mathbf{E}(z, t) = \text{Re}\{[E^+(z)\mathbf{e}_+ + E^-(z)\mathbf{e}_-]\exp - i\omega t\}, \quad (37)$$

where \mathbf{e}_+ and \mathbf{e}_- are the unit vectors associated with the circular polarizations σ^+ and σ^- :

$$\mathbf{e}_{\pm} = \mp \frac{\mathbf{e}_x \pm i\mathbf{e}_y}{\sqrt{2}}, \quad (38)$$

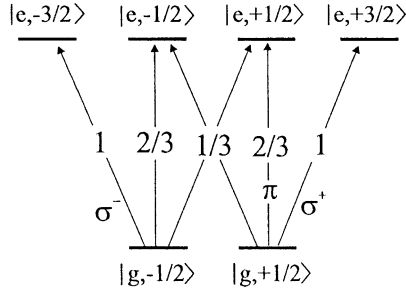


Fig. 11. Square of the Clebsch–Gordan coefficients for a $J_g = 1/2 \rightarrow J_e = 3/2$ transition.

and E^+ and E^- are the circular components of \mathbf{E} :

$$E^+(z) = -i\sqrt{2}E_0 \sin kz ,$$

$$E^-(z) = \sqrt{2}E_0 \cos kz . \quad (39)$$

The sites where the light polarization is purely circular are then $z=0, \lambda/2, \lambda, \dots$ for the σ^- polarization and $z=\lambda/4, 3\lambda/4, \dots$ for the σ^+ polarization (Fig. 10b). In general the polarization is elliptical.

Two fundamental and closely connected processes are at the basis of Sisyphus cooling: optical pumping [49] and light-shift [50]. Consider an atom having an angular momentum J_g in its ground state and assume that the field given by Eq. (37) is quasis resonant on a $J_g \rightarrow J_e$ transition. Because of optical pumping [49], the atoms are transferred to a Zeeman substate $m_g = +J_g$ at points where the light is σ^+ polarized and to a substate $m_g = -J_g$ at points where the light polarization is σ^- .

3.1.2. The situation of a $J_g = 1/2 \rightarrow J_e = 3/2$ transition

Physical processes are usually studied in the simple case of a $J_g = 1/2 \rightarrow J_e = 3/2$ transition (Fig. 11). The populations Π_+ and Π_- of the two Zeeman substates $m_g = +1/2$ and $m_g = -1/2$ are solutions of the optical pumping equations

$$\begin{aligned} \frac{d}{dt}\Pi_+ &= \Gamma_p \left[\frac{I^+}{I} \Pi_- - \frac{I^-}{I} \Pi_+ \right] , \\ \frac{d}{dt}\Pi_- &= \Gamma_p \left[\frac{I^-}{I} \Pi_+ - \frac{I^+}{I} \Pi_- \right] , \end{aligned} \quad (40)$$

where $I^\pm = |E^\pm|^2$, $I = I^+ + I^-$ and Γ_p is the optical pumping rate. Its value is $\Gamma_p = \frac{2}{9}\Gamma s_0$, Γ being the radiative width of the upper level and s_0 the saturation parameter

$$s_0 = \frac{\Omega_1^2/2}{\Delta^2 + \Gamma^2/4} . \quad (41)$$

In this expression, $\Delta = \omega - \omega_0$ is the detuning from the atomic resonance and Ω_1 is the resonant Rabi frequency for one travelling wave of amplitude E_0 and for a transition having a Clebsch–Gordan coefficient equal to 1.

Using $\Pi_+ + \Pi_- = 1$, Eqs. (40) can be written as

$$\begin{aligned}\frac{d}{dt}\Pi_+ &= -\Gamma_p(\Pi_+ - \Pi_+^{\text{st}}), \\ \frac{d}{dt}\Pi_- &= -\Gamma_p(\Pi_- - \Pi_-^{\text{st}}),\end{aligned}\tag{42}$$

where $\Pi_+^{\text{st}} = \sin^2 kZ$ and $\Pi_-^{\text{st}} = \cos^2 kZ$ are the steady-state populations for a stationary atom located in Z .

The coupling between atom and light also produces level shifts [50]. These light-shifts are particularly simple to evaluate in the case of the $J_g = 1/2 \rightarrow J_e = 3/2$ transition because there is no Raman coupling between $m_g = -1/2$ and $m_g = +1/2$ when the field has only σ^+ and σ^- components. The light-shift Hamiltonian is thus diagonal in the basis ($|m_g = -1/2\rangle, |m_g = +1/2\rangle$) with eigenvalues

$$\begin{aligned}U_+ &= 2\hbar\Delta'_0 \left(\frac{I^+}{I} + \frac{I^-}{3I} \right), \\ U_- &= 2\hbar\Delta'_0 \left(\frac{I^-}{I} + \frac{I^+}{3I} \right),\end{aligned}\tag{43}$$

where $\Delta'_0 = \Delta s_0/2$ is the light-shift *per beam* for a closed transition having a Clebsch–Gordan coefficient equal to 1. Because I^+ and I^- depend on the position \mathbf{R} of the atom, U_+ and U_- are also space dependent. They act as a potential in the same way as the dipole potential considered in Section 2, but this is now a bipotential which depends on the internal state of the atom. When $\Delta < 0$, the largest population is found in the lowest potential curve.

Instead of Δ'_0 , one can express the light-shifts in terms of the depth $U_0 = -\frac{4}{3}\hbar\Delta'_0$ of the optical potential (Fig. 10c):

$$U_{\pm} = \frac{U_0}{2} [-2 \pm \cos 2kZ].\tag{44}$$

As mentioned before, Sisyphus cooling originates from a combination of optical pumping and light-shift. Consider an atom initially located in the U_- potential curve in $Z=0$ and moving in the $+Oz$ direction. If its velocity is such that it travels over a distance on the order of $\lambda/4$ in an optical pumping time Γ_p^{-1} , the atom climbs a potential hill, reaches the domain where the light is mostly σ^+ polarized and undergoes an optical pumping process which brings it in the potential valley corresponding to U_+ . From there, a similar sequence can be repeated. The atom thus almost always climbs potential hills, and therefore its kinetic energy decreases. In fact the kinetic energy is first transformed into potential energy and finally dissipated in the spontaneous emission that accompanies the optical pumping process. An important feature of this mechanism is its nonadiabaticity. Because of the time-lag $\sim \Gamma_p^{-1}$ associated with optical pumping, the relative populations of moving atoms differ from the values Π_{\pm}^{st} evaluated for

atoms at rest. We show in Section 3.2 that the friction force associated with Sisyphus cooling can be calculated from the actual values of Π_{\pm} .

Comments: (i) The coefficient $2/9$ that appears in the formula giving the optical pumping rate originates from the Clebsch–Gordan coefficients of the $J_g = 1/2 \rightarrow J_e = 3/2$ transition (Fig. 11). To have a less specific reference, the photon scattering rate per beam $\Gamma'_0 = \Gamma s_0/2$ for a transition having a Clebsch–Gordan coefficient equal to 1 is often introduced.

(ii) The damping of the atomic velocity in the Sisyphus mechanism can also be interpreted as arising from a *redistribution of photons* between the two incident travelling waves. In a Raman process where the atom absorbs a photon propagating along $-Oz$ and emits a photon propagating in the opposite direction, the atomic momentum is changed by $-2\hbar k$. The succession of these Raman processes permits to reduce the atomic velocity. This photon redistribution in the $\text{lin} \perp \text{lin}$ configuration was studied in [51].

3.1.3. Case of a $J_g \rightarrow J_e = J_g + 1$ transition with $J_g > 1/2$

In the case where the ground state has an angular momentum $J_g > 1/2$, the light-shift Hamiltonian \hat{U} is not diagonal because two sublevels m and $m + 2$ of the ground state are coupled by a Raman process involving the absorption of a photon σ^+ and the stimulated emission of a photon σ^- . This implies that the eigenstates $|\Phi_n\rangle$ of \hat{U} do not generally coincide with the Zeeman substates $|m\rangle$. The operator \hat{U} can be written as [16] (see Section 4.1)

$$\hat{U}(\mathbf{R}) = \hbar \Delta'_0 \frac{E_0^2(\mathbf{R})}{E_0^2} [\boldsymbol{\varepsilon}^*(\mathbf{R}) \cdot \hat{\mathbf{d}}^-][\boldsymbol{\varepsilon}(\mathbf{R}) \cdot \hat{\mathbf{d}}^+], \quad (45)$$

where $E_0(\mathbf{R})$ is the (real) field amplitude in \mathbf{R} , $\boldsymbol{\varepsilon}(\mathbf{R})$ is the (generally complex) local polarization and $\hat{\mathbf{d}}$ is the reduced dipole operator, the matrix elements of $\mathbf{e}_q(\mathbf{R}) \cdot \hat{\mathbf{d}}^+$ (with $q = -1, 0, 1$) being the Clebsch–Gordan coefficients for the $J_g \rightarrow J_e$ transition (see also Section 4.1).

The eigenstates $|\Phi_n\rangle$ and the eigenvalues U_n of \hat{U} are generally space dependent:

$$\hat{U}(\mathbf{R}) = \sum_n U_n(\mathbf{R}) |\Phi_n(\mathbf{R})\rangle \langle \Phi_n(\mathbf{R})|. \quad (46)$$

The $|\Phi_n\rangle$ correspond to the adiabatic basis and the U_n are the *adiabatic* energies. We have plotted them in Fig. 12a in the case of the $J_g = 4 \rightarrow J_e = 5$ transition.

Comments: (i) For several problems, the detailed knowledge of $|\Phi_n(\mathbf{R})\rangle$ and $U_n(\mathbf{R})$ everywhere is not necessary. For example, one can be interested only in the dynamics of the atoms close to the minima of the potential curves. Because the minima are located at points where the light has a pure circular polarization σ^+ or σ^- , the Raman couplings are small and the light-shift eigenstates are nearly equal to the Zeeman substates $|m\rangle$. Near those points, a reasonable approximation for the light-shift operator is

$$\hat{U}(\mathbf{R}) \simeq \sum_m V_m(\mathbf{R}) |m\rangle \langle m|, \quad (47)$$

where the $V_m(\mathbf{R}) = \langle m | \hat{U}(\mathbf{R}) | m \rangle$ are the diagonal elements of $\hat{U}(\mathbf{R})$. The V_m are often called the *diabatic* energies (and the Zeeman substates $|m\rangle$ represent then the diabatic basis). These diabatic potentials are compared to the adiabatic potentials in Fig. 12.

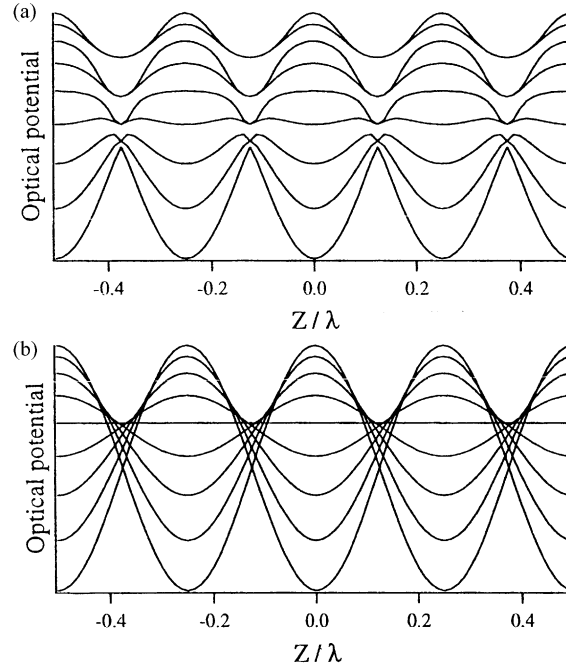


Fig. 12. Optical potentials for a $J_g = 4 \rightarrow J_e = 5$ transition in the $\text{lin} \perp \text{lin}$ configuration for $\Delta < 0$. (a) Adiabatic potentials. (b) Diabatic potentials. The two sets of curves are similar away from the level anti-crossings of the adiabatic potentials. In particular, the potentials have a nearly identical curvature at the minima, located at points where the light polarization is circular.

(ii) The picture of velocity damping given in Section 3.1.2 in the case of a $J_g = 1/2 \rightarrow J_e = 3/2$ transition implies that the atom travels over several potential wells and hills to dissipate its kinetic energy. Another picture involving *local cooling* is also possible for levels of higher angular momentum. The light-shifts presented in Fig. 12 exhibit several wells around the same site of circular polarization, the deepest well being associated with a level for which $|m| = J_g$. Because optical pumping tends to accumulate the atoms in this level near the minima while it redistributes the populations among the various levels away from these points, a local cooling scheme where the atom travels over a distance smaller than $\lambda/4$ is possible, as shown in Fig. 13. In this process, the atom climbs the deepest potential well from A to B , is then optically pumped into another well having a smaller curvature where it comes down from C to D , and finally returns to the deepest well in another optical pumping process [52].

3.1.4. Motional coupling and topological potential

The description of the Hamiltonian motion in the adiabatic basis is not always straightforward, because the $|\Phi_n(\mathbf{R})\rangle$ are space dependent and nonadiabatic coupling terms proportional to $\langle \Phi_m | \nabla_Z \Phi_n \rangle$ thus connect different potential curves ($|\nabla_Z \Phi_n\rangle$ is a short notation for $\nabla_Z(|\Phi_n\rangle)$). The order of magnitude of these motional terms is $\hbar kv$ with v the atomic velocity (see Section 3.4.2 for an example). As long as $\hbar kv \ll |U_m - U_n|$, the adiabatic approximation is valid and the motional terms can be neglected.

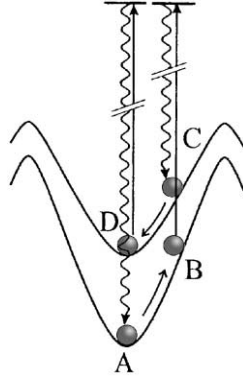


Fig. 13. Local cooling for a transition starting from a fundamental level having an angular momentum J_g larger than $1/2$ (typically, $J_g \geq 2$).

When necessary, it is possible to have a more convenient image in the diabatic basis. This results in the addition of a topological potential [53] to the light-shift Hamiltonian. To understand the origin of this term we start from the Hamiltonian H_{eff} of the atom in the light field

$$H_{\text{eff}} = \frac{P_Z^2}{2M} + \sum_n U_n |\Phi_n\rangle \langle \Phi_n|, \quad (48)$$

and we apply to H_{eff} a unitary transformation T which transforms the adiabatic basis into the diabatic basis:

$$T = \sum_m |m\rangle \langle \Phi_m|. \quad (49)$$

The transform of the light-shift Hamiltonian gives

$$T \hat{U} T^\dagger = \sum_n U_n |n\rangle \langle n|. \quad (50)$$

To calculate the kinetic term, we note that

$$[T, P_Z] = i\hbar \frac{\partial T}{\partial Z} = i\hbar \sum_m |m\rangle \langle \nabla_Z \Phi_m|. \quad (51)$$

This leads to

$$T P_Z T^\dagger = P_Z + i\hbar \sum_{m,n} \langle \nabla_Z \Phi_m | \Phi_n \rangle |m\rangle \langle n|. \quad (52)$$

After some straightforward algebra, the Hamiltonian in the new representation can be written as

$$T H_{\text{eff}} T^\dagger = \frac{1}{2M} (P_Z + A_t)^2 + \sum_n U_n |n\rangle \langle n| + U_t + C_t, \quad (53)$$

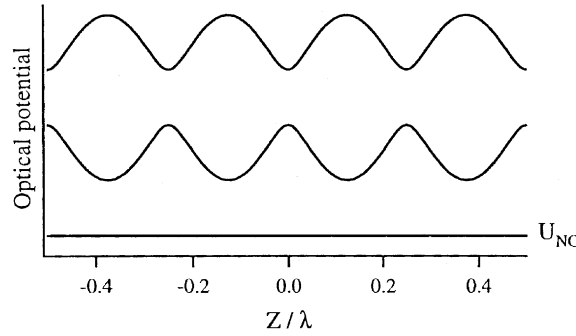


Fig. 14. Adiabatic potentials for a $J_g = 2 \rightarrow J_e = 2$ transition in the $\text{lin} \perp \text{lin}$ configuration for $\Delta > 0$. The lowest potential curve is flat because the corresponding eigenstate is not coupled to the excited state. Sisyphus cooling originates from nonadiabatic transitions near the anticrossing points. The two upper curves have a two-fold degeneracy.

with

$$A_t = i\hbar \sum_m \langle \nabla_Z \Phi_m | \Phi_m \rangle, \quad (54)$$

$$U_t = \frac{\hbar^2}{2M} \sum_m [\langle \nabla_Z \Phi_m | \nabla_Z \Phi_m \rangle - |\langle \nabla_Z \Phi_m | \Phi_m \rangle|^2] |m\rangle \langle m|, \quad (55)$$

and where C_t is an operator that couples different states $|m\rangle$ and $|n\rangle$. The matrix elements of A_t , U_t and C_t are very small. Typical orders of magnitude for U_t and C_t are, respectively, the recoil energy $E_R = \hbar^2 k^2 / (2M)$ and $k\bar{v}$ (where \bar{v} is the mean quadratic velocity). Therefore, when the $|U_m - U_n|$ are very large compared to $k\bar{v}$, it is legitimate to neglect the effect of C_t and to use

$$H_t = \frac{1}{2M} (P_Z + A_t)^2 + \sum_n U_n |n\rangle \langle n| + U_t \quad (56)$$

as an approximate Hamiltonian. Because of their analogies with the vector and scalar potentials in electromagnetism, A_t and U_t are called topological potentials.

Comment: The effect of these topological potentials on the atomic dynamics has been recently observed in a 1D $\text{lin} \perp \text{lin}$ optical lattice filled with ^{87}Rb atoms [218]. Indeed, the dependence of the lowest-band tunnelling period on the depth of the adiabatic potential can only be explained by additional gauge potentials.

3.1.5. Transitions accommodating an internal dark state

For transitions connecting two levels of same angular momentum ($J_g = J_e$) with J_g integer and for transitions $J_g \rightarrow J_e = J_g - 1$, there exists internal dark states [17,54–56]. These states correspond to a linear superposition of Zeeman substates for which the matrix elements of $\mathbf{e}(\mathbf{R}) \cdot \mathbf{d}$ (\mathbf{d} electric dipole moment) with any substate of the excited level is equal to 0. As a result, the light-shift of these internal dark states $|\Phi_{\text{NC}}\rangle$ is 0. The adiabatic potentials for a $J_g = 2 \rightarrow J_e = 2$ transition, displayed in Fig. 14, show the occurrence of such a state (there is one internal dark state for $J_g = J_e$ integer and two for $J_e = J_g - 1$). In steady state and for atoms at rest, optical pumping collects all the population in these internal dark states from which they cannot escape by absorbing radiation.

Sisyphus cooling is also possible in this situation, but it occurs for a blue detuning ($\Delta > 0$) and the mechanism is slightly different [57–59]. Consider an atom moving at velocity v on the flat potential of Fig. 14. Because of the motional coupling a nonadiabatic transition is possible from $|\Phi_{\text{NC}}\rangle$ to another eigenstate $|\Phi_{\text{C}}\rangle$ of the light-shift operator (when $\langle \Phi_{\text{C}} | \nabla_Z \Phi_{\text{NC}} \rangle \neq 0$) and such a transition has a maximum probability to occur near the anticrossing between these two potential curves. The atom then climbs a potential hill in the state $|\Phi_{\text{C}}\rangle$ and when it returns into $|\Phi_{\text{NC}}\rangle$ through an optical pumping process, it has lost a fraction of its kinetic energy.

Comment: We use the term dark state only in the situations where the internal dark state is also an eigenstate of the kinetic energy operator. In this case indeed, an additional cooling process using velocity selective coherent population trapping (VSCPT) occurs [60].

3.2. Kinetic temperature

The Sisyphus mechanism allows to damp the atomic velocity. To find out the temperature, it is necessary to know more precisely the friction force and the fluctuation processes that prevent a complete freezing of the motion.

3.2.1. Friction force for a $J_g = 1/2 \rightarrow J_e = 3/2$ transition

Consider an atom moving at velocity v along Oz in the $\text{lin} \perp \text{lin}$ configuration. To evaluate the friction force, we calculate the populations $\Pi_+(t) = \frac{1}{2} + p(t)$ and $\Pi_-(t) = \frac{1}{2} - p(t)$ for an atom following a trajectory $Z = vt$. Using Eq. (42), we find

$$p(t) = -\frac{1}{2} \frac{\Gamma_p^2}{\Gamma_p^2 + 4k^2v^2} \cos 2kvt - \frac{\Gamma_p kv}{\Gamma_p^2 + 4k^2v^2} \sin 2kvt. \quad (57)$$

If there was no *time-lag*, the second term in the right-hand side of Eq. (57) would vanish. We assume that the atom evolves in the jumping regime, i.e. that it makes frequent jumps between the two potential curves of Fig. 10c when it travels over one spatial period. In this case, the force acting on the atom is the average value of the dipole force:

$$\bar{F} = -\Pi_+ \nabla_Z U_+ - \Pi_- \nabla_Z U_- . \quad (58)$$

Using Eqs. (44) and (57) and averaging over a time period long compared to $(kv)^{-1}$, one finds [4]

$$\bar{F} = -k^2v \frac{\Gamma_p U_0}{\Gamma_p^2 + 4k^2v^2} . \quad (59)$$

In the limit of low velocity ($kv \ll \Gamma_p$), Eq. (59) describes a friction force $-\alpha v$ with a friction coefficient $\alpha = -3\hbar k^2(\Delta/\Gamma)$. As expected, damping is found for red detuned beams ($\Delta < 0$).

Comments: (i) Eq. (59) shows that the friction is efficient for atoms having a velocity $2kv \leq \Gamma_p$. The velocity $v_c = \Gamma_p/2k$ is known as the *capture velocity* for the Sisyphus mechanism. For atoms faster than v_c , Doppler cooling [23,61] can damp the velocities.

(ii) An atom with a very weak velocity is submitted to an average dipole force equal to

$$\bar{F} = -\Pi_+^{\text{st}} \nabla_Z U_+ - \Pi_-^{\text{st}} \nabla_Z U_- . \quad (60)$$

In this 1D situation, an average dipole potential can be defined through the relation $\bar{F} = -\nabla_Z \bar{U}$ with $\bar{U} = (U_0/4) \sin^2 2kZ$.

3.2.2. Momentum diffusion coefficient

The most important heating process in the Sisyphus mechanism arises from the fluctuations of the dipole force that occur when the atom jumps from one level to the other. To estimate the diffusion coefficient associated with this process, we note that when the atom remains in the potential curve U_+ for a time Γ_p^{-1} , its momentum changes by an amount $(\nabla_z U_+) \Gamma_p^{-1} \sim k U_0 \Gamma_p^{-1}$. When the atom jumps back and forth between U_+ and U_- , it thus performs a random walk in the momentum space with elementary steps on the order of $k U_0 \Gamma_p^{-1}$. Because the time interval between two steps is on the order of Γ_p^{-1} , the momentum diffusion coefficient D can be estimated to be on the order of $k^2 U_0^2 / \Gamma_p$. In fact, a precise calculation gives [4]

$$D = \frac{3}{2} \hbar^2 k^2 \Delta'_0 \frac{\Delta}{\Gamma}. \quad (61)$$

The equilibrium temperature T , found from the Einstein relation $k_B T = D/\alpha$, is thus

$$k_B T = -\frac{1}{2} \hbar \Delta'_0. \quad (62)$$

The ratio $k_B T / U_0 = 3/8$ is relatively small and a good localization in the potential wells is thus expected.

Comments: (i) There are some other contributions to the momentum diffusion coefficient. As known from the theory of Doppler cooling [16,61], one should also consider the fluctuations of the momentum carried away by fluorescence photons and the fluctuations in the difference between the number of photons absorbed in each travelling wave. These two processes lead to a contribution to D which is on the order of $\hbar^2 k^2 \Gamma'_0$. However, in the limit $|\Delta| \gg \Gamma$, the contribution given by Eq. (61) is dominant and the temperature is only a function of Δ'_0 . In this limit, T is thus proportional to I/Δ . Such a dependence is no longer expected for very small detunings $|\Delta| \sim \Gamma$ because the additional terms coming from the diffusion processes described above should then be included in the model.

(ii) Instead of Δ'_0 or U_0 , one uses sometimes the light-shift Δ' at a point where the light polarization is circular. For the 1D lin \perp lin configuration, $\Delta' = 2\Delta'_0$.

(iii) In the theory of brownian motion, the spatial diffusion coefficient D_{sp} is related to the temperature T and the friction coefficient α through the relation [62]

$$D_{\text{sp}} = \frac{k_B T}{\alpha}. \quad (63)$$

Using Eq. (62) and the value of α found in Section 3.2.1, this yields for $D_{\text{sp}} M / \hbar$ (which is a dimensionless quantity) a value equal to $\Gamma'_0 / 12 \omega_R$ (where $\omega_R = E_R / \hbar$ is the recoil frequency). Note however that Γ'_0 cannot be infinitely small because we assumed that the atom jumps several times between the two potential curves when it travels over λ . In fact, the jumping regime condition for delocalized atoms is $k v \ll \Gamma_p$. Because $M v^2 \sim U_0$ and $\Gamma_p \sim \Gamma'_0$, this condition can be written $\Gamma'_0 / \omega_R \gg |\Delta| / \Gamma$. Therefore we expect $D_{\text{sp}} M / \hbar \geq |\Delta| / \Gamma$.

However, this model has a restricted range of validity. If $|\Delta'_0| / \omega_R$ is not large enough, there are many atoms for which the friction force is not linear in v (see Eq. (59)) and this leads to a divergence of D_{sp} . Using the complete friction force (Eq. (59)) and an analogous equation for D , Hodapp et al. [62] were able to derive a formula for D_{sp} which coincides with the value $\Gamma'_0 / 12 \omega_R$ for $|\Delta'_0| / \omega_R \gg 1$ and shows a divergence for $|\Delta'_0| / \omega_R = 135$. Furthermore, from a more general point of view, these models do not describe accurately the contribution of localized

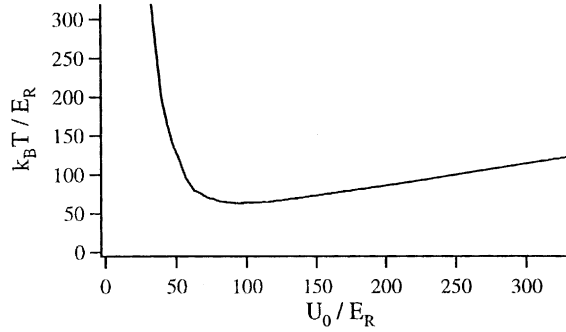


Fig. 15. Kinetic temperature versus depth of the optical potential in the $\text{lin} \perp \text{lin}$ configuration, for a $J_g = 1/2 \rightarrow J_e = 3/2$ transition. The calculation was performed using a semi-classical Monte-Carlo simulation (see Section 4.3).

atoms and more sophisticated methods are often necessary to predict quantitatively the value of D_{sp} [63].

(iv) Because an atom moving at velocity v interacts in its own frame with two waves having Doppler-shifted frequencies $\omega_1 = \omega - kv$ and $\omega_2 = \omega + kv$, the dependence on kv of the friction force (Eq. (59)) implies that for an atom at rest, the redistribution of photons between two waves of frequency ω_1 and $\omega_2 = \omega_1 + \delta$ has a dispersive shape when δ is swept, with a peak to peak distance equal to $2\Gamma_p$. This stimulated Rayleigh resonance has indeed been studied in the context of nonlinear optics [51,64].

3.2.3. Temperature versus potential depth

In Sections 3.2.1 and 3.2.2, it was assumed that an atom makes frequent jumps between the two potential curves of Fig. 10c when it travels over one wavelength. This jumping regime corresponds however to a restricted range of parameters. For a $J_g = 1/2 \rightarrow J_e = 3/2$ transition, a more general derivation of the kinetic temperature can be obtained by solving the Fokker–Planck equation in the bipotential using a Monte-Carlo simulation [65,66] (see also Section 4.3) or with the band model [67] (see also Section 4.2). These two approaches give a similar dependence for the temperature which varies linearly with U_0 for large values of U_0 and exhibits a sharp increase at small U_0 (see Fig. 15). In the asymptotic regime, the slope $k_B T / U_0$ is equal to 0.28, which is slightly smaller than the one predicted in Section 3.2.2. The sharp increase at low U_0 is often called “decrochage”. It occurs because in this case the energy dissipated in a Sisyphus process, which is always less than U_0 , cannot efficiently compensate the recoil energy transferred to the atom in an optical pumping process. The minimum temperature is on the order of $60E_R$ (which corresponds to an average value of $5.5\hbar k$ for the momentum) and is found for $U_0 \simeq 95E_R$. The orders of magnitude rather than the exact numbers are important here because similar values are found in most Sisyphus processes and for most transitions.

Comments: (i) Quantitative calculations of the variations of T versus Δ'_0 were performed for various transitions with $J_g \geq 1$ [52,68,69]. For all of the $J_g \rightarrow J_e = J_g + 1$ transitions (with $\Delta < 0$) and for most of the transitions accommodating an internal dark state (with $\Delta > 0$), a variation similar to the one of Fig. 15 is observed. The only exceptions correspond to situations

where none of the potential curves is spatially modulated and Sisyphus cooling vanishes. This is the case for the $J_g = 1 \rightarrow J_e = 1$ transition in the $\text{lin} \perp \text{lin}$ configuration, but another cooling mechanism (VSCPT) occurs for this transition [60].

(ii) In practical situations, when there are several hyperfine sublevels, it is not always possible to describe quantitatively the temperature with a model using a well-isolated transition. This is in particular the case in the neighbourhood of a transition accommodating an internal dark state because the cooling arising from nonadiabatic couplings has a weak efficiency (see Section 3.4.2). The effect of distant transitions can therefore be significant in this case [70,71].

3.2.4. Oscillating and jumping regimes

Because $k_B T < U_0$, many atoms are found inside a potential well where they oscillate. If we call Ω_v the oscillation frequency in a well associated to U_+ or U_- ($\Omega_v = 2\sqrt{E_R U_0}/\hbar$), the situations $\Omega_v \ll \Gamma_p$ and $\Omega_v \gg \Gamma_p$ are naturally separated. In the first case, an atom makes several jumps during an oscillation period and this corresponds to the jumping regime. Note that because $U_0 \sim Mv^2$, the condition for the jumping regime can be written $kv \ll \Gamma_p$. The opposite condition describes the case where the atom performs several oscillations between two optical pumping processes, and it corresponds to the oscillating regime.

In fact, a further inspection of the border between these domains should be performed when considering localized atoms [72]. Consider for example an atom in the σ^- well centred in $z = 0$. The probability to jump in the U_+ potential curve is $\Gamma_p I^+/I$ (see Eq. (40)) i.e. $\Gamma_p \sin^2 kz$. If the amplitude of the oscillation motion is a $\ll \lambda$ (*Lamb–Dicke* regime), the border between the oscillating and jumping regimes is found for $\Omega_v \sim \Gamma_p (ka)^2$. The oscillating regime domain has increased to the detriment of the jumping regime.

3.2.5. Distribution of population in the quantum approach

In the quantum approach, the description in terms of band structure is appropriate because of the periodicity of the potential (Fig. 16a, see also Section 4.2). If we consider a single potential well, we can find a set of eigenenergies E_n and eigenstates $|\psi_n\rangle$. Due to the tunnelling effect, the eigenstates of two different wells having the same energy are coupled: this process gives rise to the band structure. However, for $U_0 \gg E_R$ and for the deepest bound states, the tunnelling rate is generally very weak compared to the photon scattering rate and can be neglected. (The situation can however be different in far-detuned optical lattices [73–79] where dissipation is very small.) One can thus use a description either in terms of band structure or in terms of well localized eigenstates, according to one's convenience.

In the case of the $J_g = 1/2 \rightarrow J_e = 3/2$ transition, the distribution of population in the various bands (Fig. 16a) was calculated by Castin and Dalibard [67]. Fig. 16b shows the variation of the populations π_n of the lowest energy bands versus the depth of the optical potential. For example, the population of the lowest band π_0 reaches a maximum on the order of 33% for $U_0 \simeq 60E_R$. As expected, for large U_0 most of the population is found in the bands associated with the bound levels of a well.

The population in each band results from rate equations. In the feeding and emptying processes, two kinds of terms can be distinguished: the first terms are associated to optical pumping

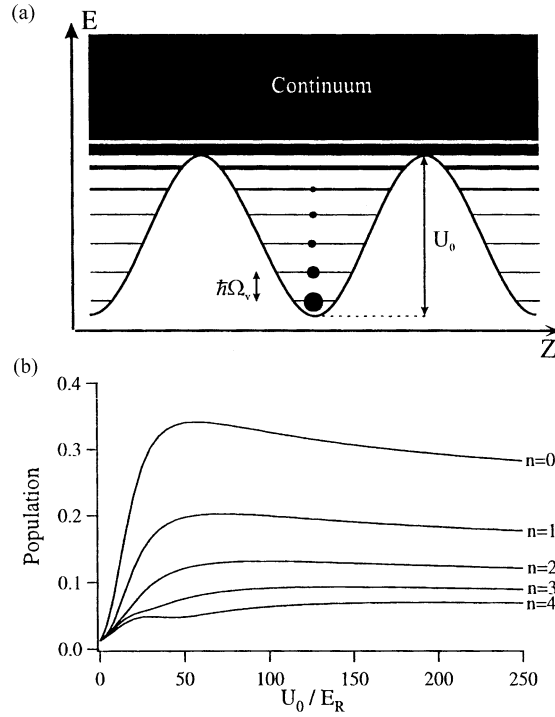


Fig. 16. (a) Position and population of the bands for the $J_g = 1/2 \rightarrow J_e = 3/2$ transition and for $U_0 = 100E_R$. Only the potential curve $U_-(Z)$ has been plotted. (b) Population of the lowest bands versus U_0/E_R . From Castin and Dalibard [67].

processes inducing a transfer between potential curves and the second terms correspond to the redistribution of population between the various bands inside a given potential.

Following Courtois and Grynberg [72], we now study the flux of population from the level $|\psi_n^{(-)}\rangle$ in the potential U_- , starting with the transfer towards the levels of U_+ . From Eq. (40), we estimate this transition rate to be

$$\sum_l \Gamma(n_- \rightarrow l_+) = \Gamma_p \langle \psi_n^{(-)} | \frac{I^+}{I} | \psi_n^{(-)} \rangle. \quad (64)$$

When $|\psi_n^{(-)}\rangle$ corresponds to a deeply bound level, it is possible to replace $U_-(Z)$ with its harmonic approximation. For example, near $Z=0$ we find

$$U_-(Z) \simeq -\frac{3}{2}U_0 + U_0 k^2 Z^2 \simeq -\frac{3}{2}U_0 + \frac{1}{2}M\Omega_v^2 Z^2, \quad (65)$$

with $\hbar\Omega_v = 2\sqrt{E_R U_0}$. In this limit, $|\psi_n^{(-)}\rangle$ is nearly equal to the eigenstate $|n\rangle_{\text{ho}}$ of the harmonic oscillator. From Eq. (39) we find $I^+(Z) \simeq 2E_0^2 k^2 Z^2$ and therefore

$$\sum_l \Gamma(n_- \rightarrow l_+) = \Gamma_p (2n+1) \frac{E_R}{\hbar\Omega_v}. \quad (66)$$

Optical pumping from the deepest bound states is thus much smaller than Γ_p because of the Lamb–Dicke factor $E_R/\hbar\Omega_v$.

Consider now the transition rate between two levels of the same potential. An atom in the $|\psi_n^{(-)}\rangle$ level can absorb a σ^- photon from the lattice beams and spontaneously emit a σ^- photon of wavevector \mathbf{k}' to end in the $|\psi_l^{(-)}\rangle$. The transition amplitude for this process is proportional to $\langle\psi_l^{(-)}|E^-(Z)e^{-i\mathbf{k}'\cdot\mathbf{R}}|\psi_n^{(-)}\rangle$. In the case of deeply bound levels (Lamb–Dicke regime), we can use the eigenstates of the harmonic oscillator and expand $E^-(Z)e^{-i\mathbf{k}'\cdot\mathbf{R}}$ in the vicinity of the potential minimum. For example, near $Z=0$ $E^-(Z)e^{-i\mathbf{k}'\cdot\mathbf{R}} = 1 - i\mathbf{k}'\cdot\mathbf{R} + \dots$. The zeroth order transition amplitude differs from 0 only if $l=n$. Therefore, it does not contribute to a redistribution of population. The first order term allows transitions from $|n\rangle_{\text{ho}}$ to the neighbour levels $|n-1\rangle_{\text{ho}}$ and $|n+1\rangle_{\text{ho}}$. Because of the matrix element ${}_{\text{ho}}\langle l|\mathbf{k}'\cdot\mathbf{R}|n\rangle_{\text{ho}}$, the transition rate includes the Lamb–Dicke factor. A detailed calculation also including the possibility of absorbing and emitting a σ^+ photon gives

$$\sum_{l \neq n} \Gamma(n_- \rightarrow l_-) = \frac{11}{9} \Gamma'_0 \left(n + \frac{1}{2} \right) \frac{E_R}{\hbar\Omega_v}. \quad (67)$$

Because $\Gamma_p = (4/9)\Gamma'_0$, the two rates given by Eqs. (66) and (67) are on the same order. The lifetime of the deepest levels is thus considerably longer than the average time between two scattering events because of the Lamb–Dicke factor.

Note however that the photon scattering rate from a deeply bound level is not reduced with respect to that of a free atom, but most of the scattering events correspond to *elastic* processes where the final state coincides with the initial one. (In the preceding calculation, these processes are associated to the zeroth order term in the expansion versus $\mathbf{k}\cdot\mathbf{R}$.) For atoms in these deeply bound states, the Rayleigh scattering should be significantly larger than the inelastic scattering [72]. This result, which has been confirmed experimentally [3], is strongly connected with the Mossbauer and Lamb–Dicke effects [8,80–82].

Comments: (i) For atoms in the deeply bound levels, the condition for the oscillating regime is $\Gamma'_0(E_R/\hbar\Omega_v) \ll \Omega_v$ which is equivalent to $\Gamma \ll |\Delta|$.

Note that it is possible to have an oscillating regime for the lowest levels and a jumping regime for levels of higher energy.

(ii) In the case of the $J_g = 1/2 \rightarrow J_e = 3/2$ transition, the redistribution of population inside one well (Eq. (67)) and the transfer to the other potential curves (Eq. (66)) have the same order of magnitude. In the case of transitions $J_g = J \rightarrow J_e = J + 1$ with higher J_g value, the transfer to other potential curves is reduced for tightly bound levels because the Clebsch–Gordan coefficient connecting $m_g = J$ to $m_e = J - 1$ is a decreasing function of J .

(iii) The populations of the bands show a very smooth variation with the potential depth in Fig. 16b. Such a behaviour is not found for transitions starting from a level of higher angular momentum (typically $J_g \geq 2$). Sharp resonances are then superimposed on broader curves similar to those shown in Fig. 16b. These resonances appear when a high energy band of the lowest potential curve is nearly degenerate with a band of another potential curve. Because of their coupling, the feeding of the lowest bands can be highly modified [83].

(iv) In the case of a $J_g = J \rightarrow J_e = J + 1$ transition with $J \geq 1$, there is in addition to Eqs. (66) and (67) a supplementary term that empties bound levels. This term originates from the fact that the adiabatic states do not coincide with the Zeeman states. For instance, the eigenstate $|\Phi_{-J}\rangle$ of lowest energy U_{-J} coincides with $|m = -J\rangle$ in $z = 0$ where the polarization of light is σ^- but has a $|m = -J + 2\rangle$ component proportional to $E_+(z)/E_-(z)$ near $z = 0$. Because of this component, an atom can leave a tightly bound level in U_{-J} by absorbing a σ^- photon to reach the U_{-J+2} , U_{-J+1} or U_{-J} potential at the end of the scattering process. Here again the harmonic approximation permits to evaluate this transition rate, and its order of magnitude is similar to the one in Eq. (66).

3.3. Generalization to higher dimensions

3.3.1. Circular components of the field—spatial periodicity

To summarize, the essential features of the 1D $\text{lin} \perp \text{lin}$ configurations are: (i) the σ^+ and σ^- components of the total field exhibit a periodic variation with the same spatial period, (ii) the maxima of I^+ are located at points where $I^- = 0$ and *vice versa*. These features of the field are to be found in the generalizations to 2D and 3D of the $\text{lin} \perp \text{lin}$ configuration.

We assume here that the field polarization lies in the xOy plane. The first step to characterize the lattice consists in the study of the intensity of the two circular components $I^+(\mathbf{r}) = |\mathbf{e}_+^* \cdot \mathbf{E}(\mathbf{r})|^2$ and $I^-(\mathbf{r}) = |\mathbf{e}_-^* \cdot \mathbf{E}(\mathbf{r})|^2$ of the field $\mathbf{E}(\mathbf{r}, t) = \text{Re}[\mathbf{E}(\mathbf{r})e^{-i\omega t}]$. For example, if the field results from the superposition of several plane waves of real amplitudes E_j , wavevectors \mathbf{k}_j , polarizations $\boldsymbol{\varepsilon}_j$ and phases ϕ_j , we find

$$I^+(\mathbf{r}) = \sum_{j,l} E_j E_l (\mathbf{e}_+^* \cdot \boldsymbol{\varepsilon}_j)(\mathbf{e}_+ \cdot \boldsymbol{\varepsilon}_l^*) \exp i[(\mathbf{k}_j - \mathbf{k}_l) \cdot \mathbf{r} + \phi_j - \phi_l] \quad (68)$$

and a similar expression for $I^-(\mathbf{r})$ obtained by changing \mathbf{e}_+ into \mathbf{e}_- . The bipotential for the $J_g = 1/2 \rightarrow J_e = 3/2$ transition is then readily obtained using Eqs. (43).

The results presented in Section 2 can be applied to determine the lattice structure. For example, Eq. (68) shows that the vectors $(\mathbf{k}_j - \mathbf{k}_l)$ belong to the reciprocal lattice. We can take $\mathbf{a}_1^* = \mathbf{k}_1 - \mathbf{k}_2$, $\mathbf{a}_2^* = \mathbf{k}_1 - \mathbf{k}_3$, etc. as primitive translations of the reciprocal lattice and find the primitive translations in real space using Eqs. (19) and (20) or (29). The discussion about periodic phase-independent and phase-dependent lattices, superlattices, quasiperiodic lattices presented in Section 2 can be simply adapted here. In particular, a periodic phase-independent lattice is obtained in 2D with three beams and in 3D with four beams [13]. Note that for a $\text{lin} \perp \text{lin}$ configuration, the primitive cell should at least contain one σ^+ well and one σ^- well.

Usually, the graphic description of potentials in the case of a $J_g = 1/2 \rightarrow J_e = 3/2$ transition consists of the map of $U_{\text{inf}} = \inf\{U_+, U_-\}$ together with the points of circular polarizations. Similarly, for transitions $J_g = J \rightarrow J_e = J + 1$ with $J \geq 1$ integer, the map of the lowest potential surface together with the points of circular polarization is usually presented. When it is important to have a scheme involving several potential surfaces, sections of the surfaces are generally shown.

Comments: (i) In the jumping regime the reactive and dissipative forces are given by the following expressions which generalize Eqs. (8) and (9):

$$\mathbf{F}' = -\hbar \Delta'_0 \sum_{l \neq j} \frac{E_l E_j}{E_0^2} i(\mathbf{k}_l - \mathbf{k}_j) \text{Tr}\{(\hat{\mathbf{d}}^- \cdot \boldsymbol{\varepsilon}_j^*)(\hat{\mathbf{d}}^+ \cdot \boldsymbol{\varepsilon}_l) \sigma\} \\ \times \exp i[(\mathbf{k}_l - \mathbf{k}_j) \cdot \mathbf{R} + \phi_l - \phi_j], \quad (69)$$

$$\mathbf{F}'' = \hbar \Gamma'_0 \sum_l \frac{E_l^2}{E_0^2} \mathbf{k}_l \text{Tr}\{(\hat{\mathbf{d}}^- \cdot \boldsymbol{\varepsilon}_l^*) - (\hat{\mathbf{d}}^+ \cdot \boldsymbol{\varepsilon}_l) \sigma\} \\ + \frac{\hbar \Gamma'_0}{2} \sum_{l \neq j} \frac{E_l E_j}{E_0^2} (\mathbf{k}_l + \mathbf{k}_j) \text{Tr}\{(\hat{\mathbf{d}}^- \cdot \boldsymbol{\varepsilon}_j^*)(\hat{\mathbf{d}}^+ \cdot \boldsymbol{\varepsilon}_l^*) \sigma\} \\ \times \exp i[(\mathbf{k}_l - \mathbf{k}_j) \cdot \mathbf{R} + \phi_l - \phi_j], \quad (70)$$

where σ is the restriction of the density matrix to the ground state (see Section 4.1). A rapid inspection shows that \mathbf{F}' is equal to $-\text{Tr}\{\sigma \nabla \hat{U}\}$ where \hat{U} is the light-shift Hamiltonian defined in Eq. (45). This equation reminds of Eq. (5); however, contrary to the classical situation, in the multidimensional case \mathbf{F}' is not necessarily the gradient of a potential. It should also be noticed that \mathbf{F}' generally differs from $-\sum_n \Pi_n \nabla U_n$ (where Π_n is the population of the state $|\Phi_n\rangle$) because of nonadiabatic terms [16]. The equality occurs when the $|\Phi_n\rangle$ are space independent (Eq. (60) was derived in this situation).

(ii) If the optical potential is spatially periodic, the topological potentials are also spatially periodic. Consider the situation where $\mathbf{a}_1, \mathbf{a}_2, \mathbf{a}_3$ are three independent primitive translations of the potential. The basis vectors $\mathbf{a}_1^*, \mathbf{a}_2^*, \mathbf{a}_3^*$ in the reciprocal space are related to $\mathbf{a}_1, \mathbf{a}_2, \mathbf{a}_3$ through Eqs. (29). Because of the periodicity, the eigenstates $|\Phi_n\rangle$ of $\hat{U}(\mathbf{R})$ have a Fourier expansion

$$|\Phi_n\rangle = \sum_n \sum_{p_j \in \mathbb{Z}} C_{p_j}^{nm} \exp i \left[\sum_{i=1,2,3} p_j \mathbf{a}_j^* \cdot \mathbf{R} \right] |m\rangle. \quad (71)$$

All quantities $\langle \Phi_{n'} | \nabla \Phi_n \rangle$ which are the building blocks of $\langle n | \mathbf{A}_t | n \rangle = i\hbar \langle \nabla \Phi_n | \Phi_n \rangle$ and $\langle n | U_t | n \rangle = (\hbar^2/2M) \sum_{n' \neq n} |\langle \Phi_{n'} | \nabla \Phi_n \rangle|^2$ (see Eqs. (54) and (55)) are thus periodic functions with primitive translations $\mathbf{a}_1, \mathbf{a}_2, \mathbf{a}_3$.

3.3.2. Three-beam two-dimensional configurations

The topography of the potential surfaces is invariant under phase translations in a three-beam configuration for reasons identical to those presented in Section 2.

We start by the description of the configuration used by Grynberg et al. [13]. Three coplanar beams of equal amplitudes E_0 , making with each other an angle of 120° (Fig. 17a) and linearly polarized in the xOy plane of the beams, create a total field with a space dependent polarization.

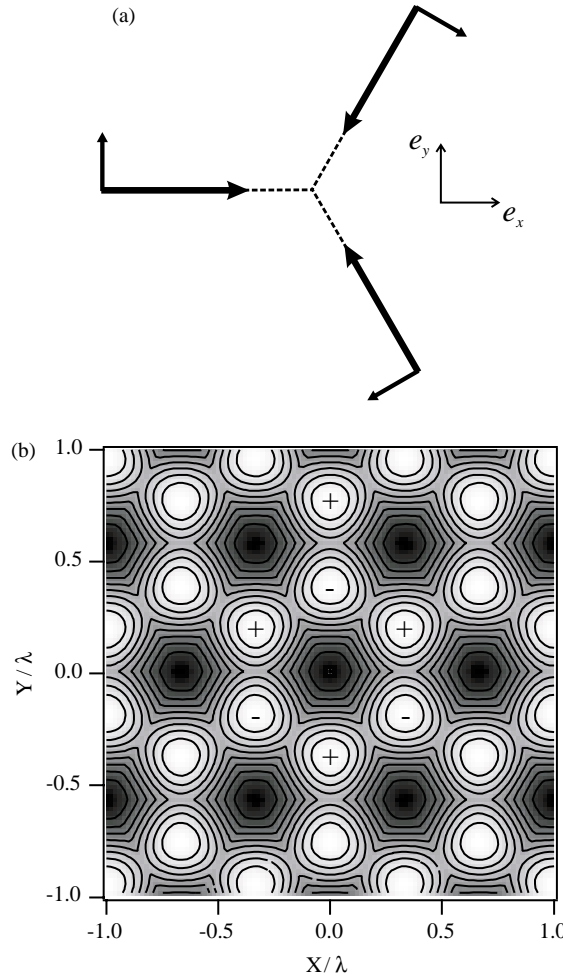


Fig. 17. (a) Beam configuration. The three coplanar beams make an angle of 120° with each other. Their linear polarizations lie in the plane of the figure. (b) Map of the lowest potential surface. The potential minima, corresponding to bright zones, are found in points where the light is circularly polarized, alternatively σ^+ and σ^- .

Indeed, with an appropriate choice of phase, the total field is given by Eq. (37) with

$$E^-(\mathbf{r}) = \frac{E_0}{\sqrt{2}} (\exp i\mathbf{k}_1 \cdot \mathbf{r} + j \exp i\mathbf{k}_2 \cdot \mathbf{r} + j^2 \exp i\mathbf{k}_3 \cdot \mathbf{r}),$$

$$E^+(\mathbf{r}) = -\frac{E_0}{\sqrt{2}} (\exp i\mathbf{k}_1 \cdot \mathbf{r} + j^2 \exp i\mathbf{k}_2 \cdot \mathbf{r} + j \exp i\mathbf{k}_3 \cdot \mathbf{r}), \quad (72)$$

where $j = \exp 2i\pi/3$. The translation symmetries of $I^-(\mathbf{r})$ and $I^+(\mathbf{r})$ are those of a hexagonal lattice. Indeed, from the knowledge of the primitive vectors $\mathbf{a}_1^* = \mathbf{k}_1 - \mathbf{k}_2$ and $\mathbf{a}_2^* = \mathbf{k}_1 - \mathbf{k}_3$ of the reciprocal lattice, we deduce from Eqs. (19) and (20) that $\mathbf{a}_1 = (4\pi/3k^2)\mathbf{k}_2$ and $\mathbf{a}_2 = -(4\pi/3k^2)\mathbf{k}_3$ are primitive translations for $I^-(\mathbf{r})$ and $I^+(\mathbf{r})$. They are also primitive translations of the optical potential (Fig. 17b) which is given by Eqs. (43) in the case of a $J_g = 1/2 \rightarrow J_e = 3/2$ transition.

It should be noticed that the maxima of I^+ are found at points where $I^- = 0$ and vice versa. More precisely, inside the unit cell a pure σ^+ site is found in $\mathbf{r} = (2\mathbf{a}_1 + \mathbf{a}_2)/3$, a pure σ^- site in $\mathbf{r} = (\mathbf{a}_1 + 2\mathbf{a}_2)/3$ and the field vanishes in $\mathbf{r} = \mathbf{0}$. The alternation of σ^+ and σ^- sites permits a Sisyphus cooling mechanism identical to the one described in Section 3.1.2 to occur.

Comments: (i) The lattices exhibiting alternated σ^+ and σ^- potential wells are often described as *antiferromagnetic*. This is because in steady state the atoms are optically pumped into the states $|m = J_g\rangle$ and $|m = -J_g\rangle$, respectively. The resulting pattern of atoms has thus the same order as an antiferromagnetic medium. However, in the case of an optical lattice, the order results from optical pumping and not from atom–atom interactions.

(ii) Another possible 2D three-beam configuration that gives rise to a potential with alternated σ^+ and σ^- wells is obtained with beams having wavevectors given by Eq. (16). The beam propagating along the x -axis has an amplitude E_0 and a polarization \mathbf{e}_y , while the two other beams have an amplitude $E_0/2$ and a polarization \mathbf{e}_z . The lattice is generally centred rectangular with a basis consisting of a σ^+ and a σ^- well [14].

3.3.3. Four-beam two-dimensional configurations

A 2D $\text{lin} \perp \text{lin}$ lattice can also be generated with a y -polarized standing wave along Ox and x -polarized standing wave along Oy [25]. With an appropriate choice of phases (i.e. of the origin of the space coordinates) the circular components of the field are

$$\begin{aligned} E^-(\mathbf{r}) &= \sqrt{2}E_0[\text{ie}^{i\phi}\cos kx + \cos ky], \\ E^+(\mathbf{r}) &= \sqrt{2}E_0[\text{ie}^{i\phi}\cos kx - \cos ky], \end{aligned} \quad (73)$$

where ϕ is the phase difference between the two standing waves. (If we consider the standing wave as the sum of two counter-propagating travelling waves as in Section 2.3.3, $2\phi = \phi_1 + \phi_3 - \phi_2 - \phi_4$.) The optical potentials given by Eq. (43) in the case of a $J_g = 1/2 \rightarrow J_e = 3/2$ transition are thus phase-dependent as expected for a 2D configuration with more than three beams. It can be easily checked that a pattern with alternated σ^+ and σ^- wells is obtained for $\phi = \pm \pi/2$. The potential has the symmetry of a square lattice with a basis consisting of one σ^+ and one σ^- potential wells (Fig. 18). In practice, to achieve this type of pattern it is necessary to lock the relative phase ϕ of the beams.

3.3.4. The four-beam three-dimensional configuration

The four-beam 3D $\text{lin} \perp \text{lin}$ configuration is a simple extension of the 1D $\text{lin} \perp \text{lin}$ configuration studied earlier. The beam wavevectors are arranged according to Eq. (30) and Fig. 7, the polarizations being \mathbf{e}_y for the two beams propagating in the xOz plane and \mathbf{e}_x for the two beams propagating in the yOz plane [14,42]. The beams have equal amplitude E_0 . The circular components of the field are

$$\begin{aligned} E^-(\mathbf{r}) &= \sqrt{2}E_0 \exp iK_-z [\cos(K_x x) \text{e}^{iK_+z} + \cos(K_y y) \text{e}^{-iK_+z}], \\ E^+(\mathbf{r}) &= \sqrt{2}E_0 \exp iK_-z [\cos(K_x x) \text{e}^{iK_+z} - \cos(K_y y) \text{e}^{-iK_+z}], \end{aligned} \quad (74)$$

where $K_x = k \sin \theta_x$, $K_y = k \sin \theta_y$ and $K_{\pm} = k(\cos \theta_x \pm \cos \theta_y)/2$. The relationship to the 1D $\text{lin} \perp \text{lin}$ configuration is obvious when the 3D field is viewed along a line parallel to Oz

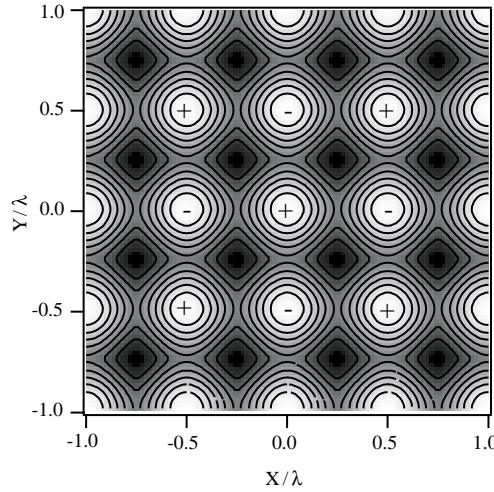


Fig. 18. Map of the lowest potential surface in the case of two coplanar standing waves with a linear polarization in the xOy plane and for a phase difference $\phi = \pi/2$.

such as $x = y = 0$. Apart from the distance between two consecutive circular sites which is $\lambda_+/4$ (with $\lambda_+ = 2\pi/K_+$) instead of $\lambda/4$, one finds the same field configuration. More generally, the 3D lattice exhibits alternated σ^+ and σ^- wells, the spatial periodicity being given by the primitive translation vectors derived in Eq. (31). Maps of the potential in the xOy and xOz planes are shown in Fig. 19.

It can be noticed that a potential well is generally not isotropic. Therefore the atomic vibrational frequencies along the three principal axes are generally different (see Eqs. (102) in Section 5.3).

Comments: (i) The data for these lattices are sometimes given as a function of the light-shift per beam Δ'_0 and sometimes as a function of the light-shift Δ' at a point of circular polarization for a transition having a Clebsch–Gordan coefficient equal to 1. The relation between these quantities is $\Delta' = 8\Delta'_0$.

(ii) From the knowledge of the intensity per beam I and the detuning Δ , one deduces $\Delta' = (I/I_{\text{sat}})(\Gamma^2/\Delta)$ where I_{sat} is the saturation intensity. Because I_{sat} and Γ are generally well known parameters, this formula is often used in practice.

(iii) Another simple 3D generalization of the 1D $\text{lin} \perp \text{lin}$ situation is obtained by inserting a 2D periodic mask on the trajectory of one of the beams of the 1D $\text{lin} \perp \text{lin}$ configuration. Because of the Talbot effect [43–45], a periodic 3D configuration is achieved with alternated σ^+ and σ^- sites (Section 2.5.3).

3.4. Bright lattices and grey molasses

3.4.1. Photon scattering rate

In the case of a $J_g = J \rightarrow J_e = J + 1$ transition with $J_g \geq 1/2$, the majority of atoms are optically pumped into σ^+ and σ^- wells where they are trapped. Once in a well, they scatter photons

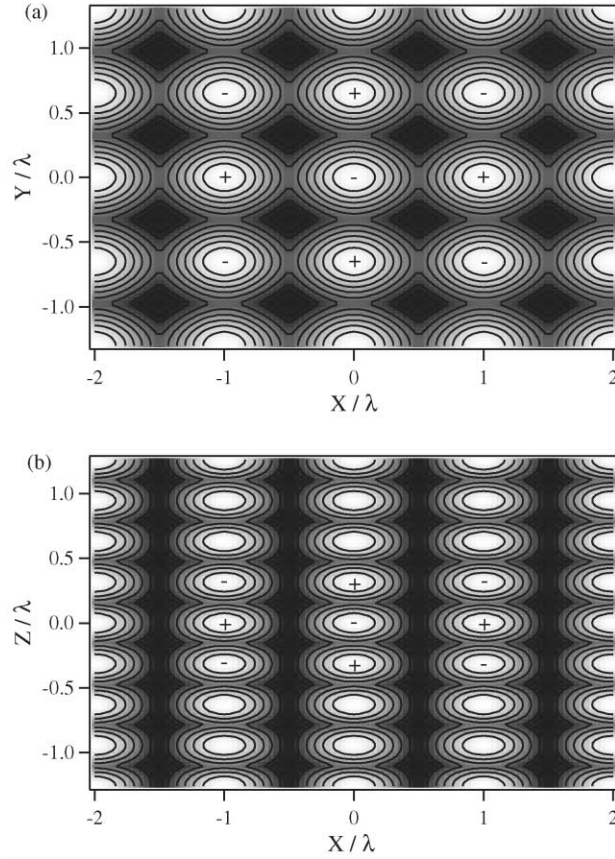


Fig. 19. Section of the lowest potential surface along the xOy (a) and xOz (b) planes for the 3D four-beam $\text{lin} \perp \text{lin}$ configuration. The maps correspond to $\theta_x = 30^\circ$ and $\theta_y = 50^\circ$. The spatial periods along Ox , Oy and Oz are λ_x , λ_y and $\lambda_+/2$, respectively.

at the maximum rate because the Clebsch–Gordan coefficient connecting $m_g = J$ to $m_e = J + 1$ is equal to 1. The photon scattering from these lattices is high, hence the name *bright lattice* often given to them.

By contrast, in the case of $J_g = J \rightarrow J_e = J$ (with J integer) and $J_g = J \rightarrow J_e = J - 1$ transitions, atoms are optically pumped into internal dark states which radiate very few photons. Only motional coupling induces absorption from the internal dark states. This is why they are called *grey molasses* or *grey lattices*. Molasses here refers to the fact that the majority of atoms are in a flat potential surface because the light-shift of an internal dark state is equal to 0. Hence no localization is expected. In fact, this is not exactly true. First, the topological potential (Section 3.1.4) generally differs from 0 so that the potential surface associated with an internal dark state is not perfectly flat [84]. Second, the other potential surfaces are spatially modulated (and this is indeed necessary for the Sisyphus effect to occur, see Fig. 14). Therefore the atomic population may be modulated and the term grey lattice can also be used for these systems.

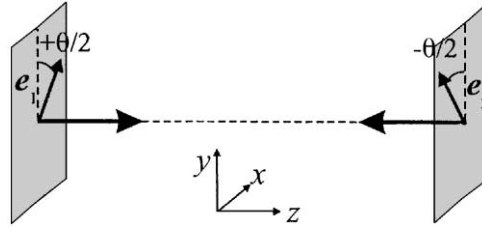


Fig. 20. The lin θ lin configuration consists of two counter-propagating beams with linear polarizations making an angle θ with each other.

Dark lattices are a special case where an eigenstate of kinetic energy can be found from the internal dark state. Because very low temperatures can be achieved in this case using VSCPT [60], the topological potentials are particularly significant in this situation [53].

Comment: The addition of a small magnetic field to a grey molasses leads to a potential which is spatially modulated even for the internal dark state [85]. In 2D and 3D, this potential consists of antidots rather than wells in most configurations (see Section 9.2).

3.4.2. Blue Sisyphus cooling—a one-dimensional model

The lin θ lin configuration consists of two linearly polarized beams counterpropagating along Oz , the angle between the polarizations being θ (Fig. 20). To fix the notations we take $\mathbf{e}_1 = \cos \theta/2 \mathbf{e}_y + \sin \theta/2 \mathbf{e}_x$ and $\mathbf{e}_2 = \cos \theta/2 \mathbf{e}_y - \sin \theta/2 \mathbf{e}_x$ as the polarization vectors. If the beams have equal amplitude E_0 , the circular components are

$$E^\pm(z) = E_0 \sqrt{2} \cos\left(kz \pm \frac{\theta}{2}\right). \quad (75)$$

Although there exists sites of pure circular polarization, they generally do not coincide with the minima of the potentials as it can be checked in the case of the $J_g = 1/2 \rightarrow J_e = 3/2$ transition using Eqs. (43) and (75). This field configuration is in fact well suited to understand the Sisyphus cooling of grey and dark molasses. For the sake of simplicity, we consider the $J_g = 1 \rightarrow J_e = 1$ transition. It can be noticed that for a field with only σ^+ and σ^- components, the population of the $|J_g, m_g = 0\rangle$ sublevel vanishes in steady state because there is no fluorescence from $|J_e, m_e = 0\rangle$ towards $|J_g, m_g = 0\rangle$ (the Clebsch–Gordan coefficient is 0). We can thus describe the cooling process within the subspace of the Zeeman components $|+1\rangle$ and $|-1\rangle$ of the ground state. The eigenstates of the light-shift operator are

$$\begin{aligned} |\Phi_{\text{NC}}\rangle &= \frac{1}{\sqrt{D(z)}} \left[\cos\left(kz + \frac{\theta}{2}\right) |+1\rangle + \cos\left(kz - \frac{\theta}{2}\right) |-1\rangle \right], \\ |\Phi_{\text{C}}\rangle &= \frac{1}{\sqrt{D(z)}} \left[\cos\left(kz - \frac{\theta}{2}\right) |+1\rangle - \cos\left(kz + \frac{\theta}{2}\right) |-1\rangle \right], \end{aligned} \quad (76)$$

where $D(z) = 1 + \cos \theta \cos 2kz$. The corresponding adiabatic energies are

$$\begin{aligned} U_{\text{NC}} &= 0, \\ U_{\text{C}} &= \hbar \Delta'_0 D(z). \end{aligned} \quad (77)$$

Because $U_{\text{NC}} = 0$, $|\Phi_{\text{NC}}\rangle$ is the internal dark state. The motional coupling between $|\Phi_{\text{NC}}\rangle$ and $|\Phi_{\text{C}}\rangle$ is equal to

$$W_{\text{MC}} = -i\hbar \langle \Phi_{\text{C}} | \left(\frac{d}{dt} | \Phi_{\text{NC}} \rangle \right) . \quad (78)$$

For an atom moving at velocity v we have, using $t = Z/v$ and Eqs. (76)

$$W_{\text{MC}} = -i\hbar \frac{kv \sin \theta}{D(Z)} . \quad (79)$$

Because $D(Z)$ is minimum near the anticrossings between U_{NC} and U_{C} , the transition probability from $|\Phi_{\text{NC}}\rangle$ to $|\Phi_{\text{C}}\rangle$ is maximum in these points (see Fig. 14). In the case of a blue detuning ($\Delta'_0 > 0$), an atom transferred into $|\Phi_{\text{C}}\rangle$ then climbs a potential hill. Because the photon absorption rate $\Gamma'_\text{C} = \Gamma'_0 D(Z)$ is maximum at the top of the potential hill, the probability to return into $|\Phi_{\text{NC}}\rangle$ is maximum near these points and on the average, the kinetic energy of the atom decreases.

Comments: (i) Because of motional coupling, the atoms in $|\Phi_{\text{NC}}\rangle$ have a finite lifetime $\Gamma_{\text{NC}}'^{-1}$ given by

$$\Gamma_{\text{NC}}' = \Gamma_{\text{C}}' \frac{|W_{\text{NC}}|^2}{U_{\text{C}}^2 + (\hbar^2 \Gamma_{\text{C}}'^2 / 4)} . \quad (80)$$

This formula can be used to calculate the friction force. For example, in the range $\Gamma'_0 \ll kv \ll \Delta'_0$, the kinetic energy loss per unit time is on the order of $\overline{\Gamma_{\text{NC}}'} \hbar \Delta'_0$, which leads to a friction coefficient on the order of $-\hbar k^2 (\Gamma / \Delta)$. This friction is weaker than the one found in the case of a bright lattice (Eq. (59)) by a factor $(\Gamma / \Delta)^2$. However the momentum diffusion is also reduced and the temperature is still predicted to be on the order of $\hbar \Delta'_0$ [86].

(ii) The topological potentials can be calculated for the eigenstates of Eq. (76) using Eqs. (54) and (55). In particular, for the internal dark state $|\Phi_{\text{NC}}\rangle$, one finds $\mathbf{A}_t = \mathbf{0}$ and

$$U_t = E_{\text{R}} \frac{\sin^2 \theta}{[1 + \cos \theta \cos 2kZ]^2} . \quad (81)$$

As expected the order of magnitude of U_t is the recoil energy. The maxima U_t are found for $2kZ = (2p + 1)\pi$ (p integer), which corresponds to the minima of the field intensity.

3.5. Universality of Sisyphus cooling

Sisyphus cooling is a very general cooling process which can be accomplished in many field configurations. Although the basic ideas were already given in the case of the $\text{lin} \perp \text{lin}$ model system (existence of several potential surfaces, of a dissipation process transferring the atoms to the lowest potential surface, nonadiabaticity), it is however interesting to describe a few other configurations either because they are often used or because they exhibit particular characteristics.

3.5.1. Six-beam molasses

In many experiments, cooling is achieved using a molasses consisting of two counter-propagating beams along each of the three axis [9]. For most situations (i.e. choices of

polarization and transition), the optical potentials are spatially modulated. Because of the combined effects of different light-shifts and optical pumping rates, Sisyphus cooling occurs for a red detuning in the $J_g = J \rightarrow J_e = J + 1$ case and for a blue detuning in the $J_g = J \rightarrow J_e = J$ and $J_g = J \rightarrow J_e = J - 1$ situations.

Because of its translational symmetries (see Section 2.5.2), this structure can be described as a lattice. However, in most experiments the phases of the beams vary randomly. Hence the topography of potentials, the field polarization and the optical pumping rates are not fixed and the experimental results generally correspond to an average over the phases. In that sense, the term molasses is appropriate because the relevant properties do not depend on the precise shape of the potentials.

Comments: (i) Although this field configuration does not generally yield alternated σ^+ and σ^- sites, a very efficient Sisyphus cooling is however obtained [87].

(ii) The properties of a magneto-optical trap were studied experimentally by Schadowinkel et al. [88] for several values of the relative phases between the six incident beams. It appears that in most cases, the magneto-optical trap behaves as an optical lattice. In particular, there are potential wells in which the atoms are localized.

3.5.2. Potential wells: from circular to linear polarization

The 3D Rot [$\text{lin} \perp \text{lin}$] four-beam configuration described in this paragraph is interesting because different patterns of potential, leading to different cooling schemes, are obtained according to the angles between the beams and the choice of polarizations. In this configuration, the deepest potential wells can have a linear π polarization. Therefore the optical pumping rates near the bottom of the wells are not reduced by a Lamb–Dicke factor as in Eq. (66) and the parameter range in which a jumping regime is found is much broader than in the $\text{lin} \perp \text{lin}$ case [89].

This field configuration is obtained from the 3D four-beam $\text{lin} \perp \text{lin}$ configuration (Section 3.3.4) by rotating all the polarizations by 90° . The beam wavevectors are thus still given by Eq. (30) but the polarizations of the two beams propagating in the xOz plane lie in the xOz plane and similarly the beams propagating in the yOz plane have their polarizations in this yOz plane. The main difference with the $\text{lin} \perp \text{lin}$ case is that the field now has a π component. In the case where $\theta_x = \theta_y = \theta$, the components of the field are

$$\begin{aligned} E^\pm(\mathbf{r}) &= \sqrt{2}E_0 \cos \theta [\pm i \sin(K_\perp x) \exp iK_+ z - \sin(K_\perp y) \exp -iK_+ z], \\ E^\pi(\mathbf{r}) &= 2E_0 \sin \theta [\cos(K_\perp x) \exp iK_+ z + \cos(K_\perp y) \exp -iK_+ z], \end{aligned} \quad (82)$$

with $K_\perp = k \sin \theta$ and $K_+ = k \cos \theta$. In the case of a small angle θ , the π component remains small and the potentials have a pattern similar to those of the $\text{lin} \perp \text{lin}$ configuration with alternated σ^+ and σ^- wells. By contrast, when $\theta \geq 45^\circ$, these wells are no longer attractive in the three dimensions and the atomic localization occurs near π -polarized sites [14]. Contrary to the case of σ^+ and σ^- sites where all the atoms are optically pumped in a single sublevel ($m = J$ or $-J$), the atoms are distributed over several sublevels in a site where the polarization is linear. The population increases when $|m|$ decreases but a significant fraction of the population is found outside the lowest potential surface. For example, in the case of the $J_g = 1 \rightarrow J_e = 2$ transition, the fraction of atoms in $m = 0$ is $9/17$.

Comments: (i) A local cooling mechanism similar to the one shown in Fig. 13 is certainly important in this configuration.

(ii) Eq. (82) for the field is relative to the (fixed) z axis. It should however be noticed that in any point \mathbf{r} , the field actually oscillates in a plane and an expansion in terms of two local circular polarizations is also possible.

This is because the field can always be written as

$$\mathbf{E}(\mathbf{r}, t) = \text{Re}[(\mathbf{E}_P(\mathbf{r}) + i\mathbf{E}_Q(\mathbf{r}))e^{-i\omega t}], \quad (83)$$

where $\mathbf{E}_P(\mathbf{r})$ and $\mathbf{E}_Q(\mathbf{r})$ are real vectors. In \mathbf{r} , the field oscillates in the plane generated by $\mathbf{E}_P(\mathbf{r})$ and $\mathbf{E}_Q(\mathbf{r})$.

3.5.3. Magnetically assisted Sisyphus effect

In the Sisyphus cooling of transitions with an internal dark state (Sections 3.1.5 and 3.4.2), the atoms are optically pumped towards the lowest potential curve while motional coupling transfers the atoms into the other potential curves, allowing the Sisyphus process to occur. Similar effects are found in magnetically assisted Sisyphus effect (MASE, also known as MILC for magnetically induced laser cooling) [90]. However this scheme also works with $J_g = J \rightarrow J_e = J + 1$ transitions and red detuned beams.

Consider for example a 1D σ^+ polarized standing wave and a $J_g = 1/2 \rightarrow J_e = 3/2$ transition. The atoms are optically pumped in the $m_g = +1/2$ sublevel which has the largest light-shift (see Fig. 11). However, at the nodes of the standing wave the $|+1/2\rangle$ and $|-1/2\rangle$ substates have the same energy so that a small *transverse* magnetic field can mix the two states efficiently. The adiabatic eigenstates are then space dependent and the transfer from the lowest potential curve to the higher one due to motional coupling can be significant near the nodes of the field. The Sisyphus effect proceeds as follows: the atoms climb a potential hill of the lower potential curve, undergo a motional-induced transition near the nodes of the field, fall down in a shallower potential well of the higher potential curve before being optically pumped into the lower potential curve by the σ^+ light near an antinode of the field. On the average, the kinetic energy has decreased.

Comments: (i) In steady state most atoms are trapped in a well associated with an eigenstate which is nearly $|+1/2\rangle$ near the bottom of the well. Because the magnetic moments of all the trapped atoms are nearly parallel, this type of lattice is often called *ferromagnetic*.

(ii) Ferromagnetic optical lattices do not necessarily require an external static field. An example of 3D four-beam lattice where the atoms are trapped in σ^+ sites only was reported by Grynberg et al. [13].

4. Theoretical methods

In this section, we describe several methods used to study theoretically the dynamics of an atom with a degenerate ground state in an electro-magnetic field resulting from the interference of several waves of same frequency $\omega/2\pi$.

In the first paragraph, we present the basic approximations leading to the master equation (Eq. (92)) for the ground state density matrix. The two following paragraphs are devoted to two methods often used to solve this optical pumping equation. The first one, the band method,

consists of a quantum treatment of all atomic degrees of freedom while the second one considers the atomic centre-of-mass motion classically. We finally present an alternative approach to the resolution of the master equation: the Monte-Carlo wavefunction approach.

4.1. Generalized optical Bloch equations

Let us consider atoms having a closed transition of frequency ω_0 between a fundamental state g with an angular momentum J_g and an excited state e with an angular momentum J_e . The external degrees of freedom of the atom are quantized, so that the position and momentum operators \mathbf{R} and \mathbf{P} do not commute. The atoms evolve in the presence of a laser field of frequency $\omega = \omega_0 + \Delta$. The interaction between the atom and the laser field is treated classically using the electric dipole Hamiltonian in the rotating wave approximation:

$$\hat{V}_{\text{AL}}(t) = \hat{V}_{\text{AL}}^+(t) + \hat{V}_{\text{AL}}^-(t) = -\mathbf{d}^+ \cdot \mathbf{E}^{(+)}(\mathbf{R}, t) - \mathbf{d}^- \cdot \mathbf{E}^{(-)}(\mathbf{R}, t). \quad (84)$$

In this equation, $\mathbf{E}^{(+)}$ (*resp.* $\mathbf{E}^{(-)}$) represents the positive (*resp.* negative) frequency component of the complex laser field and \mathbf{d}^+ (*resp.* \mathbf{d}^-) the upwards (*resp.* downwards) component of the atomic dipole. One can also write the atomic dipole \mathbf{d} as

$$\mathbf{d} = \mathcal{D}(\hat{\mathbf{d}}^+ + \hat{\mathbf{d}}^-), \quad (85)$$

where the reduced matrix element of the dipole \mathcal{D} and the reduced atomic dipole $\hat{\mathbf{d}}^+$ are defined through the Wigner–Eckart theorem:

$$\mathcal{D} = \frac{\langle J_e || \mathbf{d}^+ || J_g \rangle}{\sqrt{2J_e + 1}}, \quad (86)$$

$$\langle J_e, m_e | \hat{\mathbf{d}}^+ \cdot \mathbf{e}_q | J_g, m_g \rangle = \langle J_e, m_e | J_g, 1, m_g, q \rangle \quad \text{with } q = 0, \pm 1. \quad (87)$$

The vacuum electro-magnetic field is quantized and is considered as a reservoir inducing fluctuations, hence dissipation, in the evolution of the atomic system. In particular, spontaneous emission originates from the atom–vacuum interaction.

The equations describing the interaction between atoms and light are called *generalized optical Bloch equations* [10], and they determine the evolution of the density matrix ρ . This density matrix can be written as

$$\rho = \begin{pmatrix} \rho_{ee} & \rho_{eg} \\ \rho_{ge} & \rho_{gg} \end{pmatrix}, \quad (88)$$

where ρ_{gg} and ρ_{ee} are the matrices containing the populations and the Zeeman coherences of the fundamental and excited states, respectively, and $\rho_{ge} = \rho_{eg}^\dagger$ contains the optical coherences.

Using a unitary transformation ($\rho_{gg} \rightarrow \rho_{gg}$, $\rho_{ee} \rightarrow \rho_{ee}$ and $\rho_{eg} \rightarrow \rho_{eg} e^{i\omega t}$) which is equivalent to using a frame rotating at frequency ω , one can obtain a time-independent expression for the optical Bloch equations:

$$\frac{d\rho_{ee}}{dt} = \frac{1}{i\hbar} \left[\frac{\mathbf{P}^2}{2M}, \rho_{ee} \right] + \frac{1}{i\hbar} [\hat{V}_{\text{AL}}^{(+)} \rho_{ge} - \rho_{eg} \hat{V}_{\text{AL}}^{(-)}] - \Gamma \rho_{ee}, \quad (89)$$

$$\frac{d\rho_{eg}}{dt} = \frac{1}{i\hbar} \left[\frac{\mathbf{P}^2}{2M}, \rho_{eg} \right] + \frac{1}{i\hbar} [\hat{V}_{\text{AL}}^{(+)} \rho_{gg} - \rho_{ee} \hat{V}_{\text{AL}}^{(+)}] + \left(i\Delta - \frac{\Gamma}{2} \right) \rho_{eg}, \quad (90)$$

$$\begin{aligned} \frac{d\rho_{\text{gg}}}{dt} = & \frac{1}{i\hbar} \left[\frac{\mathbf{P}^2}{2M}, \rho_{\text{gg}} \right] + \frac{1}{i\hbar} [\hat{V}_{\text{AL}}^{(-)} \rho_{\text{eg}} - \rho_{\text{ge}} \hat{V}_{\text{AL}}^{(+)}] \\ & + \frac{3\Gamma}{8\pi} \int d^2\Omega_{\kappa} \sum_{\mathbf{e} \perp \kappa} (\widehat{\mathbf{d}}^- \cdot \mathbf{e}^*) e^{-i\kappa \cdot \mathbf{R}} \rho_{\text{ee}} e^{i\kappa \cdot \mathbf{R}} (\widehat{\mathbf{d}}^+ \cdot \mathbf{e}) . \end{aligned} \quad (91)$$

The last term of Eq. (91) describing the effect of spontaneous emission is integrated over the solid angle Ω_{κ} in which a spontaneous photon of wavevector κ and polarization \mathbf{e} is emitted.

Before going to the next step, it is important to note that Eqs. (89)–(91) take into account all the mechanisms concerning the evolution of atomic observables and do not contain any radical approximation on laser parameters or atomic velocities.

In most cases, however, the saturation parameter is small ($s(\mathbf{R}) = (\Omega(\mathbf{R})^2/2)/(\Delta^2 + \Gamma^2/4) \ll 1$ where $\Omega(\mathbf{R})$ is the total resonant Rabi frequency) so that the atoms spend most of their time in the ground state. Furthermore, atoms in optical lattices are generally much colder than the Doppler limit, so that their Doppler-shift kv is negligible compared to the natural width Γ . When these two conditions are fulfilled, it is possible to eliminate adiabatically the excited state and the optical coherences: Eq. (91) indicates that the evolution time of ρ_{gg} is on the order of the optical pumping rate $\tau_{\text{p}} \simeq \Gamma'^{-1}$ while ρ_{ee} and ρ_{ge} evolve much faster, with rates on the order of Γ (see Eqs. (89) and (90)). After the adiabatic elimination, one obtains an equation related only to the restriction of the density matrix ρ to the fundamental state, ρ_{gg} [16,91]. From now on, we use the simplified notation $\sigma = \rho_{\text{gg}}$. Let us remark that σ is a square matrix of dimension $2J_{\text{g}} + 1$ whose diagonal elements are the populations of the Zeeman sub-levels of the fundamental state, the off-diagonal elements corresponding to Zeeman coherences (light-induced couplings between the Zeeman sub-levels).

The master equation for the ground state density matrix σ is

$$\frac{d\sigma}{dt} = \frac{1}{i\hbar} [H_{\text{eff}}, \sigma] + \left(\frac{d\sigma}{dt} \right)_{\text{relax}} . \quad (92)$$

Eq. (92) has the same structure as the traditional optical pumping equation [18,16] even though the centre-of-mass motion is here quantized. We now analyse the different terms of Eq. (92).

- The first term corresponds to the Hamiltonian evolution due to the effective Hamiltonian $H_{\text{eff}} = \mathbf{P}^2/2M + \hat{U}(\mathbf{R})$. The light-shift operator $\hat{U}(\mathbf{R})$ may also be written as $\hat{U}(\mathbf{R}) = \hbar \Delta'(\mathbf{R}) \hat{u}(\mathbf{R})$, where $\Delta'(\mathbf{R}) = \Delta s(\mathbf{R})/2$ and $\hat{u}(\mathbf{R})$ is the dimensionless light-shift operator:

$$\hat{u}(\mathbf{R}) = [\widehat{\mathbf{d}}^- \cdot \boldsymbol{\varepsilon}^*(\mathbf{R})][\widehat{\mathbf{d}}^+ \cdot \boldsymbol{\varepsilon}(\mathbf{R})] . \quad (93)$$

Note that because the atomic position \mathbf{R} and momentum \mathbf{P} are quantized, the light-shift operator and the kinetic energy operator do not commute. Consequently, one cannot write the eigenstates of the total Hamiltonian as a product of the eigenstates of the light-shift and of the kinetic energy. The vector noted $\boldsymbol{\varepsilon}(\mathbf{R})$ represents the polarization of the laser field at point \mathbf{R} .

- The second term of Eq. (92) is a dissipative term and can be written as

$$\left(\frac{d\sigma}{dt}\right)_{\text{relax}} = -\frac{\Gamma'(\mathbf{R})}{2}\{\hat{u}(\mathbf{R}), \sigma\} + \frac{3\Gamma'(\mathbf{R})}{8\pi} \int d^2\Omega_{\mathbf{\kappa}} \sum_{\mathbf{e} \perp \mathbf{\kappa}} \hat{B}_{\mathbf{e}}^{\dagger}(\mathbf{R}) e^{-i\mathbf{\kappa} \cdot \mathbf{R}} \sigma e^{i\mathbf{\kappa} \cdot \mathbf{R}} \hat{B}_{\mathbf{e}}(\mathbf{R}), \quad (94)$$

where $\Gamma'(\mathbf{R}) = \Gamma s(\mathbf{R})/2$ and $\{A, B\} = AB + BA$. The first term on the right-hand side in Eq. (94) describes the depopulation of the fundamental state due to the absorption of photons in the laser field, while the second term corresponds to the repopulation of the fundamental state by spontaneous emission. The nonhermitian operator $\hat{B}_{\mathbf{e}}(\mathbf{R})$ is

$$\hat{B}_{\mathbf{e}}(\mathbf{R}) = [\widehat{\mathbf{d}}^{-} \cdot \boldsymbol{\varepsilon}^*(\mathbf{R})][\widehat{\mathbf{d}}^{+} \cdot \mathbf{e}]. \quad (95)$$

There is generally no analytic solution to this equation, even in simple cases. Some supplementary approximations as well as the use of numerical simulations are thus necessary.

We do not describe the technique consisting of a direct integration of the equation after discretization of the momentum space [92,93]. This method is indeed extremely power demanding and its 3D generalization cannot be implemented on usual computers.

4.2. The band method

This fully quantum method, developed in the *secular limit*, takes advantage of the strong analogy between optical lattices and periodic solid state materials. It has been used for the first time in the frame of laser-cooled atoms by Castin and Dalibard [67,92] in a one-dimensional configuration.

The basic idea is that an atom experiencing a periodic optical potential satisfies to the Bloch theorem. One can thus develop the wavefunction for the atomic position on the basis of the Bloch states, which leads to the existence of allowed and forbidden energy bands for the atoms, as for the electrons in solid-state physics.

The resolution of the master equation is made perturbatively in three steps. First, one calculates the eigenstates $|n, q, m\rangle$ ($n \geq 0$ being the band number, q the Bloch index in the first Brillouin zone and m the internal state) and the energy spectrum $E_{n,q,m}$ of the Hamiltonian H_{eff} in Eq. (92). One then takes into account the relaxation part of the master equation by calculating the rates of transfer $\gamma_{n,q,m \rightarrow n',q',m'}$ from $|n, q, m\rangle$ to $|n', q', m'\rangle$.

One finally obtains the steady-state populations $\pi(n, q, m)$ by solving the rate equations

$$0 = \dot{\pi}(n, q, m) = - \sum_{n',q',m'} \gamma_{n,q,m \rightarrow n',q',m'} \pi(n, q, m) + \sum_{n',q',m'} \gamma_{n',q',m' \rightarrow n,q,m} \pi(n', q', m'). \quad (96)$$

All steady-state quantities, such as population and momentum distributions, can then be deduced from this set of eigenstates and steady-state populations.

An inspection of the band method shows that this approach is valid if the Hamiltonian evolution dominates the dynamics, i.e. if the Bohr frequencies of the Hamiltonian are much larger than the damping rate Γ' . In this case, one can neglect the nondiagonal elements of the density matrix $\langle n, q, m | \sigma | n', q', m' \rangle$ with $(n, q, m) \neq (n', q', m')$. This approximation is called

the *secular approximation* [10] and is generally valid for large detunings. More precisely, in one-dimensional situations the energy splitting between two states is on the order of the oscillation frequency $\Omega_v \propto \sqrt{U_0 E_R}$ of the atoms in a potential well, which leads to the condition $\sqrt{U_0/E_R} \ll \Delta/\Gamma$. The increase of the band degeneracy in higher dimensions makes the extension of the band method to two and three dimensions problematic: in 2D situations, for example, the average energy splitting between two bound states is on the order of the recoil energy E_R , leading to a condition $U_0/E_R \ll |\Delta/\Gamma|$ [93]. The condition becomes even more restrictive in 3D.

On the contrary, the secular approach can be applied to transitions with angular momenta higher than 1/2 without any particular difficulty. It has been often used, in particular to predict pump–probe spectra [72,83] and to study the temperature and the magnetism of atoms in optical lattices [69,94,95], and led to results in good agreement with the experiments.

4.3. Semi-classical Monte-Carlo simulation

Here, the solution of the master equation for the ground state density matrix is evaluated by calculating the temporal evolution of a given number of atoms.

In the semi-classical approach, only the internal degrees of freedom of the atom are treated using quantum mechanics, the external degrees of freedom being treated semi-classically. The validity of this approximation requires that spatial coherence length of the wavefunction associated with the atom position to be small compared to the optical wavelength λ , which, through the Heisenberg inequality, implies the $\Delta P \gg \hbar k$. This condition means that the momentum change due to the absorption or the emission of a photon has to be small compared to the momentum distribution width.

In this regime, it is convenient to use the Wigner representation, which is particularly well adapted to the semi-classical approximation

$$W(\mathbf{R}, \mathbf{P}, t) = \left(\frac{1}{2\pi\hbar} \right)^3 \int d^3\mathbf{u} \left\langle \mathbf{R} + \frac{\mathbf{u}}{2} \right| \sigma(t) \left| \mathbf{R} - \frac{\mathbf{u}}{2} \right\rangle \exp - \frac{i\mathbf{P} \cdot \mathbf{u}}{\hbar}. \quad (97)$$

$W(\mathbf{R}, \mathbf{P}, t)$ is thus a matrix representing a quasiprobability distribution in phase space. Applying the Wigner transformation to the master equation, one obtains an equation for the evolution of the Wigner transform $W(\mathbf{R}, \mathbf{P}, t)$ of σ . This equation is nonlocal in momentum \mathbf{P} , but in the regime where a semi-classical approximation is justified, one can expand the equation up to second order in the small parameter $\hbar k/\Delta P$.

One more approximation is necessary to get Fokker–Planck-like equations for the quasipopulations $\Pi_i(\mathbf{R}, \mathbf{P}, t) = \langle \Phi_i | W(\mathbf{R}, \mathbf{P}, t) | \Phi_i \rangle$ of the eigenstates $|\Phi_i\rangle$ of the light-shift operator: the adiabatic approximation, meaning that one neglects the motion-induced couplings between two adiabatic states $|\Phi_i\rangle$ and $|\Phi_j\rangle$. This approximation amounts to neglect nondiagonal elements in the Wigner distribution in the adiabatic basis, provided one adds to the potential topological terms (see Section 3.1.4) [52].

In this model, the atom is thus submitted to an optical potential, to radiation pressure forces and to optical pumping that can induce jumps between different sublevels. In addition, a momentum diffusion coefficient takes into account the recoil of the atom during elementary absorption

or emission processes. This momentum diffusion coefficient is simulated in the calculations by random forces with a zero average.

The semi-classical Monte-Carlo simulation has been frequently used [26,52,93,96–99]. The advantage of this method is that one can easily control each term and thus determine the precise origin of an observed effect. Note however that the validity regime of the adiabatic approximation becomes narrower for transitions with high angular momenta [52] because the energy separation between the levels is smaller: the probability for the atom to undergo a nonadiabatic transition is then all the more important. Nevertheless, in situations similar to the $\text{lin} \perp \text{lin}$ configuration, the localized atoms hardly attain the anti-crossing points, so that the semi-classical Monte-Carlo simulations remain valid to study the effects originating from the majority of atoms which are localized (temperature for instance).

Comment: For $J_g \geq 1$, the full set of potential curves can often be replaced by an effective bipotential [52]. The lowest curve of the bipotential corresponds to the lowest adiabatic potential, the upper curve being the average of the other potentials with a weight proportional to their populations.

4.4. The Monte-Carlo wavefunction approach

Introduced in 1992 [100], this method allows to handle a wide variety of dissipative problems in quantum optics without integrating the master equation Eq. (92). It consists of replacing the calculation of the atomic density matrix by the calculation of the temporal evolution of a statistical ensemble of wavefunctions. The required information for a quantity A is then obtained by averaging the corresponding observable \hat{A} over this statistical ensemble, instead of calculating the trace of $\sigma\hat{A}$.

Although a wavefunction approach is apparently incompatible with the existence of dissipation, spontaneous emission is taken into account here by the addition of a stochastic element to the Hamiltonian evolution of the “atom+quantized field” system: after a short phase dt during which the system has evolved under the effect of the atom-laser Hamiltonian, one calculates the probability dp that a spontaneous photon was emitted during dt (dt is chosen small enough to guarantee $dp \ll 1$). Comparing dp and a pseudo-random number uniformly distributed in $[0,1]$, one then makes a “gedanken measurement” which projects the wavefunction onto either of its components corresponding to 0 or 1 photon in the quantized field. The possibly emitted photon is destroyed immediately after being “detected”: one derives here the evolution of only the atomic part of the wavefunction.

This method is equivalent to the optical Bloch equation approach [100]. Its main advantage is that the size of the wavefunction scales as the number N of atomic states, while the density matrix scales as N^2 . This method is thus very powerful, in particular to handle the case of atomic transitions with high angular momenta. It has been used to calculate temperatures and fluorescence spectra in 1D and 3D molasses [68,101,102], and also to study anomalous diffusion in optical lattices [63]. The drawback of this method lies in a relative lack of transparency: it is indeed sometimes difficult to get a precise idea of the elementary phenomenons leading to a given macroscopical effect.

5. Probe transmission spectroscopy: vibration, propagation and relaxation

Probe transmission is obviously a widespread and efficient method to study the elementary excitations of an optically active medium. A first point that should be stressed is that this detection method is sensitive to the excitation modes of the *free* system (i.e. in the absence of probe) as long as signals *linear* into the probe are concerned. The only influence of the probe is to excite some particular dynamical modes of the system because of its polarization and its direction. In that respect, the information provided by this method is not qualitatively different from those obtained by fluorescence spectroscopy (Section 6). The use of one method or the other is thus not a question of principle but merely a question of convenience.

After a brief introduction (Section 5.1), we describe different types of processes that were studied with this method, among which we made a classification according to the detuning δ between the probe beam and the lattice beams. Starting from large values of $|\delta|$, we first describe Raman transitions between eigenstates of the light-shift Hamiltonian that are differently populated by the Sisyphus mechanism (Section 5.2). We then present Raman transitions between different vibrational levels inside the same potential well (Section 5.3). These Raman resonances being associated with transitions between atomic eigenstates, their position is independent of the probe direction. The next subsection concerns the observation of propagation modes associated with a single atom that give rise to resonances analogous to those found in Brillouin scattering (Section 5.4). In particular, the position of these resonances vary with the probe direction. The relevant parameter here is the velocity of the propagation mode. We continue this description with the central part of the probe transmission spectrum, i.e. the stimulated Rayleigh line which originates from light scattering on non-propagating modulation of atomic observables (Section 5.5). All these subsections deal with the steady-state regime but the study of the transmission in the transient regime (Section 5.6) provides the same information in a form that is sometimes more convenient. Finally, we describe multiphotonic effects that appear with a stronger probe beam (Section 5.7).

5.1. General considerations on probe transmission

The spatial evolution of a probe beam inside a material medium is found from the Maxwell equations. In the case of a dilute medium of length L and in the slowly varying envelop approximation, the variation of the complex amplitude E_p of the probe beam at the exit of the medium is

$$E_p(L) = E_p + \frac{ikL}{2\varepsilon_0} \mathcal{P}, \quad (98)$$

where \mathcal{P} is the complex amplitude of the Fourier component of the atomic polarization along the probe direction. For a weak monochromatic probe beam of frequency $\omega_p = \omega + \delta$ ($|\delta| \ll \omega$),

$$\mathcal{P} = \varepsilon_0 [\chi'(\omega_p) + i\chi''(\omega_p)] E_p, \quad (99)$$

where $\chi = \chi' + i\chi''$ is the probe *linear susceptibility*. Eq. (98) thus becomes

$$E_p(L) = E_p \left[1 + \frac{kL}{2} (-\chi''(\omega_p) + i\chi'(\omega_p)) \right]. \quad (100)$$

Usually, one measures the intensity of the transmitted probe beam $|E_p|^2(1 - \chi''kL)$ and finds therefore the spectral dependence of $\chi''(\omega_p)$ when the probe beam frequency is scanned.

Comments: (i) From the knowledge of χ'' , one can deduce χ' using the *Kramers–Krönig* relation

$$\chi(\Omega) = \frac{i}{\pi} \int_{-\infty}^{+\infty} \frac{\chi(\omega)}{\Omega - \omega} d\omega. \quad (101)$$

(ii) In most situations, the linear susceptibility is a tensor $\chi_{ij}(\omega_p)$ rather than a scalar. In optical lattices, the directions along which this tensor is diagonal can often be deduced from symmetry arguments.

5.2. Raman transitions between eigenstates of the light-shift Hamiltonian

In a probe transmission spectrum, broad resonances are found for probe detunings on the order of the light-shift Δ' . These resonances correspond to Raman transitions between potential surfaces associated with eigenstates of the light-shift Hamiltonian which are differently populated by the sub-Doppler cooling mechanism. In principle, a resonant enhancement of the absorption ($\chi'' > 0$) is found for $\delta > 0$, which corresponds to a Raman process where a probe photon is absorbed and a photon is emitted in the lattice beams; conversely, a resonant enhancement of the probe amplification ($\chi'' < 0$) is found for $\delta < 0$ with a permutation between the probe and the lattice beams in the Raman process. The width of these resonances is on the order of or larger than the optical pumping rate Γ_p (the spatial dependence of the light-shifts can contribute to an inhomogeneous width). This type of resonances was first observed by Grison et al. [103] and Tabosa et al. [104].

Examples of resonances observed in 3D four-beam optical lattices (lin \perp lin lattice, see Section 3.3.4, and Rot[lin \perp lin] lattice, see Section 3.5.2, with $\theta = 55^\circ$) are shown in Fig. 21. The experiments [89] are performed with cesium atoms. The lattice beams are tuned to the red side of the $6S_{1/2}(F=4) \rightarrow 6P_{3/2}(F'=5)$ transition ($\Delta = -13\Gamma$), the light-shift per beam being $\Delta'_0 \simeq -65E_R$. The transverse probe propagates along the Ox axis. In the lin \perp lin case (Fig. 21a), the broad resonance is observed with a π -polarized probe and the absorption peak Ω_S is significantly larger than the amplification peak. The asymmetry between absorption and amplification first arises from the different Clebsch–Gordan coefficients for the probe absorption ($F, m \nearrow_p F+1, m \searrow F, m \pm 1$) and the probe amplification ($F, m \nearrow F+1, m \pm 1 \searrow_p F, m \pm 1$). However the main reason is that the atoms are localized around sites where the lattice field has a pure circular polarization. (Note that m is a good quantum number at points where the light is σ^+, σ^- or π polarized.) Because of the weak intensity of the minority circular polarization (σ^+ for example), the Raman process $F, m = -F \nearrow F+1, m = -F+1 \searrow_p F, m = -F+1$ is reduced and therefore the probe amplification also. Furthermore, the Clebsch–Gordan coefficient connecting $F, m = -F$ to $F+1, m = -F+1$ is also small for large F . For a σ -polarized probe, the analogous resonances are weaker and this is due to the combined effect of strong localization and smaller Clebsch–Gordan coefficients.

The spectra obtained with Rot[lin \perp lin] lattice are markedly different. First, with a π -polarized probe the Ω_S resonance is almost absent and this is explained by the fact that for $\theta = 55^\circ$, the atoms are localized around sites where the lattice field is π -polarized (see Section 3.5.2).

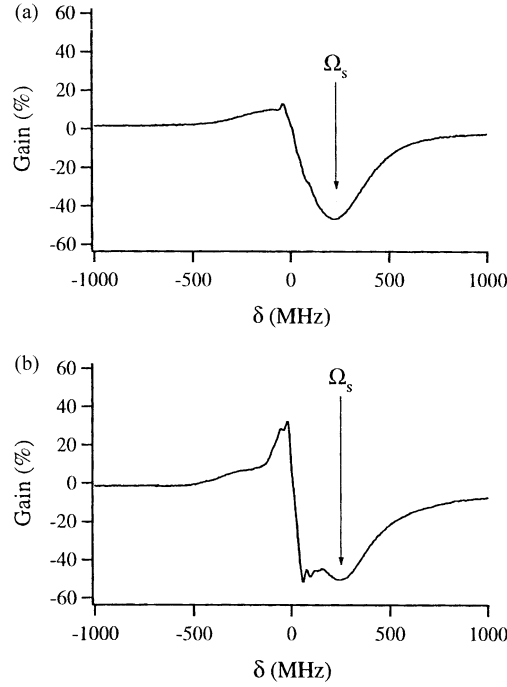


Fig. 21. Probe transmission spectrum in a Cs four-beam optical lattice on the red side of the $6S_{1/2}(F=4) \rightarrow 6P_{3/2}(F'=5)$ transition. The probe frequency is scanned here on a relatively large range to observe transitions between different eigenstates of the light-shift Hamiltonian. (a) Lin \perp lin lattice with $\theta_x = \theta_y = \theta = 55^\circ$. The probe is π -polarized. (b) Rot[lin \perp lin] lattice with $\theta = 55^\circ$. The probe is σ -polarized. From Mennerat-Robilliard et al. [89].

Therefore, a Raman process between two Zeeman substates of different magnetic quantum number m cannot be induced by the two π -polarized fields. By contrast, the Ω_s resonance is observed with a σ -polarized probe (Fig. 21b).

These examples show that the relative magnitude of these broad resonances for different probe polarizations gives valuable information on the atomic localization inside the lattice.

Comment: In the case of *grey molasses*, the asymmetry between absorption and amplification is even more important, the amplification being vanishingly small [105]. This is because most atoms are optically pumped into the internal dark state and because the molasses field does not connect the internal dark state to the excited state.

5.3. Raman transitions associated with the vibrational motion

When an atom is trapped inside a potential well, it oscillates around the potential minimum. The probe transmission spectrum exhibits resonances located at the frequency of this oscillation. We present now the characteristics of these resonances in the oscillating (Section 5.3.1) and jumping (Section 5.3.3) regimes. Although a quantum approach is often used to describe these resonances, a classical point of view (Section 5.3.2) also provides some valuable information with a simple formalism.

5.3.1. Oscillating regime

In a potential well of depth U_0 , the oscillation frequency Ω_v is on the order of $\sqrt{E_R U_0}$ (see Section 3.2.5). Because $U_0 \sim |\Delta'|$ and (generally) $E_R \ll |\Delta'|$, one finds $\Omega_v \ll |\Delta'|$. Therefore the resonances associated with the vibration motion occur at a probe detuning ($\delta \sim \Omega_v$) smaller than the one ($\delta \sim |\Delta'|$) associated with transitions between different potential surfaces. These vibrational resonances were first reported in [1,2] and their main characteristics were described by Courtois and Grynberg [72].

The origin of these resonances can be easily understood in the quantum approach. Because of the population difference between the vibrational levels (see Section 3.2.5), stimulated Raman processes occur with probe amplification when $\delta = -\Omega_v$ (Fig. 22a) and with probe absorption when $\delta = \Omega_v$ (Fig. 22b).

Examples of probe transmission spectra in a 3D four-beam $\text{lin} \perp \text{lin}$ lattice (Section 3.3.4) filled with cesium atoms are shown in Figs. 22c and d. The experiment is performed on the red side of the $6S_{1/2}(F=4) \rightarrow 6P_{3/2}(F'=5)$ transition with $\Delta = -15\Gamma$, $\Delta'_0 = -190E_R$ and $\theta_x = \theta_y = 30^\circ$ [106]. Fig. 22c obtained with a probe propagating along Oz (and polarized along a direction orthogonal to that of the copropagating lattice beams) shows evidence of vibrational resonances located in $\delta = \Omega_z$ and $-\Omega_z$. Fig. 22d obtained with a probe propagating along Ox (and polarized along Oy) shows other vibrational resonances located in $\delta = \Omega_x$ and $-\Omega_x$. The occurrence of different vibrational frequencies is not surprising because the potential wells do not have a spherical symmetry in the general case. More precisely, the bipotential for a $J_g = 1/2 \rightarrow J_e = 3/2$ transition can be found from Eqs. (43) and (74) and an expansion near the potential minima gives

$$\begin{aligned} \hbar\Omega_{x,y} &= 2 \sin \theta_{x,y} \sqrt{3U_0 E_R} , \\ \hbar\Omega_z &= 2(\cos \theta_x + \cos \theta_y) \sqrt{U_0 E_R} , \end{aligned} \quad (102)$$

where $U_0 = -4\hbar\Delta'_0/3$ is the depth of the 1D optical potential. The dependence of the vibrational frequencies with the angles θ_x and θ_y has been studied by Verkerk et al. [42] and Morsch et al. [107]. The proportionality to $\sqrt{|\Delta'_0|}$ has also been checked by varying both the beams intensity and the detuning from resonance Δ [89,107].

Comments: (i) Eqs. (102) for the vibration frequencies are adapted to the particular case of a $J_g = 1/2 \rightarrow J_e = 3/2$ transition. In a more general situation, it is necessary to expand the adiabatic potential near the potential minima. For a sufficiently large value of J_g (typically $J_g \geq 3$), the following formulas are a better approximation of the vibration frequency:

$$\begin{aligned} \hbar\Omega_{x,y} &= \sin \theta_{x,y} \sqrt{2\hbar|\Delta'|E_R} , \\ \hbar\Omega_z &= (\cos \theta_x + \cos \theta_y) \sqrt{\hbar|\Delta'|E_R} . \end{aligned} \quad (103)$$

(ii) The relative intensities of the vibrational transitions between the levels $\{n\} = \{n_x, n_y, n_z\}$ and $\{n'\} = \{n'_x, n'_y, n'_z\}$ of a $\text{lin} \perp \text{lin}$ lattice are given in the case of a $J_g = 1/2 \rightarrow J_e = 3/2$ transition by

$$I(m, \{n\} \rightarrow m, \{n'\}) \propto [\pi(\{n\}) - \pi(\{n'\})] |\langle m, \{n\} | \hat{\mathcal{P}} | m, \{n'\} \rangle|^2 , \quad (104)$$

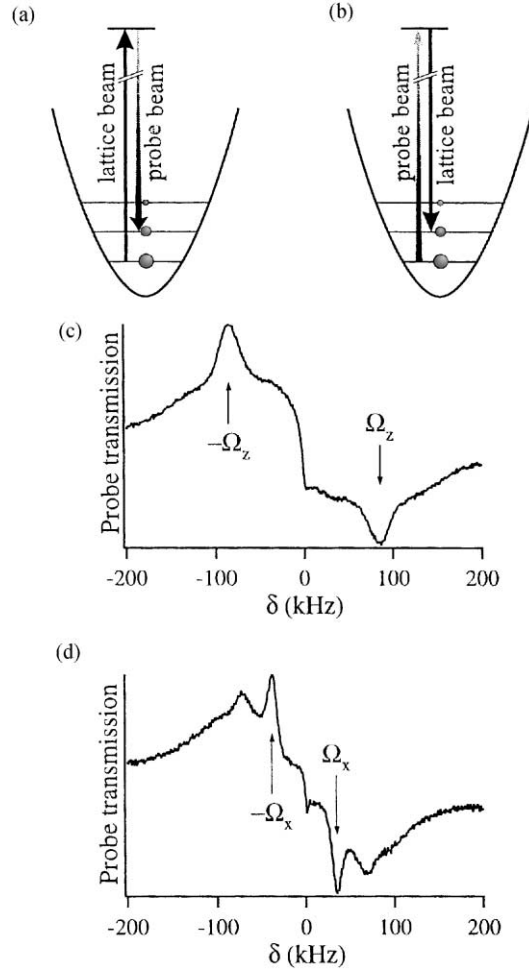


Fig. 22. Raman transitions between vibrational levels. (a) Absorption of a photon of a lattice beam and stimulated emission of a probe photon. (b) Reverse process with probe absorption. (c) and (d) Probe transmission spectra in a 3D four-beam lin \perp lin lattice filled with cesium atoms. The probe propagates along Oz in (c) and along Ox in (d). Spectrum (c) is obtained with a x -polarized probe (i.e. its polarization is orthogonal to that of the copropagating lattice beams). From Grynberg and Triché [106].

where m is an eigenvalue of J_z/\hbar and $\pi(\{n\})$ is the population of the vibrational level n_x, n_y, n_z . The operator $\hat{\mathcal{P}}$ is equal to

$$\hat{\mathcal{P}} = \frac{E_{p-}^*(\mathbf{R})E_-(\mathbf{R})}{E_0E_p} \left(1 - \frac{J_z}{\hbar}\right) + \frac{E_{p+}^*(\mathbf{R})E_+(\mathbf{R})}{E_0E_p} \left(1 + \frac{J_z}{\hbar}\right), \quad (105)$$

where $E_-(\mathbf{R})$ and $E_+(\mathbf{R})$ are the circular components of the lattice field given in Eq. (74) and $E_{p-}(\mathbf{R})$ and $E_{p+}(\mathbf{R})$ the circular components of the probe beam. The extension of Eqs. (104) and (105) to higher angular momenta gives different coefficients for the magnetization term and requires the introduction of tensors of higher rank [72].

Note that Eq. (105) shows that a probe propagating along Oz cannot excite the Ω_x resonance ($n'_x - n_x = \pm 1$, $n'_y = n_y$, $n'_z = n_z$) because there is no term linear in X in the expansion of the operator $\hat{\mathcal{P}}$ whatever the probe polarization.

(iii) Experimental spectra often show the occurrence of overtones located in the vicinity of $2\Omega_x$, $2\Omega_y$ or $2\Omega_z$, depending on the probe direction. These overtones have weaker intensities because they appear at a higher order in the expansion in R/λ of the fields in Eq. (105) (see also Section 3.2.5).

(iv) Soon after the observation of the vibrational resonances, it was realized that their position slightly differs from Ω_v [72]. Indeed, accurate measurements [107,108] show that the center of the resonance is found at a frequency smaller than Ω_v . This is due to the anharmonicity of the potential that we discuss now in the 1D lin \perp lin case and for a $J_g = 1/2 \rightarrow J_e = 3/2$ transition. The expansion of $U_-(Z)$ (Eq. (44)) to order 4 in kZ gives an additional term $-U_0(kZ)^4/3$ to the harmonic expansion in Eq. (65). Considering this supplementary term as a small correction, one obtains using perturbation theory to first order:

$$E_{n+1} - E_n = \hbar\Omega_v - (n+1)E_R. \quad (106)$$

The resonance frequency is thus shifted to a lower value and the distance between two consecutive vibrational transitions is equal to the recoil frequency. This splitting between the vibrational lines has not been observed yet but an indirect evidence for it was obtained through the observation of revivals in transients [109].

Because all these vibrational resonances overlap, one can estimate the location of the centre of their superposition. The weight p_n of the $n \rightarrow n+1$ line, deduced from Eq. (104), is proportional to $[\pi(n+1) - \pi(n)](n+1)$ (the factor $(n+1)$ originates from the matrix element of Z that appears in the field expansion). Assuming a Boltzmann distribution with a temperature T for $\pi(n)$, one finds an average shift $\xi_v \simeq -(k_B T / 2U_0) \Omega_v$.

Because $k_B T / U_0 \simeq 0.28$ (see Section 3.2.3), this model predicts a relative shift ξ_v / Ω_v on the order of 14%, in reasonable agreement with experimental observations [108]. This is also in agreement with the result of a full quantum calculation [72].

(v) Since the first observation of vibrational transitions [1,2], their width was a subject of considerable discussion. First, it was realized that their width was much smaller than the photon scattering rate Γ' because the strong elastic component (Section 3.2.5) does not contribute to the width [72]. If the vibrational lines were well isolated, the width of each vibrational line would be given by half the sum of their lifetimes which are given by Eqs. (66) and (67). The width of the $n \rightarrow n+1$ transition would thus be on the order of $n\Gamma'(E_R/\hbar\Omega_v)$ [72]. Although this is smaller than Γ' because of the Lamb–Dicke factor, the observed width is generally even smaller: this is because in a harmonic potential the transfer of coherence gives much narrower lines [10]. In fact, in the framework of this model one predicts a linewidth on the order of $2\hbar\Gamma_p(E_R/\hbar\Omega_v) \sim \Gamma_p(k_B T / 2U_0)$ [106]. However, anharmonicity prevents a full transfer of coherence and accounts for a significant fraction of the width. In fact, it was shown experimentally by Morsch et al. [107] that there is a relatively large range of parameters where the width is proportional to Ω_v . Such a relation appears naturally if the width corresponds to the mean quadratic value of the anharmonic shifts (see also comment (i) in Section 5.3.2).

(vi) A more correct method to predict the lineshape consists of calculating the density matrix σ of the system (Section 4) and to deduce from it the probe absorption [72]. In the presence

of the probe beam, the steady-state density matrix σ can be written as a Fourier expansion

$$\sigma = \sigma_0 + (\sigma_1 \exp - i\delta t + \sigma_1^\dagger \exp i\delta t) + \dots \quad (107)$$

The absorption χ'' in a $\text{lin} \perp \text{lin}$ lattice is then given by [72]

$$\chi'' = C_0 \text{Im} \left\{ \left(A'_0 - i \frac{\Gamma'_0}{2} \right) \text{Tr} \hat{\mathcal{P}} \sigma_1 \right\}, \quad (108)$$

where C_0 is a constant proportional to the atomic density. In the case of the $1/2 \rightarrow 3/2$ transition, the transition operator $\hat{\mathcal{P}}$ writes

$$\hat{\mathcal{P}} = \left[\sum_{j \parallel p} e^{i(\mathbf{k}_j - \mathbf{k}_p) \cdot \mathbf{R}} - \frac{J_z}{\hbar} \sum_{j \perp p} e^{i(\mathbf{k}_j - \mathbf{k}_p) \cdot \mathbf{R}} \right]. \quad (109)$$

In this expression, $\sum_{j \parallel p}$ (*resp.* $\sum_{j \perp p}$) means that the summation runs over the lattice beams having the same polarization as the probe beam (*resp.* a polarization orthogonal to that of a probe beam). This formalism was applied to 1D lattices in [72].

5.3.2. Semi-classical approach to atom dynamics

In classical terms, the action of the probe is to shake the potentials and thus to induce the oscillation motion. For the $J_g = 1/2 \rightarrow J_e = 3/2$ transition and a 3D $\text{lin} \perp \text{lin}$ lattice, the potential $U_-(t)$ associated with $|m_g = -1/2\rangle$ becomes $U_- + U_-^{(p)}$ where U_- is given by Eq. (43) and

$$U_-^{(p)} = 2 \frac{\hbar A'_0}{I} \left[\left(E_{p-}^*(\mathbf{R}) E_-(\mathbf{R}) + \frac{1}{3} E_{p+}^*(\mathbf{R}) E_+(\mathbf{R}) \right) e^{i\delta t} + \text{c.c.} \right]. \quad (110)$$

The force acting on the atom $\mathbf{F} = -\nabla U_-(t)$ can be expanded in the vicinity of a minimum of U_- (for example $\mathbf{R} = 0$). The lowest order term gives a driving force oscillating at frequency δ . Among the higher order terms, some lead to a parametric excitation, resonant when $\delta = 2\Omega_j$ ($j = x, y$ or z). These resonances correspond to a transition $n'_j - n_j = 2$ in the quantum description (see Section 5.3.1, comment (iii)).

In the case of the 1D $\text{lin} \perp \text{lin}$ lattice, $U_-^{(p)}$ and $U_+^{(p)}$ can be easily calculated and this is interesting to illustrate the influence of the probe polarization. We thus assume that the probe beam $E_p \sin(k_p z - \omega_p t)$ propagates in the $+z$ direction and that its polarization is either \mathbf{e}_y or \mathbf{e}_x . In the first case (labelled \perp), the probe has a polarization perpendicular to the copropagating lattice beam. In the second case (labelled \parallel), both have the same polarization. The shifted potentials are [72]

$$U_{\pm}^{(p)} = U_0 \frac{E_p}{E_0} \left[-\cos(2kZ - \delta t) \pm \frac{1}{2} \cos \delta t \right] \quad (111)$$

for a \perp probe and

$$U_{\pm}^{(p)} = U_0 \frac{E_p}{E_0} \left[\pm \frac{1}{2} \sin(2kZ - \delta t) + \sin \delta t \right] \quad (112)$$

for a \parallel probe (similar studies were also performed in 2D four-beam lattices [110]). The total potentials $U_+(t)$ and $U_-(t)$ at different time intervals are shown in Figs. (23) and (24). It can be seen that the potentials oscillate back and forth around their mean value and this is the source

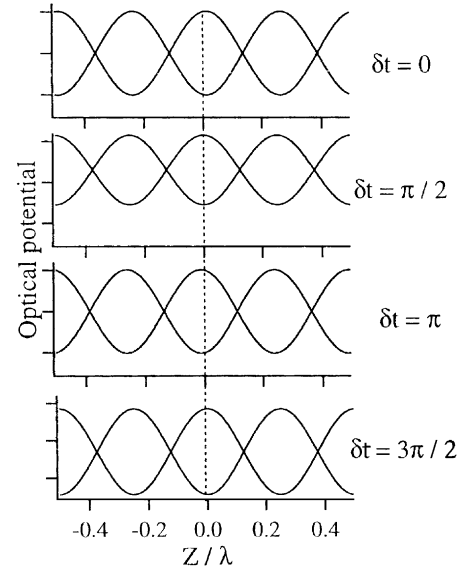
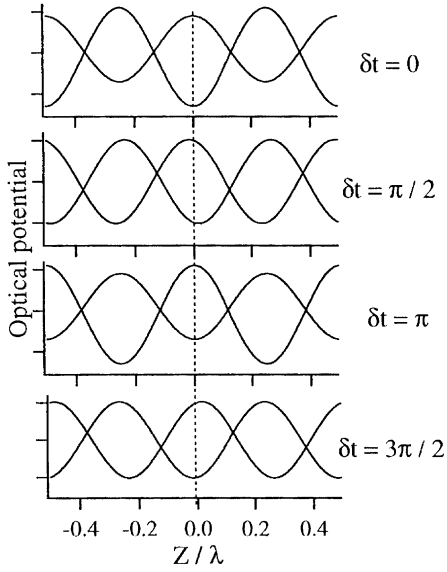


Fig. 23. Optical bipotential for a probe having a polarization orthogonal to the one of the copropagating lattice beam (\perp configuration). The shape of the potentials is represented at four different times during a period $T = 2\pi/|\delta|$.

Fig. 24. Optical bipotential for a probe having a polarization parallel to the one of the copropagating lattice beam (\parallel configuration). The shape of the potentials is represented at four different times during a period $T = 2\pi/|\delta|$.

of the Raman resonance occurring at $\delta = \Omega_v$. It can also be seen that the potential curvature oscillates periodically and this induces the *parametric* excitation. Finally, it can be noticed in Figs. 23 and 24 that the depths of the two potentials oscillate in phase in the \parallel case and that they are π phase-shifted in the \perp case.

For the evaluation of the additional force $-\nabla U_p^{(\pm)}$, the only relevant term is the first term in the brackets of Eqs. (111) and (112) because it is space dependent. This term is twice as large for the \perp probe, which thus excites more efficiently the vibrational motion.

To be more precise, consider as an example the motion of an atom in the σ^- well located in $z=0$ of a 1D lattice, and submitted to a \perp probe. The atom's dynamics is described by the equation

$$\frac{d^2 Z}{dt^2} + \frac{\alpha}{M} \frac{dZ}{dt} + \frac{\Omega_v^2}{2k} \sin 2kZ = \frac{\Omega_v^2 E_p}{k E_0} \sin(\delta t - 2kZ). \quad (113)$$

As a first approximation, we can assume that the atom remains in the neighbourhood of $Z=0$. Using $\sin 2kZ \sim 2kZ$ and $\sin(\delta t - 2kZ) \sim \sin \delta t$, we find the equation of a driven harmonic oscillator which exhibits a resonance when $\delta = \Omega_v$.

A more precise approximation is to expand $\sin(\delta t - 2kZ)$ to first order in kZ . We then find an additional driving term $-2kZ \cos \delta t$ which yields a parametric resonance when $\delta = 2\Omega_v$.

If we expand the static dipole force up to terms of order $(kZ)^3$, we find an anharmonic contribution $-2k^2 \Omega_v^2 Z^3/3$. If $\delta \sim \Omega_v$, the equation of motion can have more than one stable

steady state. In fact, in a certain range of parameters, two stable oscillations with different amplitudes are found [111]. An experimental evidence of this mechanical bistability in an optical lattice is presented in Section 5.7.1. If the driving force has a frequency $\delta \sim \Omega_v/3$, the unperturbed oscillation $Z_0 = \text{Re}[ae^{i\delta t}]$ yields, due to the anharmonic term, a driving force oscillating at frequency 3δ . Because $3\delta \sim \Omega_v$, the mechanical resonance can be excited [111]. Such a nonlinear resonance has been observed experimentally (see Section 5.7.2) and can be interpreted as a hyper-Raman transition in the lattice.

Comments: (i) The shift of the vibrational resonance due to anharmonicity and temperature can also be easily found from Eq. (113). Instead of expanding $\sin 2kZ$ around $Z=0$, the expansion is performed around Z_0 which differs from 0 because of fluctuations. The new frequency $\Omega_v[\cos(2kZ_0)]^{1/2}$ is shifted from Ω_v by a quantity $\xi(Z_0)_v \simeq -k^2 Z_0^2 \Omega_v$. Using $M\Omega_v^2 \overline{Z_0^2} = k_B T$ and $\Omega_v = 2\sqrt{E_R U_0}$ yields an average shift $\bar{\xi}_v = -(k_B T/2U_0)\Omega_v$, in perfect agreement with the result of the quantum analysis (Section 5.3.1, comment (iv)).

If the width of the resonance is to be associated with the dispersion of anharmonicity (see comment (v) in Section 5.3.1), it should vary as the mean quadratic value of $[\xi(Z_0)_v - \bar{\xi}_v]$, a quantity equal to $\sqrt{2}\bar{\xi}_v$. It turns out that this analysis is in reasonable agreement with the experiments [107].

(ii) The probe beam is also the source of a time-dependent dissipation [72]. The fact that optical pumping exhibits a periodic variation at frequency δ has important consequences on the relative occupation of σ^+ and σ^- wells (see Section 5.5.1).

(iii) Once the atomic motion $\mathbf{R}(t)$ is known, the transmission of the probe can be evaluated by a method similar to the one described in Section 5.3.1 (comment (vi)) for the quantum case. The formula for χ'' is identical to Eq. (108) but for the replacement of $\text{Tr}(\hat{\mathcal{P}}\sigma_1)$ by $\overline{\hat{\mathcal{P}} \exp i\delta t}$, where $\hat{\mathcal{P}}$ is given by Eq. (109) with a time-dependent \mathbf{R} and the average is taken on the internal state and on the classical probability distribution of amplitude and phase.

In the case of a 3D four-beam $\text{lin} \perp \text{lin}$ lattice and a y -polarized probe (called \perp configuration in the limit $\theta_x = \theta_y = 0$), using the notation $Z = \sqrt{2A} \sin(\delta t + \zeta)$ for the position relative to the potential minima along the z axis (and $X = Y = 0$) one finds

$$\begin{aligned} \overline{\hat{\mathcal{P}} \exp i\delta t} = & \left[2 \int dA d\zeta J_1[k(1 + \cos \theta_y)\sqrt{2A}] e^{-i\zeta} \{ \Pi_+(A, \zeta) + \Pi_-(A, \zeta) \} \right. \\ & \left. - \int dA d\zeta J_1[k(1 - \cos \theta_x)\sqrt{2A}] e^{-i\zeta} \{ \Pi_+(A, \zeta) - \Pi_-(A, \zeta) \} \right], \end{aligned} \quad (114)$$

where $\Pi_{\pm}(A, \zeta)$ is the quasipopulation in phase space expressed using the $\{A, \zeta\}$ coordinates and in the $m_g = \pm 1/2$ sublevel [112].

Note that in the case of large detunings ($|A| \gg \Gamma$), the absorption is proportional to $\text{Im} \overline{\hat{\mathcal{P}} e^{i\delta t}}$ and therefore to the average value of $\sin \zeta$, which is reasonable because ζ corresponds to the phase-shift between the force (see Eq. (111)) and the position.

5.3.3. Jumping regime

In the jumping regime, the atom undergoes many jumps between the potential surfaces during a single oscillation period. If nonadiabatic terms can be neglected, the relevant force acting on

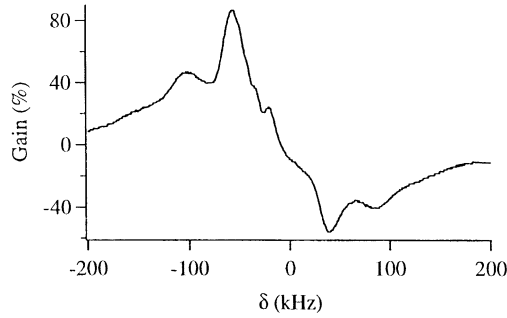


Fig. 25. Probe transmission spectrum in a Rot[lin ⊥ lin] lattice filled with cesium atoms. The probe is polarized along Oz . Narrow vibrational resonances are observed. From Mennerat-Robilliard et al. [89].

the atom is $-\sum_n \Pi_n \nabla U_n$, where Π_n is the average population in the n th potential surface (see Section 3.3.1). In the case of a restoring force linear in the amplitude of the displacement, a harmonic motion is found. This motion also leads to sharp vibrational resonances, as shown by Mennerat-Robilliard et al. [89,113]. To achieve the jumping regime, they used a Rot[lin ⊥ lin] configuration with $\theta = 55^\circ$ (see Section 3.5.2). In this case, the atoms are mostly located near sites where the light is linearly polarized along Oz and they jump from one potential to the other at the optical pumping rate. An example of vibrational spectrum obtained on the red side of the $6S_{1/2}(F=4) \rightarrow 6P_{3/2}(F'=5)$ cesium transition ($\Delta = -13\Gamma$) and for a light-shift per beam $\Delta'_0 = -90E_R$ is shown in Fig. 25. This recording was obtained with a π -polarized transverse probe, i.e. propagating along Ox . Here again the variation of the position Ω_x of the resonance with $|\Delta'_0|$ is in reasonable agreement with a square root law [89].

Although the atoms remain in the same potential surface for a time shorter than Γ_p^{-1} , the width of the vibrational resonance is much narrower than Γ_p . As shown by Mennerat-Robilliard et al. [113], this is due to a motional narrowing effect [114]. Let us denote Ω_n the vibration frequency associated with the n th potential curve. One can define an average frequency $\bar{\Omega} = \sum_n \Pi_n \Omega_n$ and a dispersion $\sigma = [\sum_n \Pi_n (\Omega_n - \bar{\Omega})^2]^{1/2}$. The vibrational resonance is centred in $\bar{\Omega}$ and the frequency dispersion contributes to the width by a term on the order of $\sigma^2 \Gamma_p^{-1}$ only. This is smaller than σ by a factor σ/Γ_p which decreases when Γ_p increases. The random and fast sampling of different potential curves transforms here a broad inhomogeneous width into a narrow homogeneous width.

Comment: Probe transmission was used by Schadowinkel et al. [88] to show the localization and the oscillation of atoms at the bottom of potential wells in a magneto-optical trap. This experiment gives actual evidence that a magneto-optical trap with well stabilized phases is closely related to a lattice.

5.4. Propagating excitation. The Brillouin-like resonance

In fluids, light scattering on propagative excitation modes such as sound waves gives rise to Brillouin resonances [115,116]. Identical processes have not been observed up to now in optical lattices because the density is generally too low to have sufficient particle interactions. However,

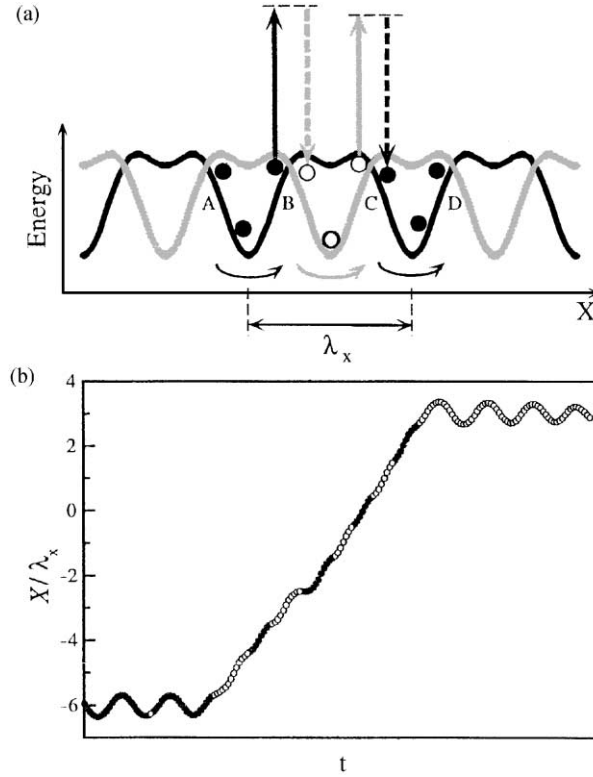


Fig. 26. (a) Section of the optical bipotential of a $J_g = 1/2 \rightarrow J_e = 3/2$ four-beam $\text{lin} \perp \text{lin}$ lattice along the direction $Y = Z = 0$. An atom can propagate along this periodic structure through a sequence of half-oscillations in a well followed by optical pumping transitions. (b) Example of atomic trajectory: the empty (resp. black) dots correspond to a $m = +1/2$ (resp. $m = -1/2$) state for the atom. From Courtois et al. [96].

a different propagative excitation mode is found in optical lattices. It consists of repeated cycles of half oscillations in a potential well followed by optical pumping towards an adjacent potential well [96].

Consider atoms in a four-beam $\text{lin} \perp \text{lin}$ lattice (Section 3.3.4). The variation of the optical potential along an x -axis connecting the potential minima is shown in Fig. 26a for the $J_g = 1/2 \rightarrow J_e = 3/2$ transition. The light polarization at the bottom of the wells is alternatively σ^+ and σ^- and the distance between two adjacent wells is $\lambda/2 \sin \theta_x$. Semiclassical Monte-Carlo simulations (Section 4.3) of the atomic motion [96] show that the dominant propagation mode along the x direction for delocalized atoms consists of the following steps: (i) half oscillation in a σ^- potential well (the atom moves from A to B); (ii) optical pumping from a σ^- to a σ^+ potential surface; (iii) half oscillation in a σ^+ potential well (the atom moves from B to C); (iv) optical pumping from a σ^+ to a σ^- potential surface; and so on. A typical example of computed trajectory is shown in Fig. 26b; an initially localized atom travels over eight potential wells before being trapped again. To estimate the velocity \bar{v} associated with this propagation mode, we remark that the atom travels from A to B , B to C in a typical time τ equal to half the oscillation period, i.e. $\tau = \pi/\Omega_x$. As $AB \simeq \lambda/2 \sin \theta_x$, we find $\bar{v} \simeq \Omega_x/k \sin \theta_x$.

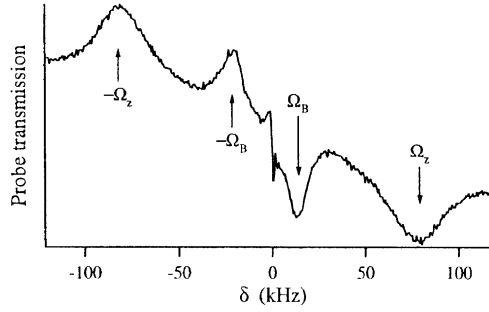


Fig. 27. Probe transmission spectrum in a 3D $\text{lin} \perp \text{lin}$ lattice filled with Cs atoms. The probe propagates along Oz and is y -polarized (its polarization is parallel to that of the copropagating lattice beams). The spectrum shows vibrational resonances located in $\pm\Omega_z$ and resonances associated with the propagating excitation in $\pm\Omega_B$. From Grynberg and Triché [106].

Such a density wave can be driven by the modulation of the optical potential and of the optical pumping rate induced by the lattice–probe interference pattern provided that its phase velocity along the x direction be equal to $\pm\bar{v}$.

Considering a lattice beam having the same polarization as the probe beam, the interference pattern moves along Ox with the velocity $v = \delta/(\mathbf{k}_p - \mathbf{k}) \cdot \mathbf{e}_x$ where \mathbf{k}_p and \mathbf{k} are the wavevectors of the probe and lattice beams respectively. The resonant driving condition $|v| = \bar{v}$ yields

$$\delta = \Omega_x \left| \frac{\sin \theta_x - \sin \theta_p}{\sin \theta_x} \right|, \quad (115)$$

where θ_p is the angle between \mathbf{k}_p and \mathbf{e}_z (note that θ_p and θ_x can have opposite signs).

The occurrence of a resonance when Eq. (115) is fulfilled has been checked experimentally and numerically by Courtois et al. in the limit of small θ_x and θ_p [96]. When the probe beam propagates along Oz , this Brillouin-like resonance is expected to be found near $\delta = \Omega_x$. This is what is observed in Fig. 27 where a spectrum obtained for $\theta_x = 30^\circ$, $\theta_y = 15^\circ$, $\Delta = -11\Gamma$ (detuning from the $6S_{1/2}(F=4) \rightarrow 6P_{3/2}(F'=5)$ Cs transition), $\Delta'_0 = -250E_R$ is shown. In spite of the fact that the Ω_B resonance is located at the expected position for the Ω_x vibration frequency, it does not correspond to a Raman vibrational transition, for several reasons. First, as explained in Section 5.3.1, this probe geometry does not permit the x vibrational mode to be excited. Second, when the probe polarization is rotated by $\pi/2$, the resonance disappears (see Fig. 22c). Third, when the probe direction changes the resonance Ω_B is shifted whereas a vibrational transition remains always located at the same frequency [96].

Comments: (i) Actually, the propagating excitation mode can be driven by the interference pattern created by the probe and any of the two copropagating lattice beams. It follows that when the probe is not aligned along Oz , the Ω_B resonance splits into two resonances corresponding to these two patterns. One resonance frequency is smaller than Ω_x and the second one higher [96].

(ii) The polarization pattern of the four-beam $\text{lin} \perp \text{lin}$ lattice promotes these propagation modes. In particular, it can be noticed that transitions from $m = -1/2$ to $+1/2$ are strongly

suppressed near the bottom of a σ^- potential well because the σ^+ intensity varies as x^4 (x being the distance to the potential minimum).

(iii) The mechanism of these Brillouin-like resonances, which requires spontaneous emission (i.e. a dissipative process) reminds the stochastic resonances [117].

5.5. Stimulated Rayleigh resonances—relaxation of nonpropagative modes

Rayleigh scattering results from the scattering of light on any nonpropagative modulation of atomic observables [64]. In the case of optical lattices and molasses, the observables that were considered up to now are the magnetization (Section 5.5.1), the density (Sections 5.5.2 and 5.5.3) and the velocity (Section 5.5.4). The width of the Rayleigh resonance gives information on the damping time of these observables.

5.5.1. Magnetization

In a $\text{lin} \perp \text{lin}$ lattice, the population is on average the same in the σ^+ and σ^- wells. When a probe beam is added, the balance between atoms in the $m = +J_g$ and in the $m = -J_g$ states can be broken, leading to a global magnetization of the lattice. If the probe–lattice detuning is δ , the magnetization oscillates at frequency δ but with a phase-shift with respect to the applied field because of the time delay τ_D associated with the atomic response time. The atomic polarization thus exhibits a nonzero component being $\pi/2$ phase-shifted with respect to the probe beam. The work of the probe field onto this component leads to the modification of its intensity as displayed by a resonance on the probe transmission spectrum. This resonance is centred around $\delta \simeq 0$ because it is associated to a nonpropagative observable and its width is on the order of τ_D^{-1} . In the general case, there is no phase-shift when $\delta=0$ and the transmitted probe is neither amplified nor absorbed. The generic shape of the stimulated Rayleigh resonance is thus dispersive with a peak-to-peak distance on the order of τ_D^{-1} [64].

To be more precise, we now discuss the particular case of the 1D $\text{lin} \perp \text{lin}$ lattice with a probe beam *cross-polarized* with the copropagative lattice beam [72]. In this situation labelled \perp in Section 5.3.2, the difference $(I^+ - I^-)$ between the two circular components of the total field is

$$I^+ - I^- = -E_0 E_p \cos \delta t. \quad (116)$$

The optical pumping is thus time-modulated. However there is not a single time constant τ_D for the magnetization here. The optical pumping rate depends on the vibrational level (see Eq. (66)) and different relaxation modes with different rates ranging from $\Gamma_p E_R / \hbar \Omega_v$ to Γ_p are expected to be involved in the Rayleigh scattering. The resonance thus appears as the sum of several dispersive curves with different peak-to-peak distances. This gives rise to an uncommon shape with a steep slope at the center and broad wings. This is indeed what was observed by Verkerk et al. [2]. Note that there is a persistent memory of this lineshape in the 3D $\text{lin} \perp \text{lin}$ lattice when the probe beam has a polarization orthogonal to that of the copropagating lattice beams (see Fig. 22c).

Comments: (i) In fact, the preceding analysis is oversimplified because it does not include the reactive effects and the density modulation [72]. As shown in Fig. 23, the probe also changes the relative depth of the σ^+ and σ^- wells. Optical pumping by the lattice beams tends to adapt the population in each state to the time-dependent modification of the potentials. The flow

of population back and forth between the σ^+ and σ^- wells creates a time-dependent density modulation having a spatial period $\lambda/2$. This density modulation gives a contribution to the Rayleigh resonance having an importance nearly equal to that of the magnetization [72].

(ii) In the \parallel configuration for the probe (Section 5.3.2), $(I^+ - I^-)$ is equal to $E_0 E_p \sin(\delta t - 2kz)$ in the 1D case. Because this field configuration induces the same time dependence in the evolution of $U_-(t)$ and $U_+(t)$ (see Fig. 24), the probe only induces a redistribution of population inside each well without any net transfer from σ^+ to σ^- wells or vice versa. The Rayleigh resonance originates from the time evolution of this antiferromagnetic magnetization grating [72]. The amplitude of this resonance is predicted to be very small and in most experiments it is hidden by noise or parasitic effects. An example of this kind of resonance was however reported for a 3D $\text{lin} \perp \text{lin}$ lattice (Fig. 13a of [106]).

5.5.2. Density—connection with spatial diffusion

The interference pattern created through the superposition of the probe and the lattice beams induces a variation of the optical potential and of the optical pumping which generally leads to a density modulation. Consider for example the interference created by a lattice beam (\mathbf{k}) and a probe beam (\mathbf{k}_p) of same polarization. A spatial variation of the form $N = \text{Re}[N_0 \exp i(\mathbf{k} - \mathbf{k}_p) \cdot \mathbf{r}]$ can be expected for the atomic density, N_0 being proportional to the probe amplitude. In the case where the density modulation relaxes by spatial diffusion with an isotropic spatial diffusion coefficient D_{sp} , the equation

$$\frac{\partial N}{\partial t} = D_{\text{sp}} \Delta N, \quad (117)$$

yields a relaxation rate γ_{sp}

$$\gamma_{\text{sp}} = D_{\text{sp}} |\mathbf{k} - \mathbf{k}_p|^2. \quad (118)$$

Thus, if the probe and the copropagating lattice beams have the same polarization, it is in principle possible to measure D_{sp} from the width of the Rayleigh line and this method has been used by Jurczak et al. [97]. However it must be emphasized that this requires a careful examination of the experimental conditions [118]. First, spatial diffusion is often anisotropic. In this case one should replace the right-hand side of Eq. (118) by $\sum_j D_j (\mathbf{k} - \mathbf{k}_p)_j^2$ where D_j are the eigenvalues of the spatial diffusion tensor. Second, a diffusion model cannot always be applied to the spreading of the atomic density. This requires that the mean free path is much smaller than the typical length scale $2\pi/|\mathbf{k} - \mathbf{k}_p|$ of the density modulation. In particular, when decreasing the optical potential depth, there can be a transition from Gaussian spatial diffusion to anomalous diffusion with Lévy walks [63,119] (see Section 6.3.2). It should also be noticed that escape channels along which atoms are accelerated can be found in 2D and 3D lattices [63].

Comment: In the case of free or almost free atoms the density modulation is washed out through ballistic atomic motion. The associated resonance corresponds to the derivative of the velocity distribution (generally a Gaussian with a peak-to-peak distance equal to $2|\mathbf{k} - \mathbf{k}_p| \sqrt{k_B T/M}$ where T is the atomic kinetic temperature) [64,120–123]. This “recoil-induced” resonance can be interpreted either in terms of stimulated Rayleigh scattering from the atomic density modulation in the probe–lattice interference pattern [122] or in terms of stimulated

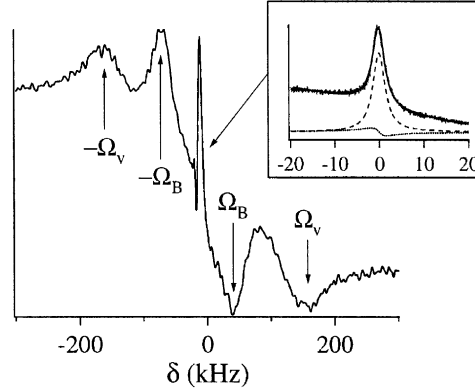


Fig. 28. Probe transmission spectrum in a 3D lin \perp lin lattice. The probe beam propagating along Oz has the same polarization as the copropagating lattice beams. The narrow central resonance (see inset) is very close to a Lorentzian. From Guibal et al. [99].

Raman (or Compton) scattering between differently populated atomic velocity groups [120,123] (see Section 6.1.1, comment (iii)).

5.5.3. Phase-shift between the density modulation and the interference pattern

The generic stimulated Rayleigh lineshape is dispersive with no probe gain when $\delta = 0$ [64]. However, probe transmission spectra recorded in optical lattices often show the occurrence of an almost lorentzian central structure, as shown in Fig. 28 [99]. This spectrum was obtained in a 3D lin \perp lin lattice filled with Rb atoms for $\theta_x = \theta_y = 20^\circ$, $\Delta'_0 = -200E_R$, $\Delta = -5\Gamma$. The probe is aligned along Oz and has the same polarization as the copropagating lattice beams. Apart from vibrational (Ω_z) and Brillouin-like (Ω_B) structures, one clearly distinguishes a central resonance with a maximum probe amplification for $\delta = 0$. The fit using an adjustable superposition of a lorentzian and a dispersion shown in the inset proves that this resonance is very close to a lorentzian.

The occurrence of gain for $\delta = 0$ shows that the density modulation induced by the probe has a component which is $\pi/2$ phase-shifted with respect to the probe-lattice interference pattern. In other words, the density modulation for $\delta = 0$ exhibits a shift with respect to the optical potential in the presence of the probe. As shown by Guibal et al., this shift originates from the radiation pressure [99]. Schematically, the probe and the copropagating lattice beams are in phase at the optical potential minima. The radiation pressure from the counter-propagating lattice beams is no longer balanced and the atoms are displaced towards another position where an equilibrium between radiation pressure and the dipole force is found. Because the ratio between radiation pressure and the dipole force originating from light-shift varies as $\Gamma/|\Delta|$ (Section 2.1), the resonance tends to distort from a lorentzian to a dispersion as $|\Delta|$ increases [99].

Comment: A similar beam coupling process is found in some photorefractive materials [124,125].

5.5.4. Velocity

Radiation pressure acting on an unbound atom in a molasses or a lattice oscillates at frequency δ because of the time variation of the relative phase between the probe and the lattice beams. Because of this driving force, the average velocity of these atoms also oscillates but with a phase shift depending on the relative value of the friction coefficient and the oscillation frequency. If the atomic polarization depends on the velocity, a Rayleigh resonance having a width on the order of the friction coefficient can be observed, as shown by Lounis et al. in the case of a 1D $\sigma^+ - \sigma^-$ molasses [126]. A detailed theoretical description of this resonance is presented by Courtois and Grynberg [127].

5.6. Coherent transients—another method to study the elementary excitations

In probe transmission spectroscopy, one generally studies the steady-state value of the probe transmitted intensity. However, it is also possible to interrupt the probe or to shift its frequency and study the transient atomic emission. If the probe is weak, the signals are proportional to the probe amplitude and the information contained in the transient spectrum is identical to that in the steady state spectrum. However, the transient signal can be more convenient for some measurements. In fact, this duality has been considered a few years ago in laser spectroscopy [128]. In optical lattices, the transient response of the probe has been used by Hemmerich et al. [41], Triché et al. [118,129] and Morsch et al. [107]. We first present this technique in Section 5.6.1 and then discuss a similar technique in Section 5.6.2, where no additional probe beam is needed as one monitors the lattice beams themselves to study the redistribution of photons among them.

5.6.1. Transient response of the probe beam

In the coherent transient method, the probe frequency is kept fixed until the atoms reach a steady state; then the probe frequency is suddenly switched from $\omega_p = \omega + \delta$ to ω'_p at time $t = 0$ (the intensity remaining constant). It is generally convenient to choose ω'_p such as the atoms do not interact with the probe after the switch. Thus the signal for $t > 0$ corresponds to the beat note between the probe at its new frequency and the light scattered by the atoms in the probe direction during their relaxation to their new steady state. Examples of signals obtained in a 3D $\text{lin} \perp \text{lin}$ lattice filled with Cs atoms are shown in Figs. 29a and c [129]. In this experiment, the probe is on the Oz symmetry axis and has the same polarization as the copropagating beams. The other conditions are $\theta_x = \theta_y = 55^\circ$, $\Delta = -14\Gamma$, $\Delta'_0 = -630E_R$, $\omega'_p - \omega_p = 1.5 \text{ MHz}$. Fig. 29a is obtained for a resonant Rayleigh excitation and Fig. 29c for a resonant Raman excitation ($\delta \simeq 125 \text{ kHz}$). These figures permit to measure the decay of non-propagative modes (Fig. 29a) and of the vibrational coherence (Fig. 29c). The square of the Fourier transforms of Figs. 29a and c are shown in Figs. 29b and d, respectively. By comparison with the probe transmission spectra shown earlier (Figs. 22 and 28), the interest of Figs. 29b and d is that there is almost no overlap between the Rayleigh and Raman resonances and it is possible to magnify one or the other by an appropriate choice of δ .

However, there is no additional information in the transient experiment. In fact, it can be readily shown that the amplitude of the Ω component of the Fourier transform of the transient

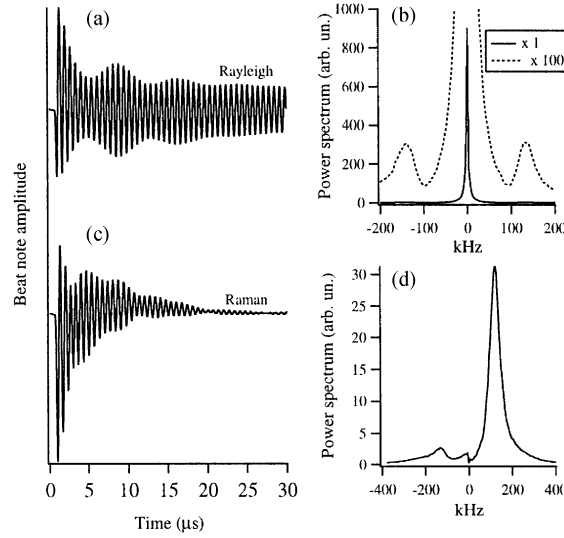


Fig. 29. (a) and (c) Transient spectra in the 3D lin \perp lin lattice for a probe propagating along Oz , having the same polarization as the copropagating lattice beams and producing (a) a resonant Rayleigh excitation and (c) a resonant Raman excitation. (b) and (d): Square of the Fourier transform of spectra (a) and (c), respectively. From Triché et al. [129].

is equal to [129]

$$S(\Omega) = \frac{kL}{8} E_p^2 \frac{\chi(\Omega) - \chi(\omega_p)}{\Omega - \omega_p}, \quad (119)$$

where L is the length along Oz of the atomic distribution. This equation shows that the same physical quantity $\chi(\omega)$ can be deduced from the transient and from the steady-state experiments. Furthermore, in the usual case where $\chi(\omega) \propto [(\omega - \omega_a) + i\Gamma_a]^{-1}$, it can be readily shown that $S(\Omega) \propto [(\Omega - \omega_a) + i\Gamma_a]^{-1}$. The same spectral dependence is therefore found for χ and S in this case.

5.6.2. Photon redistribution: a particular coherent transient

Instead of monitoring the transient signal on an additional probe beam, one can also use the lattice beams themselves and record their transient intensity after changing the optical potential in a coherent way. In this case, the intensity modulation of a lattice beam with wavevector \mathbf{k} originates from its interference with the light scattered from another lattice beam into the same direction \mathbf{k} .

This technique was demonstrated by Kozuma et al. [130] in a rubidium 1D optical lattice consisting of two beams with linear parallel polarizations, intersecting at an angle θ . These beams are tuned to the red side of the resonance ($\Delta < 0$) and their frequencies are, respectively, ω and $\omega + \delta_L$ (with $|\delta_L| \ll |\Delta|$). At time $t = 0$, δ_L is suddenly switched from 0 to more than 100 kHz, a value much larger than the atomic oscillation frequency in the potential wells. The atoms do not follow the potential moving at $v_0 = \delta_L / (2k \sin \theta/2)$ and experience an alternating dipole force as they cross the potential hills and wells. The corresponding photon

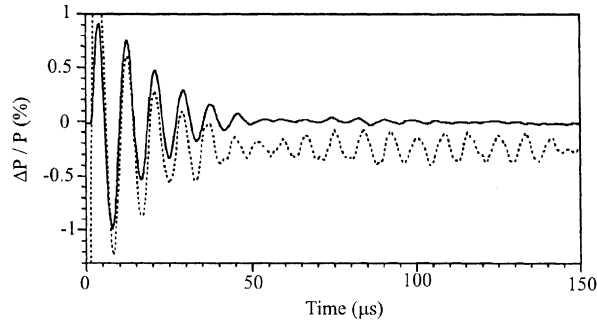


Fig. 30. Experimental (solid line) and theoretical (dotted line) power transfer ratio induced by wave packet oscillations initiated by a sudden shift of the optical potential $\delta z = 0.14\lambda$. $U_0 = 1000E_R$ and $A = -10\Gamma$. The theoretical line is obtained with quantum Monte-Carlo wavefunction simulations and is displaced from the experimental line for clarity. From Raithel et al. [109], reproduced by permission of the authors.

redistribution signal exhibits damped oscillations with a period δ_L . On the other hand, if one sets δ_L so that the kinetic energy of the atoms in the moving frame is much smaller than the optical potential depth, the atomic wave packets will remain localized in the moving potential. In this case, the period of the damped oscillations is the atomic vibration period, independently of the potential velocity [131]. In both experiments, the oscillations decay in a time on the order of 10 microseconds, which is much longer than the optical pumping time Γ_p^{-1} . Such a slow decay in a linearly polarized field can originate from a motional narrowing effect [114] (see Section 5.3.3) that prevents inelastic photon scattering from immediately washing out the coherences.

As these experiments are performed in the jumping regime, the signal decays after a few oscillations in the potential and the observation of effects associated with the quantization of the atomic motion is not expected. Making a similar experiment in the oscillating regime should allow a deeper insight in the nature—dispersive or dissipative—of the decay: dispersion through potential anharmonicity should give birth to a decay followed by quantum revivals provided that the vibrational motion is quantized, while dissipation through spontaneous emission should lead to a damping of the signal. Such an experiment was performed by Raithel et al. [109] with a 1D $\text{lin} \perp \text{lin}$ lattice, which means that the light polarization is circular at the bottom of the wells and consequently that dissipation is reduced by the Lamb–Dicke effect [8]. If one of the beams is suddenly phase-shifted after the atoms thermalize in the potential wells, the optical potential is spatially shifted. In a semi-classical picture, the atoms are on the edge of the potential wells and start oscillating in phase under the action of the dipole force. We show in Fig. 30 the experimental power transfer induced by coherent wave packet oscillations after a sudden shift of the lattice potential [109].

In agreement with the previous observations, the oscillations first decay with a time constant on the order of a few tens of μs . This time constant is not related to dissipation, but rather to the anharmonicity of the potential wells which induces a dephasing of the oscillations. This is confirmed by the existence in Fig. 30 of revivals corresponding to a subsequent rephasing of the oscillation. Note that a full analysis of the signal requires a quantum treatment to take

into account tunneling effects, the most appropriate description being the band model [109] (see Section 4.2).

Comments: (i) Such a transient experiment can also be performed by looking at the fluorescence of the atoms [132]. This is described in Section 6.2.4.

(ii) It is possible to stimulate a revival using two spatial shifts of the potential separated in time. This method, analogous to photon echoes [133], permits to measure the coherence relaxation time [134].

5.7. Intense probe beam

The situations where the driving of the atomic motion by the probe is no longer linear is interesting although it has not been studied very often in dissipative optical lattices. The effects already considered are mechanical bistability (Section 5.7.1) and hyper-Raman transitions involving several probe photons (Section 5.7.2).

5.7.1. Mechanical bistability

A forced nonlinear oscillator has two stable states in a large range of parameters [111]. One state corresponds to a large amplitude motion and the other to a small amplitude motion. A beautiful microscopic example of this mechanical bistability was provided by the cyclotron resonance of a relativistic electron revolving in a static magnetic field under the action of a nearly resonant electromagnetic wave [135–137]. Although experiments in optical lattices were mostly focused on the harmonic motion, mechanical bistability originating from the anharmonic terms in the potential (see Section 4.3.2) was also observed with atoms. The dynamics of an atom driven by a probe propagating along Oz in a σ^- well of a 1D $\text{lin} \perp \text{lin}$ lattice can be described by Eq. (113). In the case of a weak probe the atom remains close to $z=0$ and the harmonic expansion of the potential gives one steady-state solution $Z = \text{Im}[a \exp i(\delta t + \zeta)]$. However two solutions having different amplitudes of oscillation a_1 and a_2 can be found with an intense probe because of the potential anharmonicity [111]. This is because the detuning from the vibrational resonance is then a function of the amplitude itself and the equation that yields the amplitude is therefore nonlinear.

The experiment [118,138] is performed in two steps. In the first step, the atoms reach a steady state under the combined action of the lattice and probe beams and they attain an amplitude in the vicinity of a_1 or a_2 . In the second step, starting at time $t=0$, one records the coherent transient (see Section 5.6) that follows the abrupt switching of the driving probe to a new frequency. The emission from the lattice shows beats between transient oscillations of different frequencies. In fact, because of potential anharmonicity, the free oscillation frequency $\Omega(a)$ depends on the amplitude a . Therefore, two emission frequencies located around the values $\Omega_1 = \Omega(a_1)$ and $\Omega_2 = \Omega(a_2)$ associated with the two stable amplitudes a_1 and a_2 of oscillation in steady state are expected. The experiment is performed in a four-beam $\text{lin} \perp \text{lin}$ configuration. The lattice beams are tuned to the red side of the cesium $6S_{1/2}(F=4) \rightarrow 6P_{3/2}(F'=5)$ transition and the probe beam of frequency $\omega_p = \omega + \delta$ is sent along the Oz symmetry axis of the lattice. The amplitude $\tilde{S}(t)$ of the beat note signal between the transmitted probe and the light scattered by the atoms in the probe direction for $t > 0$ is shown in Fig. 31a. This curve, obtained with

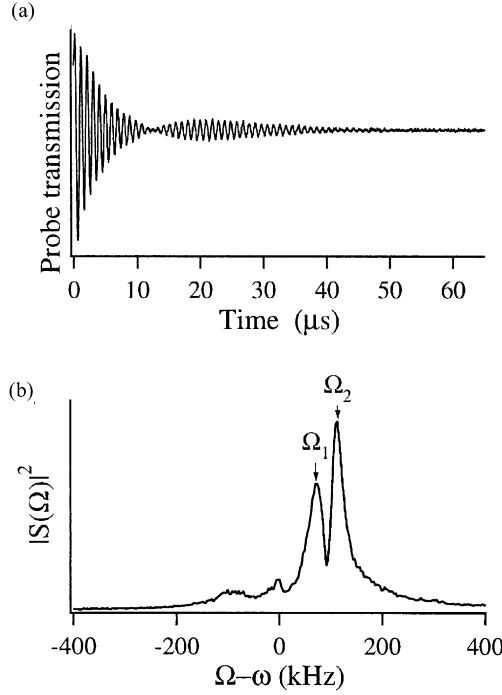


Fig. 31. (a) Transient emission of Cesium atoms in a lin \perp lin lattice after an interrupted probe excitation. The experimental conditions are $\Delta = -29\Gamma$, $I = 30 \text{ mW/cm}^2$, $I_p = 0.7 \text{ mW/cm}^2$, $\delta = 92 \text{ kHz}$. The fast oscillation corresponds to the beat frequency between the transmitted probe frequency ω_p' and the scattered light, having a frequency in the neighborhood of $\omega + \Omega_v$. The slow oscillation shows that the distribution of frequency of the scattered light has two peaks located in $\omega + \Omega_1$ and $\omega + \Omega_2$. Note that the signal has been filtered to eliminate the weak contribution of the Rayleigh component and of the anti-resonant Raman component. (b) Square of the Fourier transform of the transient emission. The horizontal axis has been shifted so that $\Omega = \omega$ corresponds to the static response. Two peaks located in Ω_1 and Ω_2 are clearly visible in the figure. From Grynberg et al. [138].

$I_p/I \approx 2 \times 10^{-2}$, can be interpreted as arising from the beat between two damped oscillators having different free oscillation frequencies. Such an image is confirmed by the observation of $|S(\Omega)|^2$ (Fig. 31b), where $S(\Omega)$ is the Fourier transform of $\tilde{S}(t)$. Two peaks located in Ω_1 and Ω_2 are clearly observed on this figure. These peaks are located on both sides of the excitation frequency δ and the values of Ω_1 and Ω_2 are smaller than the value Ω_v predicted for the harmonic frequency. The relative intensities of the peaks are related to the atomic population in the neighbourhood of each steady state [138]. When δ is swept, the positions of the maxima of emission follow a bistable curve similar to those observed in optics [139].

5.7.2. Hyper-Raman transitions

In usual probe transmission spectra, the vibrational resonances are located near $\delta \simeq \Omega_v$. However, with an intense probe other resonances originating from nonlinear resonances [111] and located near Ω_v/n with $n=2, 3, \dots$ can also be found. A probe transmission spectrum obtained with a probe beam having an intensity comparable to that of the lattice beams is shown

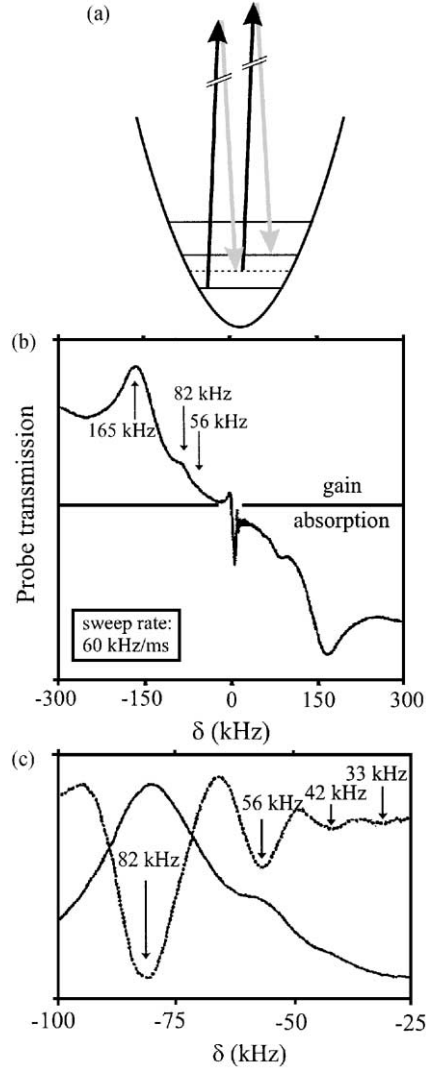


Fig. 32. (a) Hyper Raman transition involving two probe (gray arrows) and two lattice photons (black arrows). (b) Probe transmission in a 3D Rubidium lattice with a probe having an intensity comparable to that of the lattice beam. The Raman vibrational resonance is found for $|\delta| \simeq 165$ kHz, and additional resonances occur for $|\delta| \simeq 82$ kHz. (c) The dotted line is the second derivative of the probe transmission spectrum shown in solid line (this corresponds to the fraction of the spectrum shown in (b) between $\delta = -100$ and -25 kHz). From Hemmerich et al. [140], reproduced by permission of the authors.

in Fig. 32b [140]. A resonance located around $\delta \simeq \Omega_v/2$ is observed. Although this subharmonic resonances can be interpreted classically (see Section 4.3.2), a quantum picture (Fig. 32a) showing how photons are exchanged between the beams and the atom gives a particularly clear physical picture of the process. Note that a careful examination of the shape of the transmission spectrum shows also the occurrence of other subharmonics Ω_v/n with $n=3,4,5$. (This is done by calculating the second derivative of the spectrum, see Fig. 32c.)

6. Temperature, fluorescence and imaging methods

This section presents the information that can be deduced from fluorescence or imaging techniques. We start with the description of temperature measurements (Section 6.1) because the time-of-flight method which is commonly used involves the study of the fluorescence of atoms released from the lattice and crossing a probe beam. We then proceed with the description of the emission spectrum in the lattice itself (Section 6.2) and we finish with spatial diffusion which can be reliably measured using fluorescent light by taking pictures of the expanding cloud of atoms (Section 6.3).

6.1. Temperature

The linear dependence of temperature with light-shift is one of the most robust results concerning optical lattices. It was demonstrated both in the jumping regime and in the oscillating regime (Section 3.2). In fact, this variation was first observed experimentally by Lett et al. [6,141] using a time-of-flight method, a technique which is now widely used to study kinetic temperature of cold atoms.

6.1.1. Time-of-flight

In the time-of-flight method (see Fig. 33a), the atoms cooled in the optical lattice are released when the lattice beams are suddenly switched off. Because of gravity, the atoms fall towards a probe beam located a few centimeters below the intersection of the lattice beams. As the atoms pass through the nearly resonant probe laser beam, they absorb and fluoresce light. The time variation of absorption and fluorescence is related to the initial velocity distribution of the atoms in the lattice and therefore to the kinetic temperature. If the spatial extension of the lattice and of the probe beam can be neglected (this is the case when the distance h between the lattice and the probe beam is sufficiently large), the width δt of the time-dependent absorption is related to the width δv of the velocity distribution by $\delta t = \delta v/g$. An example of time-of-flight signal is shown in Fig. 33b.

Comments: (i) The scheme described above permits to determine the velocity distribution only along the vertical direction. However, the velocity distributions along both horizontal axis can also be measured if the whole pattern of the fluorescence emitted by the atoms as they cross the probe beam is recorded by a CCD camera. Such an experiment requires a probe beam significantly broader than the atomic cloud in the horizontal plane.

(ii) Corrections due to the finite size of the atomic cloud and of the probe beam's vertical waist are usually determined independently. It is also possible to have two probe beams located at different heights h_1 and h_2 . An alternate recording of the corresponding time-of-flight signals permits to deduce these corrections [70].

(iii) The “*recoil-induced resonances*” [64,120–122] can also be used to measure the velocity distribution of cold atoms [123]. In this case, two beams of frequencies ω and $\omega + \delta$ with wavevectors \mathbf{k} and $\mathbf{k} + \mathbf{q}$ are sent onto the cloud of cold atoms once the lattice beams are extinguished. Stimulated Compton transitions with the atomic momentum changing from \mathbf{P} to

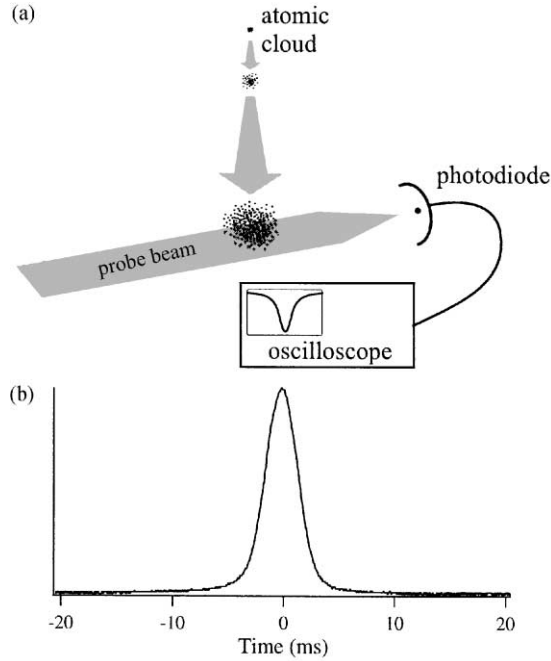


Fig. 33. Time-of-flight temperature measurement. (a) Scheme of the method. Atoms released from the lattice fall ballistically towards the probe beam. The distribution of arrival times, as measured on absorption (represented on the figure) or fluorescence, allows for the determination of atomic kinetic temperature. (b) Example of time-of-flight distribution. This recording, obtained with Cs atoms and a distance $h = 10$ cm between the lattice and the probe beam, corresponds to a temperature $T = 1.5$ μ K. From Triché [118].

$\mathbf{P} - \hbar \mathbf{q}$ are possible provided that energy is conserved, i.e. for

$$\delta = \frac{\mathbf{q} \cdot \mathbf{P}}{M} - \frac{\hbar q^2}{2M}. \quad (120)$$

The transition amplitude scales as $[\pi(\mathbf{P}) - \pi(\mathbf{P} - \hbar \mathbf{q})]$ where $\pi(\mathbf{P})$ is the atomic momentum distribution. In the limit where $q \ll P/\hbar$, this term is equal to $\hbar \mathbf{q} \cdot \nabla_{\mathbf{P}} \pi(\mathbf{P})$. The transition amplitude is thus proportional to the derivative of the momentum distribution along \mathbf{q} [120]. The total distribution along this direction is found by sweeping δ . With several directions for \mathbf{q} , the distribution in the whole momentum space can be recovered. The identity between predictions of the recoil-induced resonances and the time-of-flight method was experimentally demonstrated by Meacher et al. [123].

(iv) The relative intensities of the vibrational lines of the fluorescence spectrum are also connected to temperature. This will be discussed in Section 6.2.

6.1.2. Experimental results

All measurements performed showed that temperature increases linearly with the lattice beams intensity, apart from the range of very small intensities where a “decrochage” is observed. This includes experiments on 1D lattices [108], on 3D four-beam $\text{lin} \perp \text{lin}$ lattices [89,108], on

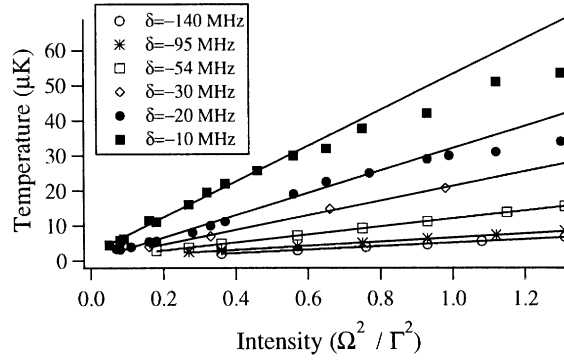


Fig. 34. Temperature as a function of intensity in a 3D six-beam molasses for various detunings. From Salomon et al. [87].

3D four-beam Rot[lin \perp lin] lattices [89], on six-beam molasses and lattices [141,142,87,143], on quasiperiodic lattices [38], on Talbot lattices [46], on grey molasses and antidot lattices [70,71]. We show in Fig. 34 an example of results obtained with a 3D cesium molasses. The linear dependence with $1/|\Delta|$ is also generally observed, although the range of variation of Δ is often reduced by the presence of neighboring transitions. For example, in the case of Cs, the $6S_{1/2}(F=4) \rightarrow 6P_{3/2}(F'=5)$ transition is located at a distance on the order of 50Γ ($\Gamma/2\pi = 5.2$ MHz) from the $6S_{1/2}(F=4) \rightarrow 6P_{3/2}(F'=4)$ transition. The approximation of a well-isolated transition thus breaks down when $|\Delta|$ becomes larger than 25Γ .

In these experiments the lowest temperature is on the order of a few recoil energies, as expected (see Section 3.2.3). For instance, cesium atoms were cooled to about $1.2\mu\text{K}$ (i.e. $6T_R$) in a four-beam lin \perp lin bright lattice. Furthermore, by turning down the intensity of the lattice beams the adiabatic expansion permits a further cooling to $0.7\mu\text{K}$ [144]. In the case of a four-beam grey molasses, cesium atoms were cooled to about $0.8\mu\text{K}$ [70].

Comments: (i) For the lowest temperature values, the width of the velocity distribution slightly overestimates the temperature inside the lattice. This is because the lowest eigenstate of the lattice Hamiltonian has a non-zero spread in momentum space.

(ii) In some circumstances, it is possible to define a spin temperature in the lattice [145]. This temperature generally differs from the kinetic temperature (see Section 9.1).

(iii) In a 3D lattice, the temperature can be anisotropic. For instance, in the Talbot lattice the temperatures in the longitudinal and in the transverse directions are significantly different [46].

(iv) In a quasi-periodic lattice (see Section 2.4), the optical potentials depend on the relative phases of the laser beams. However Guidoni et al. [38] did not observe any significant variation of the temperature with these phases. The temperature was found to be a function of I and Δ only. This is because all the potentials generated by phase variations in their experiment were topologically equivalent.

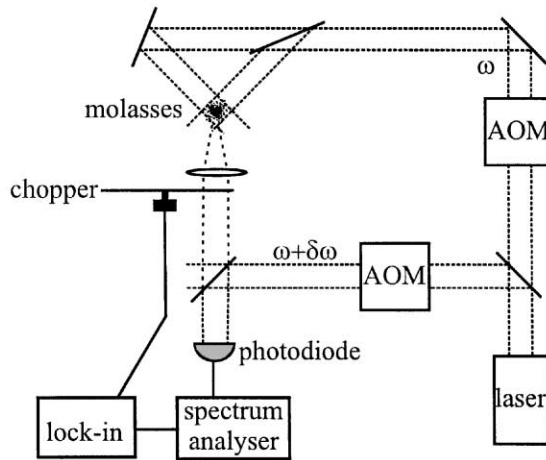


Fig. 35. Experimental scheme to observe the spectrum of light emitted in optical lattices and molasses. AOM denotes acousto-optic modulator.

6.2. Fluorescence

Many experiments on laser-cooled atoms use a scheme that either destroys the atomic cloud (time-of-flight for instance) or at least induces some perturbation (probe transmission for instance). It is however possible to collect a significant amount of information by simply observing the fluorescence spectrum of the light emitted by the atoms in the lattice. This light originates from the scattering of the lattice beams by the cooled atoms. In fact, the same information can often be found by probe transmission spectroscopy and by fluorescence spectra. Vibration and propagating excitations were for example studied by these two techniques and the use of one method or the other is often merely a question of convenience.

The starting point of these studies was the observation by Westbrook et al. [7] of a narrow resonance in the fluorescence spectrum of atoms cooled in 3D six-beam molasses. This resonance was interpreted by the Dicke narrowing of light emitted by atoms confined in a well having a dimension smaller than the wavelength [8]. This experiment used a heterodyne detection method presented in Section 6.2.1 and also employed in the following experiments on 1D and 3D lattices. Examples of information deduced from these spectra are presented in Section 6.2.2. We describe in the following section (Section 6.2.3) photon correlation spectroscopy and in Section 6.2.4 experiments where information on atomic dynamics can be deduced from time-resolved fluorescence when the optical potential is changed.

6.2.1. Heterodyne detection of the fluorescence spectrum

In this method, light emitted by atoms in an optical lattice is combined on a beam splitter with a strong local oscillator beam derived (with a frequency offset) from the same laser as the one creating the lattice (see Fig. 35). Any frequency fluctuations due to technical noise in the laser thus cancel in the beat note and a frequency resolution in the kHz range can be achieved [7]. It should be emphasized that the natural width of the excited state does not play any role in

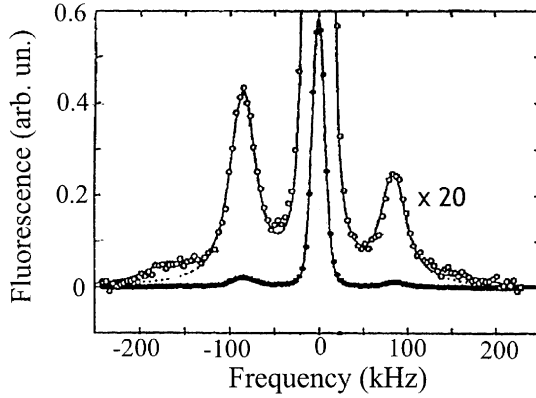


Fig. 36. Heterodyne detection of the emission spectrum of rubidium atoms in a 1D lin \perp lin lattice. From Jessen et al. [3], reproduced by permission of the authors.

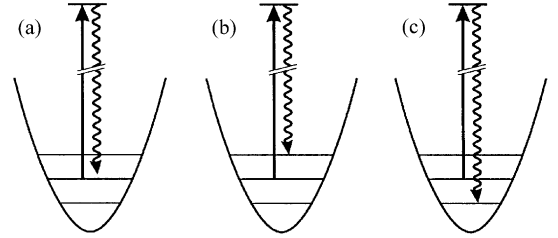


Fig. 37. Quantum description of the physical processes leading to the different components of an emission spectrum: (a) Rayleigh line, (b) Raman Stokes transition, (c) Raman anti-Stokes transition.

the linewidth because these measurements concern Rayleigh scattering which is perfectly elastic for a stationary two-level atom [10].

The frequency shift of the local oscillator with respect to the lattice beams should be large enough so that the Rayleigh line and its possible sidebands are located far away from the zero frequency. This is useful both for improving the signal-to-noise ratio and for discriminating the Stokes and anti-Stokes sidebands of the Rayleigh line which can have different magnitudes.

6.2.2. The Rayleigh line and its vibrational sidebands

An example of emission spectrum obtained from rubidium atoms (^{85}Rb) trapped in a 1D optical lattice is shown in Fig. 36 [3]. The spectrum mainly consists of a central peak at the frequency of the lattice beams (elastic scattering) and two much smaller sidebands at about 85 kHz, which roughly corresponds to the vibration frequency Ω_v of atoms trapped in a potential well.

Quantum mechanically, the central Rayleigh line is associated with a scattering process where the initial and final vibrational levels are identical (Fig. 37a). The Stokes sideband corresponds to a process beginning on a given vibrational level and returning to the next higher level (Fig. 37b). The anti-Stokes sideband originates from processes returning to the next lower level (Fig. 37c). A careful examination of Fig. 36 shows the occurrence of still smaller sidebands where the vibrational quantum number changes by two units.

The smallness of the sidebands reflects the smallness of the matrix element of the transition operator connecting two different vibrational levels (see Section 3.2.5). More precisely, the intensity of the first sideband is smaller than the intensity of the Rayleigh peak by a factor on the order of $(2\bar{n} + 1)E_R/\hbar\Omega_v$ where \bar{n} is the average vibrational number and $E_R/\hbar\Omega_v$ is the Lamb–Dicke factor [72]. Thus the sidebands are all the smaller (with respect to the Rayleigh line) as the atoms are well localized in the potential well [8,80–82].

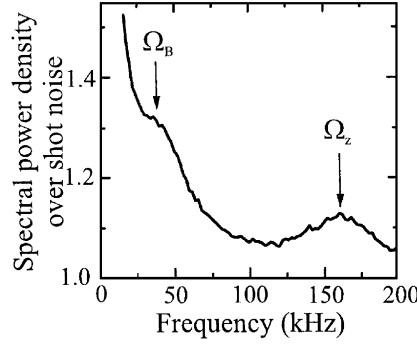


Fig. 38. Self-beating spectrum of rubidium atoms in a 3D lin \perp lin lattice, exhibiting the vibrational resonance Ω_z in the z direction and the Brillouin resonance Ω_B (see Section 5.4). Detection is performed along O_z . From Jurczak et al. [147], reproduced by permission of the authors.

An important feature that distinguishes the emission spectrum (Fig. 36) from a probe transmission spectrum (Fig. 22) is the difference of magnitude between the Stokes and anti-Stokes sidebands in emission spectra. This originates from the fact that the red sideband comes from lower vibrational levels which are more populated than the higher ones. In the harmonic approximation, the intensity of the Stokes sideband is proportional to $\pi(0)|S_{01}|^2 + \pi(1)|S_{12}|^2 + \dots$ where $\pi(n)$ is the population of the vibrational level n and S_{pn} is the transition amplitude between levels p and n . Conversely, the intensity of the anti-Stokes line is proportional to $\pi(1)|S_{10}|^2 + \pi(2)|S_{21}|^2 + \dots$. For a thermal distribution, $\pi(n)/\pi(n-1) = \exp -(\hbar\Omega_v/k_B T)$ and therefore, the ratio of the sideband strengths is given by the Boltzmann factor $\exp -(\hbar\Omega_v/k_B T)$. This provides an independent estimation of the temperature of the atoms in the lattice. This value is in reasonable agreement with theoretical predictions (Section 3.2) and with time-of-flight experiments (Section 6.1).

Comments: (i) Many effects described in Section 5 for probe transmission are also found on the fluorescence spectrum. For example, different emission spectra are found along the x - and z -axis of a 3D lin \perp lin lattice because the stiffness of the potential is different in these two directions [108]. The sideband is also located at a frequency smaller than the value predicted by the harmonic approximation because of the anharmonicity of the optical potential.

(ii) The Rayleigh peak of the emission spectrum is theoretically the sum of an elastic contribution (a Dirac δ function) and of an inelastic contribution having the same width as the stimulated Rayleigh resonance (Sections 5.5 and 5.6). Note that this inelastic contribution generally originates from several relaxation modes having different damping times.

(iii) If the local oscillator is removed from the experimental scheme (Fig. 35), a self-beating signal is observed [146]. Vibrational resonances can then be detected as shown in Fig. 38 [147]. However, the asymmetry between the sidebands of Fig. 36 is lost in Fig. 38. A careful comparison of the relative advantages of heterodyne and self-beating spectroscopy is presented by Westbrook [148].

6.2.3. Photon correlation spectroscopy

Instead of using a single detector for fluorescence, it is possible to study correlations between two spatially separated detectors observing the same optical lattice. It is also possible to study correlations between two detectors looking in the same direction but detecting cross-polarized photons. To illustrate the possibilities of this approach, let us consider a single atom in a $\text{lin} \perp \text{lin}$ lattice. When the atom is bounded in a σ^+ well, it scatters mainly σ^+ photons. When it hops into a σ^- well, the scattered light changes polarization. Thus the time scale over which polarization remains correlated should be related to the time spent in a given well.

The photon correlation method was used to study spatial diffusion [97] and spontaneous Brillouin scattering associated with the propagating excitation presented in Section 5.4 [147].

6.2.4. Time resolved fluorescence

In steady state, atomic density and magnetization match the local polarization and intensity of the lattice field. When this field is changed in a time scale short compared to the atomic response time, there is a shift between the atomic and the light patterns which yields a modification of the total fluorescence. This phenomenon is the spontaneous analog to the photon redistribution between the lattice beams (see Section 5.6.2). Consider for instance the 1D $\text{lin} \perp \text{lin}$ lattice (Fig. 10) and assume that a sudden phase-shift of the incident beam translates the bipotential by $\lambda/4$. Because atoms located at a σ^+ site are in the $m_g = -1/2$ state immediately after the translation, the fluorescence suddenly decreases because of smaller Clebsch–Gordan coefficients (see Fig. 11 for the case of the $J_g = 1/2 \rightarrow J_e = 3/2$ transition). Then the fluorescence returns to its steady-state value with a temporal behaviour depending on the eigenvalues of the dynamical modes of the optical lattice. If the translation is smaller than $\lambda/8$, fluorescence should exhibit a variation associated with the damped oscillation of atoms in a potential well.

Instead of translating the potential, one can modify its depth by changing the beams intensity or detuning [132]. If the potential depth is suddenly changed from U_0 to a new value U'_0 , the initial wave packet is projected unaltered into the new potential and undergoes damped oscillations in a breathing mode around the potential minima. Calling Ω'_v the oscillation frequency in the harmonic approximation, the period is only π/Ω'_v because of the symmetry of the wave packet. Indeed, after this time interval the atoms initially located on the right-hand side of the potential minimum occupy the symmetric position on the left-hand side of the potential minimum. The atoms initially on the left-hand side being conversely on the right-hand side, the initial wave packet is recovered, provided that damping processes can be neglected during π/Ω'_v . This effect was observed by Rudy et al. [132] in a 3D optical lattice filled with sodium atoms (see Fig. 39).

6.3. Spatial diffusion

The problem of atomic transport in optical lattices is both very difficult and particularly important to understand the atomic dynamics in this kind of structure. Depending on the depth of the optical potential and thus on the cooling efficiency, one can distinguish three regimes: if the potential is deep enough, the motion of the atoms is diffusive, which corresponds to $d\langle X^2 \rangle / dt = 2D_x$, D_x being the spatial diffusion coefficient along the x direction. At the opposite

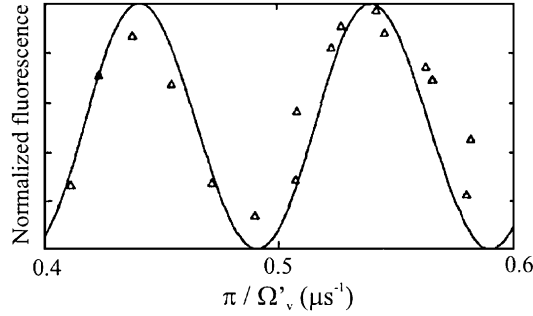


Fig. 39. Normalized fluorescence of sodium atoms in a 3D lattice after a sudden change of the potential depth. Fluorescence is detected at a fixed time ($2.6 \mu\text{s}$) after the potential change and the data are plotted versus the expected period π/Ω'_v . Each experimental result (triangles) thus corresponds to a different potential depth. The solid curve is the expected result. From Rudy et al. [132], reproduced by permission of the authors.

limit, the atoms are nearly free and their motion is ballistic, $\langle X^2 \rangle$ increasing quadratically with t . Between these two situations, one finds a regime corresponding to anomalous diffusion, where few atoms undergoing Lévy walks provide the main contribution to the evolution of the spatial distribution.

The simplest theoretical model describing spatial diffusion uses standard results of Brownian motion in the linear regime, i.e. with a friction force linear in velocity and a uniform momentum diffusion coefficient (see Section 3.2.2, comment (iii)). The validity condition for such a simple model is that the average displacement of an atom during one optical pumping time is small compared to the characteristic length of the potential (i.e. $\bar{v}/\Gamma_p \ll \lambda$); using Eq. (62), one gets

$$\left| \frac{\Delta}{\Gamma} \right| \ll \zeta \sqrt{\frac{\hbar \Delta'_0}{E_R}}, \quad (121)$$

where ζ is a numerical coefficient depending on the geometry and the atomic transition. In fact, as soon as $\Delta'_0 \gg E_R$, Eq. (121) corresponds to the condition for the jumping regime. Outside this regime, an extension of the Brownian model can still be used, starting with more realistic expressions for the friction force and the momentum coefficient [62,65]. This leads to predictions in reasonable agreement with the experimental results for deep enough potential wells. However, quantitative predictions require a complete treatment taking into account both the contribution of atoms with energies far above the potential wells and the contribution of localized atoms [63]. We describe in Section 6.3.1 the experiments studying Gaussian spatial diffusion and in Section 6.3.2 the experimental results obtained about anomalous diffusion.

6.3.1. Gaussian diffusion

Historically, the first estimates of spatial diffusion coefficients D_{sp} of atoms in optical molasses were deduced from the molasses lifetime [9,141]. Unfortunately, it appeared that the values obtained were up to 2 orders of magnitude larger than those predicted by simple theoretical models. The reason for this discrepancy is probably that the main loss mechanism is background collisions rather than atomic diffusion.

A more relevant experimental method was thus developed to study spatial diffusion of atoms in optical molasses [62]. It consists of taking a series of pictures of an atomic cloud expanding inside the spatial domain delimited by the molasses beams. A careful analysis of these images then allows to measure the size $\sqrt{\langle X^2 \rangle}$ of the cloud as a function of time and, after checking that the square $\langle X^2 \rangle$ of this size evolved linearly with time, to calculate the spatial diffusion coefficient

$$D_x = \frac{1}{2} \frac{d\langle X^2 \rangle}{dt} . \quad (122)$$

The most extensive study of this kind was performed on rubidium atoms with a 3D beam configuration consisting of three pairs of cross-polarized counter-propagating beams along the three directions Ox, Oy and Oz [62]. Strictly speaking, this configuration leads to a molasses rather than a lattice, because the potential topography changes with the relative phases of the beams (see Section 2.5.2). It is however interesting to describe the results obtained as they are similar to what is expected in an optical lattice. First, the diffusion coefficient D_x is found to be on the order of a few $100\hbar/M$, which is in good agreement with theoretical predictions. Second, in the limit of deep potential wells D_x increases linearly with the field intensity (the points of largest light-shift in Fig. 40 correspond to a small $|\Delta|$). Third, D_x reaches a minimum for a given value of the light-shift Δ'_{\min} ; then it increases and finally diverges for smaller values of Δ' . Fig. 40 shows the measurements performed by Hodapp et al. for different values of the detuning Δ and of the intensity I of the laser beams, as a function of the light-shift per beam Δ'_0 .

Comments: (i) In principle, one can also measure spatial diffusion coefficients indirectly, either through photon correlation spectroscopy [97] (see Section 6.2.3) or through pump–probe spectroscopy [118] (see Section 5.5). Such a method seems much simpler and faster than the direct technique described above. Nevertheless, quantitative relations such as Eq. (118) between the width of the zero-frequency resonance on experimental spectra and the diffusion coefficient are often not verified because the validity conditions are not met [118].

(ii) With the same experimental technique, spatial diffusion was also studied in a Talbot lattice (see Section 2.5.3) filled with cesium atoms. We show in Fig. 41 the shape of an initially spherical cloud after a lattice phase of 60 ms. Spatial diffusion is much faster in the transverse directions where the spatial period of the potential is much larger than in the longitudinal direction [46].

(iii) Diffusion measurements were also performed with nonperiodic structures, namely atoms cooled in a quasiperiodic optical lattice [149] and in a speckle field [150]. These two experiments show that investigation of spatial diffusion gives a lot of information on atomic dynamics, and especially on the role of periodicity.

6.3.2. Anomalous diffusion

Both experimental results showed in Fig. 40 and theoretical predictions show a divergence of the spatial diffusion coefficient for low values of the light-shift. In the case of the 1D $\text{lin} \perp \text{lin}$ configuration and for a $J_g = 1/2 \rightarrow J_e = 3/2$ transition, this divergence occurs for $U_0 < 61.5E_R$ [63,119].

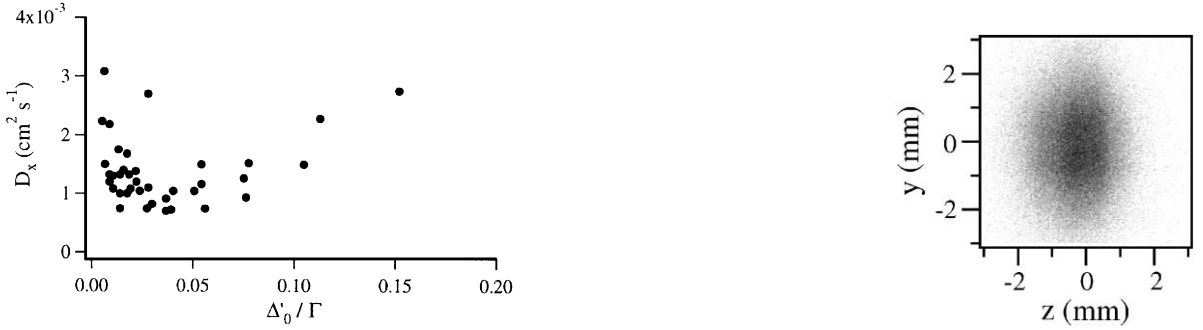


Fig. 40. Spatial diffusion coefficients D_x obtained by the measurement of the expansion of an atomic cloud in a 3D optical molasses generated by three pairs of cross-polarized counter-propagating beams. The data are plotted as a function of the light-shift per beam $|A'_0|$. For the largest values of $|A'_0|$, D_x increases linearly while it reaches a minimum for $|A'_0| \simeq 0.06\Gamma$ and increases for lower values. From Hodapp et al. [62], reproduced by permission of the authors.

Fig. 41. Pattern of the fluorescence emitted by cesium atoms in a Talbot lattice. Because spatial diffusion is slower along Oz , the shape of the cloud becomes an ellipsoid. From Mennerat-Robilliard [46].

This regime of shallow potential wells has been investigated by Katori et al. [119] with a single ion radially confined in a 2D radio-frequency quadrupole trap and cooled in a 1D $\text{lin} \perp \text{lin}$ lattice along the longitudinal direction. The position of the ion is traced through fluorescence photons. Additionally, a weak harmonic electric potential is superimposed on the optical potential, allowing for an easy relationship between the position and the potential energy of the ion.

A careful statistical analysis of the recorded ion position as a function of time shows that for shallow potential wells, some anomalous fluctuations of the ion's kinetic energy occur with long range correlations. These correlations originate from the existence of Lévy flights, i.e. periods during which the ion has enough energy to travel over many wavelengths before being trapped again.

Although quantitative comparison of the experimental results with theoretical predictions [63] is not straightforward because of the weak electric potential and of the residual micromotion of the ion in the RF trap, this experiment is a nice evidence for significant deviations from the Gaussian diffusion law.

7. Bragg scattering and four-wave mixing in optical lattices

In this section, we present additional diagnostic techniques related to Bragg scattering. We first study the basics of Bragg diffraction in optical lattices (Section 7.1). In the second paragraph (Section 7.2), we discuss the relationship between Bragg scattering and four-wave mixing in optical lattices and present some four-wave mixing experiments. The third paragraph (Section 7.3) is devoted to experiments using the dependence of the Debye–Waller factor on atomic localization to get some dynamical information on cooling and localization. In the last paragraph

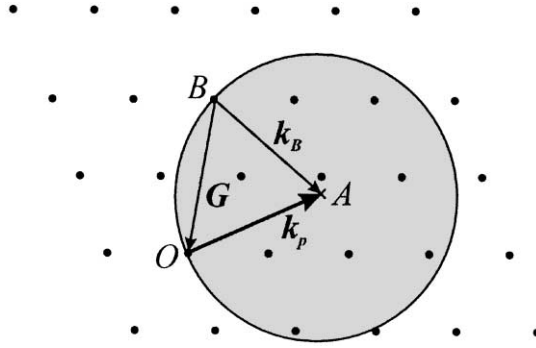


Fig. 42. Ewald construction yielding the set of Bragg diffracted wavevectors \mathbf{k}_B for a given incident probe beam \mathbf{k}_p . O being the origin of the reciprocal lattice, a sphere of radius k_p is drawn around the point A such that $\mathbf{OA} = \mathbf{k}_p$. A diffraction peak can be observed if the surface of the sphere contains a point B that belongs to the reciprocal lattice. The diffracted wave is emitted in the direction $\mathbf{BA} = \mathbf{k}_B$.

(Section 7.4), we discuss the modifications of light propagation in the optical lattice due to localized atoms.

7.1. Basics of Bragg scattering

In solid-state physics, X-ray Bragg scattering is commonly used to test long-range order in materials. Because of the structural analogy between crystals and optical lattices, it is natural to try and apply the same technique to optical lattices.

The basic idea is that a beam with an incident wavevector \mathbf{k}_p can be Bragg diffracted by a periodic structure into a beam having a wavevector \mathbf{k}_B , provided that the difference $\mathbf{k}_B - \mathbf{k}_p$ be a vector \mathbf{G} of the reciprocal lattice [29]. Considering that the reciprocal lattice is discrete and that Bragg scattering is essentially an elastic process ($|\mathbf{k}_p| = |\mathbf{k}_B|$), there is generally no wavevector matching the Bragg condition for a given incident monochromatic beam. The Ewald construction presented in Fig. 42 can be helpful to determine the set of Bragg diffracted beams for a given incident beam.

In the case of an ideal crystal where the atoms are rigidly placed at the lattice sites, the width of the Bragg peaks is diffraction limited. Taking into account the vibration of the ions around their equilibrium position, two changes occur: (i) the intensity of the Bragg peaks decreases because of the Debye–Waller factor which is associated with atomic localization (see Section 7.3), (ii) a diffuse background due to multiphonon processes appears.

This discussion can be readily transposed to optical lattices, taking into account that the typical distance between two sites is now on the order of the optical wavelength instead of one Ångström for solid crystals. Bragg diffraction of electromagnetic waves can therefore occur in the optical range instead of X-rays.

We have seen in Section 2.3.2 that for optical lattices, the reciprocal lattice is generated by the differences between the lattice beams wavevectors. This implies in particular that the Bragg condition is automatically matched for a diffraction process between two lattice beams (because $\mathbf{k}_j = \mathbf{k}_i + \mathbf{G}$ with $\mathbf{G} = \mathbf{k}_j - \mathbf{k}_i$).

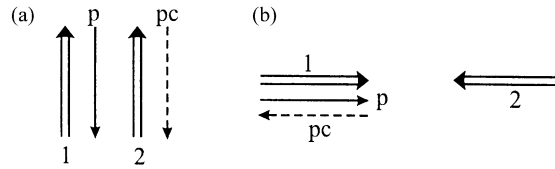


Fig. 43. Phase conjugation in an optical lattice. (a) Photon exchange in the energy diagram and (b) phase-matching condition in a 1D lattice. The lattice beams are represented by double arrows, the probe beam with a simple arrow and the conjugate beam with a dashed arrow.

Experimentally, Bragg scattering in optical lattices was demonstrated by the groups of Phillips [151] and of Hänsch [152]. Both found out that the Bragg peaks have an intensity several orders of magnitude larger than the background due to diffuse scattering, and that their angular breadth, on the order of 1 mrad, is limited by the collimation of the incident probe beam and not by the diffraction due to the finite size of the optical lattice.

Because of the frequency dependence of the scattering cross-section by the atoms, the probe beam frequency should be close to an atomic resonance to achieve a significant Bragg reflectivity. By sweeping the probe frequency around an atomic resonance, one can record a frequency spectrum of Bragg reflectivity. As expected, the spectrum exhibits a peak having a width on the order of the natural linewidth of the transition [152]. For increasing atomic densities however, the peak broadens and a dip even appears at resonance [151], accounting for the huge absorption cross-section in these conditions.

Comments: (i) A question arising when considering Bragg scattering in optical lattices concerns the low filling factor, which is generally on the order of a few percents or less in 3D lattices. One might fear that the random distribution of atoms among the lattice sites destroys the coherence of the scattering process. This is however not the case, because the empty lattice sites do not distort the potential which is imposed by the lattice beams. Contrary to the situation in solid-state physics, empty sites are not defects.

(ii) In principle, the angular width of the Bragg peak is related to the spatial extension of the illuminated sample, provided the incident probe beam is well collimated enough [153].

(iii) Bragg diffraction was also used in a quasiperiodic optical lattice (see Section 2.4) to prove the long-range quasiperiodic order in such a structure [38].

7.2. Bragg scattering and four-wave mixing

We have already mentioned in Section 2.3.2 that Bragg diffraction in optical lattices is connected to four-wave mixing processes including two lattice photons, a photon from the incident probe beam and one in the diffracted beam (see Section 2.3.2). For a deeper analysis, one can distinguish two types of four-wave mixing, namely phase conjugation-like processes and nonlinear elastic scattering (also called distributed feedback processes).

We show in Fig. 43a the energy diagram for *phase conjugation* and in Fig. 43b the corresponding phase matching geometry in the 1D case. More generally, in these processes *two* photons from the lattice beams are absorbed, a stimulated emission occurs in the probe beam and a photon is emitted in the direction \mathbf{k}_{pc} that satisfies the phase-matching condition for this

four-wave mixing process

$$\mathbf{k}_{\text{pc}} + \mathbf{k}_{\text{p}} - \mathbf{k}_1 - \mathbf{k}_2 = \mathbf{0} , \quad (123)$$

where \mathbf{k}_1 and \mathbf{k}_2 are the wavevectors of two lattice beams. Eq. (123) differs from a Bragg condition because $\mathbf{k}_1 + \mathbf{k}_2$ does not generally belong to the reciprocal lattice.

Phase conjugation in an optical lattice can also be interpreted as the scattering of a lattice beam on the atomic polarizability grating induced by the probe and a lattice beam interference pattern. It is thus clear that such a process does not constitute any evidence for the long-range order in the optical lattice [13].

Four-wave mixing spectra were recorded in a $\sigma^+ - \sigma^+$ one-dimensional lattice with a small transverse magnetic field (see Section 3.5.3). The intensity of the phase-conjugated emission exhibits a resonant enhancement when the probe beam frequency ω_{p} satisfies $\omega_{\text{p}} - \omega = 0, \pm n\Omega_{\text{v}}$ where n is an integer and Ω_{v} is the vibrational frequency [154]. These resonance conditions correspond, respectively, to the situations where the intermediate energy level in the four-wave mixing process is the initial one (degenerate four-wave mixing: $\omega_{\text{pc}} = \omega_{\text{p}}$) or that of a neighbouring vibrational level (nondegenerate four-wave mixing: $\omega_{\text{pc}} = 2\omega - \omega_{\text{p}}$). This type of four-wave mixing spectroscopy was also applied to a 3D six-beam optical lattice [155]. The spectra obtained (see Fig. 44) have a general shape similar to the ones in 1D lattices, except that the Rayleigh resonance is much narrower than the Raman vibrational sidebands. Indeed, the process which is responsible for the decay of the long-range grating induced by the pump–probe interference pattern is in this case atomic diffusion, which is very slow with respect to other relaxation processes including optical pumping. The information that can be deduced from a phase-conjugation spectrum is in fact equivalent to that found by probe transmission spectroscopy [72].

The second type of four-wave mixing process includes the absorption of only one photon in a lattice beam. A probe photon is also absorbed and there is a stimulated emission of one photon into another lattice beam. Finally, a photon is emitted into the diffracted beam. The corresponding phase-matching condition reads

$$\mathbf{k}_{\text{d}} - \mathbf{k}_{\text{p}} + \mathbf{k}_1 - \mathbf{k}_2 = \mathbf{0} . \quad (124)$$

For a given probe wavevector, the condition imposed by Eq. (124) generally corresponds to scattering directions different from those satisfying Eq. (123). By contrast, Eq. (124) coincides with a Bragg condition because $\mathbf{k}_1 - \mathbf{k}_2$ belongs to the reciprocal lattice. This four-wave mixing process was studied in the case of the 2D three-beam optical lattice [13,156] (see Section 2.3.1). In the experiment, a probe beam counter-propagating with respect to one of the lattice beams ($\mathbf{k}_{\text{p}} = -\mathbf{k}_1$) is scattered into two beams counter-propagating with respect to each of the two other lattice beams ($\mathbf{k}_{\text{d}} = -\mathbf{k}_2$ and $\mathbf{k}_{\text{d}} = -\mathbf{k}_3$). The four-wave mixing spectra obtained by sweeping ω_{p} yield some information similar to those obtained by probe transmission spectroscopy.

Fig. 45 shows how photons are exchanged in the energy diagram in this nonlinear elastic scattering. Two different processes can occur. In Fig. 45a, the sequential order of elementary steps is the following: absorption of a probe photon, stimulated emission in beam 1, absorption from beam 2, emission of a photon of wavevector \mathbf{k}_{d} . This four-wave mixing process is resonant when $\delta = 0, \pm n\Omega_{\text{v}}$ but the emitted photon has the same frequency as the probe ($\omega_{\text{d}} = \omega_{\text{p}}$). Another equivalent interpretation of this process is that the beam 2 is scattered by the atomic

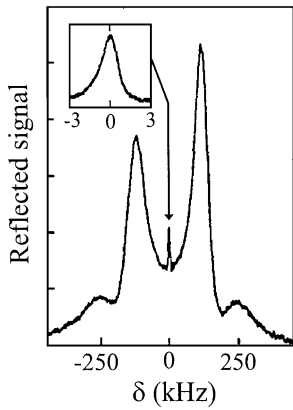


Fig. 44. Phase-conjugation spectrum for a weak probe beam directed through a cubic 3D six-beam optical lattice filled with rubidium atoms. The phase-conjugated reflectivity exhibits resonances when $\delta = \pm n\Omega_v$ and $\delta = 0$. The inset shows the central part of the spectrum with a better resolution. From Hemmerich et al. [155], reproduced by permission of the authors.

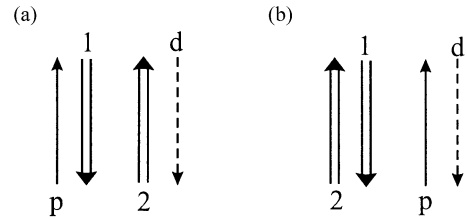


Fig. 45. Scheme of two possible four-wave mixing processes that yield nonlinear elastic scattering. The lattice (*resp.* probe) beam photons are represented by a double (*resp.* simple) arrow. The dashed arrow corresponds to the scattered wave. Only the process of (b) can be considered as Bragg diffraction in the optical lattice.

grating originating from the interference pattern created by the beam 1 and the probe beam. The emission is therefore not associated with the density modulation in the optical lattice in the absence of the probe beam. In the diagram shown in Fig. 45b, the sequential order is different. Here, the absorption in beam 2 followed by the emission in beam 1 occurs before the absorption of a probe photon and the emission of a photon with wavevector \mathbf{k}_d . This four-wave mixing process does not exhibit any resonance when δ coincides with the vibration frequency. In the classical picture, the emission results from the scattering of the probe beam off the atomic grating created by the lattice beams 1 and 2. This is therefore a Bragg diffraction process.

True Bragg diffraction can be observed if the experiment is not sensitive to four-wave mixing processes described by the diagrams of Fig. 45a. This can be done either by switching off abruptly the lattice beams before the Bragg scattering observation [151], or by resonantly enhancing the diagram of Fig. 45b with respect to the one of Fig. 45a. For instance, the choice of a probe beam frequency far enough from that of the lattice beams creates a lattice-probe interference pattern that moves too fast to imprint any grating on the atomic observables [152].

Comments: (i) Note that neither of the two experimental methods described above is able to prove unambiguously a periodic modulation of the atomic *density*. Other atomic observables can be modulated and give rise to diffraction in the same way as a density modulation. In particular, an excited state population grating or a magnetization grating can both produce Bragg scattering, even with an uniform density. Switching off the lattice beams rapidly eliminates the excited state population grating, but not the magnetization grating. This question was addressed experimentally by comparing Bragg reflectivities for different polarizations of the Bragg probe [153].

(ii) In Figs. 43 and 45, additional diagrams yielding the same physical conclusions can be drawn. For example, in Fig. 45a the following order is also possible: absorption of 2, emission of d, absorption of p, emission of 1.

7.3. The Debye–Waller factor—sensitivity to atomic localization

Let us now consider Bragg diffraction in a more quantitative way. We assume that each atom is localized at some lattice site \mathbf{R} , bound in a harmonic potential well considered as isotropic for the sake of simplicity. Note that for deeply bound vibrational levels, the harmonic approximation is excellent. A linearly polarized plane travelling wave of intensity I_p and wavelength λ_p is incident on the lattice. The amplitude A_1 scattered by a single atom is proportional to $(\pi/\lambda_p^2)\sqrt{I_p} \sin \xi |\alpha_0|$, where ξ is the angle between the incident polarization and the diffracted wavevector and α_0 is the projection of the atomic polarizability tensor on the incident polarization vector. Then the average power diffracted into the solid angle $d\sigma$ by N atoms randomly distributed among N_ℓ lattice sites is proportional to [157]

$$\frac{dP}{d\sigma} = \left(\frac{N}{N_\ell}\right)^2 |A_1|^2 \left[\beta^2 |S|^2 \left| \sum_{\mathbf{R}} e^{i\Delta\mathbf{k} \cdot \mathbf{R}} \right|^2 + N_\ell(1 - \beta^2) + \frac{N_\ell(N_\ell - N)}{N} \right]. \quad (125)$$

In this equation, the last two terms correspond to incoherent contributions coming, respectively, from the finite temperature of the lattice and from the random distribution of atoms among the lattice sites. In the following, we shall consider only the first term in the brackets of Eq. (125) associated with coherent scattering and predominant in experiments with optical lattices. In this coherent term, the sum has to be taken over all lattice sites \mathbf{R} . It averages to zero as soon as $\Delta\mathbf{k} = \mathbf{k}_B - \mathbf{k}_p$ does not satisfy the Bragg condition. The quantity $S = \sum_j \exp(i\Delta\mathbf{k} \cdot \mathbf{r}_j)$ is the structure factor of the unit cell (\mathbf{r}_j is the position of the j th atom of the basis) and $\beta = \overline{\exp(i\Delta\mathbf{k} \cdot \delta\mathbf{R})}$ is the Debye–Waller factor, where the bar represents the average over the distribution of position deviation $\delta\mathbf{R}$ with respect to the center of the potential well.

If we assume a thermal energy distribution of the atoms in the potential wells, then the position distribution is Gaussian and the Debye–Waller factor takes the well known exponential form

$$\beta = e^{-W} \quad \text{with } W = \frac{1}{2} [(\Delta k_x)^2 \overline{\delta X^2} + (\Delta k_y)^2 \overline{\delta Y^2} + (\Delta k_z)^2 \overline{\delta Z^2}]. \quad (126)$$

In view of Eq. (125), the scattered intensity appears as an accurate probe for atomic localization. Unfortunately, a direct relation between the absolute diffracted intensity and localization requires a good knowledge of the number of trapped atoms, which is difficult to measure precisely.

However, some relative measurements provide some information on the evolution of localization. Sensitivity to atomic localization was first shown independently in two experiments: in the first one, the scattered intensity was measured as a function of time after the lattice beams were switched off [151]. Because of the initial momentum distribution, the position distribution spreads as $\overline{\delta X(t)^2} = \overline{\delta X(0)^2} + \langle P_x^2 \rangle t^2 / M^2$, leading to a temporal decrease of the diffracted intensity according to a Gaussian law. The time constant of this decay is on the order of a few microseconds, in agreement with independent temperature measurements [151]. In the second

experiment [152], the lattice was created with infrared beams ($\lambda = 780 \text{ nm}$) tuned on the red side of the $5S_{1/2} \rightarrow 5P_{3/2}$ rubidium transition whereas the Bragg beam is nearly resonant on the $5S_{1/2} \rightarrow 5P_{1/2}$ transition and has therefore a completely different wavelength ($\lambda = 422 \text{ nm}$). A second probe beam at $\lambda'_p \simeq 780 \text{ nm}$ can induce stimulated Raman excitations of the vibrational motion when $\omega'_p - \omega = \pm \Omega_v$ (see Section 5.3). When this condition is fulfilled the oscillation motion of the atom is resonantly excited and $\overline{\delta X^2}$ increases. This yields a drop in the intensity of the Bragg diffracted beam (by an amount on the order of 20% [152]) because of the weaker localization.

One fundamental use of Bragg scattering in optical lattices is the dynamical study of cooling and localization [158]. Bragg scattering is indeed both extremely sensitive to localization because of the exponential form of the Debye–Waller factor, and instantaneous, contrary to pump–probe experiments for instance, which require a scanning of the probe beam frequency. Using Eq. (126), the mean-square position spread $\overline{\delta X^2_{\Delta \mathbf{k}}}$ of the atoms along $\Delta \mathbf{k}$ can be deduced from the Bragg scattered intensity $I_B(t)$ through $\overline{\delta X^2_{\Delta \mathbf{k}}} = -\ln[I_B(t)]/(\Delta K)^2 + C$, C being an additive constant which needs some further assumptions to be determined. In the harmonic approximation and for an isotropic potential, one finds $\overline{\delta X^2_{\Delta \mathbf{k}}} = K_B T / \Omega_v^2$ in the case of thermal equilibrium. The time evolution of $\overline{\delta X^2_{\Delta \mathbf{k}}}$ therefore measures the evolution of both the localization and the cooling. We show in Fig. 46 the results obtained by Phillips and coworkers [158] with cesium atoms in 1D and 3D $\text{lin} \perp \text{lin}$ optical lattices. The curves have several striking features. First, for potential wells sufficiently deep, the steady-state value reached by the mean-square position spread is independent of the lattice beams intensity and detuning, which is expected because both the kinetic temperature $k_B T$ and $\Omega_v^2 = 4E_R U_0 / \hbar^2$ are proportional to the potential depth U_0 (see Section 3.2.3). Second, the cooling rates are on the order of tens of microseconds, and for a given potential depth the evolution in 1D is around 6 times faster than in 3D. Third, an extensive study of $\overline{\delta X^2_{\Delta \mathbf{k}}}$ as a function of both intensity and detuning showed that the cooling rate is proportional only to the photon scattering rate Γ' , i.e. that whatever the conditions, an atom needs to scatter about 30 photons to be cooled in 1D and about 200 in 3D [158]. This result, which was confirmed by both semiclassical and wavefunction Monte-Carlo simulations, is unexpected in view of the theory of Sisyphus cooling, which predicts a cooling rate independent of the lattice beams intensity [4]. This suggests that the actual cooling mechanism in a realistic optical lattice is partly different from the usual theoretical description (Section 3.2). In particular, effects associated with localization could be significant.

In the same spirit, one can also use Bragg diffraction in the transient regime to study the reaction of trapped atoms to a sudden change in the potential. If one modifies the depth of the potential by a sudden change in the lattice beams intensity, the Bragg reflectivity exhibits oscillations corresponding to “breathing modes” of the atomic wave packets [159,160], i.e. oscillations of $\overline{\delta X^2_{\Delta \mathbf{k}}}$ at twice the oscillation frequency in the potential well. We show in Fig. 47 an example of such oscillations, on which different time constants appear: the fastest one corresponds to twice the atomic oscillation period, as is expected for a breathing mode (see Section 6.2.4). These oscillations decay after a few periods, both because of the anharmonicity of the potential wells and of the damping of the vibrational coherences which are excited when the potential depth changes. But one also sees a slower evolution time, on the order of 40 μs ,

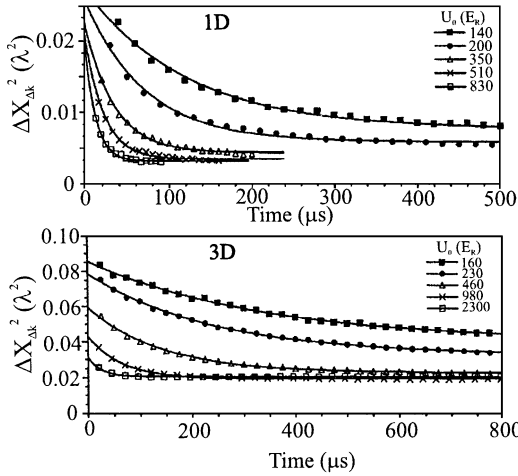


Fig. 46. Mean-square position spread deduced from Bragg scattering experiments in cesium 1D and 3D lin \perp lin optical lattices. The solid lines represent exponential fits of the experimental data with a free additive parameter. In both lattices, for deep enough potential wells, $\overline{\delta X_{\Delta k}^2}$ reaches a steady-state value independent of the parameters. From Raithel et al. [158], reproduced by permission of the authors.

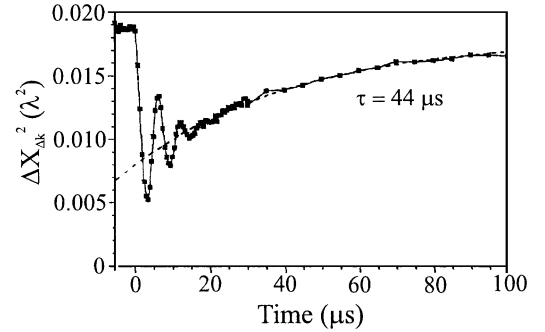


Fig. 47. Wave packet oscillations of the mean-square position spread in a 3D lin \perp lin lattice induced by a sudden increase of the potential depth from $U_0 = 850E_R$ to $U_0 = 3200E_R$ at $t = 0$ ($\Delta = -5\Gamma$). The long-term heating is best fitted with a time constant of $44\mu s$. From Raithel et al. [160], reproduced by permission of the authors.

which corresponds to a heating of the atoms towards the steady-state temperature corresponding to the new potential. Additionally, both groups (NIST and Munich) report the appearance of some structure above the noise after the oscillations decay [159,160]. Although this feature is not clear enough to be analysed quantitatively, it probably corresponds to quantum revivals, which occur if the anharmonicity-induced dephasing is faster than the damping of the coherences (a similar example of competition between dispersion and dissipation has been discussed in Section 5.6.2).

Comments: (i) To get an absolute measurement of atomic localization, one can compare the intensity scattered in two different Bragg spots [159].

(ii) Contrary to pump–probe spectroscopy which addresses all the populated vibrational levels in a potential well, the Bragg scattering technique is mainly sensitive to the lowest lying levels which correspond to the best localization. The Bragg reflectivity decreases indeed exponentially with localization. This selectivity on the low lying levels was experimentally observed in [152], where the dips in Bragg reflectivity recordings were significantly narrower than the width of vibrational resonances on the corresponding pump–probe spectra.

7.4. Backaction of the localized atoms on the lattice beams

Until now, we have considered the action of the lattice beams on the atomic dynamics. However, the Bragg condition being automatically fulfilled between two lattice beams, the lattice

waves are Bragg scattered into one another. This redistribution of the field energy induced by the atoms modifies the beams propagation and this reacts on the position of the atoms. A rigorous treatment of optical lattices thus requires a self-consistent approach, which is theoretically extremely complicated.

However, one can have a simple insight in the physical mechanisms involved by modeling a 1D optical lattice as planes of polarizable atoms of polarizability α_0 and with a planar density η , perpendicular to a standing wave (i.e. two counter-propagating travelling waves $E_0 e^{i(\pm kz - \omega t)}$ with identical polarizations) [161]. Because of the small atomic densities in optical lattices, we neglect multiple scattering and other losses. Let us now consider one atomic plane located at $z = z_0$ and calculate the amplitude to the total light field on each side of the plane [161]. The one-dimensional propagation equation in the vicinity of $z = z_0$ is

$$\left[\partial_z^2 + \frac{\omega^2}{c^2} \right] E = - \frac{\omega^2}{\epsilon_0 c^2} \mathcal{P} = - \frac{\omega^2}{c^2} \eta \alpha_0 \delta(z - z_0) E . \quad (127)$$

The tangential electric field is continuous at the boundary:

$$E(z = z_0^-) = E(z = z_0^+) . \quad (128)$$

By contrast, the derivative of the field exhibits a jump that can be calculated from Eq. (127):

$$\partial_z E(z = z_0^-) - \partial_z E(z = z_0^+) = \frac{\omega^2}{c^2} \eta \alpha_0 E(z = z_0) . \quad (129)$$

For a bright lattice, i.e. for red-detuned laser beams, the atoms are localized in planes of maximum intensity. Let us assume that such a plane is found in $z_0 = 0$ and that the solution of the Maxwell equations is

$$\mathbf{E}_{\text{left}} = 2\mathbf{E}_0 \cos(kz - \phi) \cos \omega t , \quad (130)$$

$$\mathbf{E}_{\text{right}} = 2\mathbf{E}_0 \cos(kz + \phi) \cos \omega t , \quad (131)$$

where \mathbf{E}_{left} and $\mathbf{E}_{\text{right}}$, respectively, correspond to the field in the $-\lambda_{\text{latt}} < z < 0$ and $0 < z < \lambda_{\text{latt}}$ regions (λ_{latt} is the spatial periodicity of the optical lattice). This field is obviously a solution of Eq. (127) outside $z = 0$ with $k = \omega/c$. It is also continuous in $z = 0$. Finally, we deduce from Eq. (129) that $\tan \phi = (k/2\eta)\alpha_0$. This procedure can be repeated at each antinode where the atoms are localized.

From Eqs. (130) and (131), it obviously appears that the distance between nodes and antinodes is reduced by comparison to the vacuum case. More precisely, the first node for $z > 0$, corresponding to $z = \lambda_{\text{latt}}/2$, is found when $kz + \phi = \pi/2$. This equation directly yields

$$\lambda_{\text{latt}} = \frac{\lambda}{2} \left(1 - \frac{2\phi}{\pi} \right) . \quad (132)$$

This spatial periodicity can be compared with that found in a dilute disordered gas with the same mean density $N = 2\eta/\lambda_{\text{latt}} \simeq k\eta/\pi$. The refractive index is $n_{\text{random}} = 1 + n\alpha_0/2 \simeq 1 + \phi\pi$. The wavelength λ_{random} inside this gas is therefore $\lambda_{\text{random}} = \lambda(1 - \phi/\pi)$. The distance between two antinodes is $\lambda_{\text{random}}/2$. The comparison with Eq. (132) shows that the periodic arrangement of the atoms induces an effect twice larger through coherent interference effects.

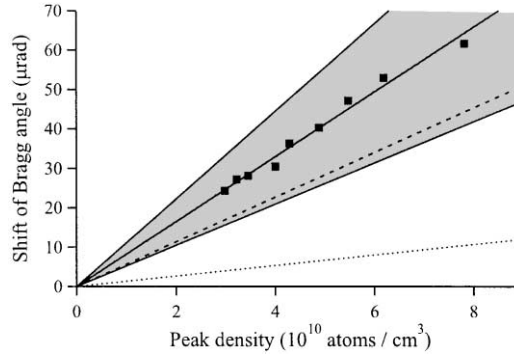


Fig. 48. Shift of the Bragg angle as a function of density. The shaded area represents the experimental confidence interval. The dotted line corresponds to the expected value without localization, and the dashed line represents the calculated value with the actual atomic localization. From Weidemüller et al. [153], reproduced by permission of the authors.

The situation for a blue-detuned lattice is quite different. The atoms are indeed localized at points of minimum intensity. A solution of the Maxwell equations of the form $\mathbf{E}_{\text{left}} = \mathbf{E}_{\text{right}} = 2\mathbf{E}_0 \cos kz$ fulfils the boundary conditions (128) and (129) in a plane such as $z = \lambda/4$ where the atoms should be found. The lattice spatial period thus remains equal to $\lambda/2$.

One can understand the difference between red and blue detuned lattices with simple arguments: compared to a randomly distributed medium, the interaction of the atoms with light is suppressed for blue detuned lattices because the atoms are localized at nodes of the field, while it is enhanced for bright lattices where the atoms are localized at the antinodes of the field.

For a realistic 3D optical lattice, more complicated models have to be developed, taking into account Bragg scattering of all lattice beams into one another [153]. Experimentally, the change of lattice constant can be detected through the change in the Bragg angle θ between the incident and diffracted beams, because the Bragg condition can be written $2d \cos \theta = \lambda_B$ where d is a spatial period of the lattice [29]. A contraction $\Delta d \sim 10^{-4}d$ was indeed observed in red-detuned optical lattices for high enough atomic densities [151,153]. We show in Fig. 48 the shift of Bragg angle as a function of the atomic density, for constant lattice parameters [153]. The shaded area represents the experimental uncertainties due to the error in determining the density and also to the error in the calibration of the Bragg angle. The dotted line corresponds to the expected value for a disordered atomic distribution and the dashed line, to the value calculated with atomic localization. One sees clearly the effect of localization on the lattice contraction.

Coherent scattering of light by the atoms localized in an optical potential can also lead to photonic bandgaps, similarly to the electronic bandgaps that are studied in solid crystals as a result of spatial periodicity [161]. From an optical point of view, photonic bandgaps arise from interferences between different Bragg diffracted beams that strongly enhance reflection and suppress propagation of light inside the optical lattice.

The engineering of materials with three-dimensional bandgaps (which means that in a given frequency range no light propagates in the material whatever the direction) is a very active

field of research. Such an effect requires that there is a strong Bragg scattering in all directions. As far as optical lattices are concerned, their filling factor is very small, and the atomic scattering cross-section is reasonably large only at resonance, so that optical lattices cannot contain multi-dimensional bandgaps. Nevertheless, a method using an interference pattern to engineer a 3D photonic crystal has been demonstrated recently [12]. This technique consists of illuminating a photoresist with the 3D interference pattern originating from 4 noncoplanar laser beams, and then dissolving the nonilluminated parts. The obtained structure is periodically modulated in three dimensions and can be used as a template for materials with a higher index of refraction.

8. Atomic interactions in optical lattices

This section deals with the atom–atom interactions in a dissipative optical lattice. We first discuss the different types of light-induced interactions that may occur (Section 8.1), and then we study the consequences of atomic localization on collisional rates (Section 8.2).

8.1. Light-induced interactions in optical lattices

Most of the time, the atomic dynamics in dissipative optical lattices can be described without taking into account any interaction between the atoms. The filling factor in these structures is indeed very low (on the order of the percent in 3D lattices), which means that the mean distance between two trapped atoms is on the order of a few microns. However, a theoretical study of long range molecular interactions shows that the interaction energy of two atoms in nearby potential wells of a dissipative optical lattice is not negligible with respect to the potential depth for one atom [162]. For example, for a 1D optical lattice generated by two counter-propagating waves with parallel linear polarizations, the interaction is attractive and for two atoms in adjacent wells, the interaction energy can be as large as $1/6$ of the potential depth. The molecular interaction energy of two atoms in the same potential well of a dissipative optical lattice is about twice the depth of the potential well, which forbids to put more than a single atom in one well [162].

Other kinds of light-induced interactions, such as multiple photon scattering, are possible in principle, but cannot be identified in practice because of the low densities achieved in near-resonant lattices.

Comments: (i) Note however that the situation is very different in far-off resonant lattices, where no spontaneous emission occurs and where molecular interactions are much smaller (they scale as $1/\Delta$ [162]): the densities achieved in these systems can reach one atom per well [79,163] and Bose–Einstein condensation might even be possible.

(ii) In optical molasses, the phase-space density is intrinsically limited by light reabsorption [164–167]. This is probably the case also for near-resonant bright optical lattices, although the localization of atoms in potential wells makes the situation different.

(iii) It is possible to have a spatial period much larger than λ in an optical lattice. This is for instance the case in a four-beam lattice with small angles θ_x and θ_y (Section 3.3.4). In

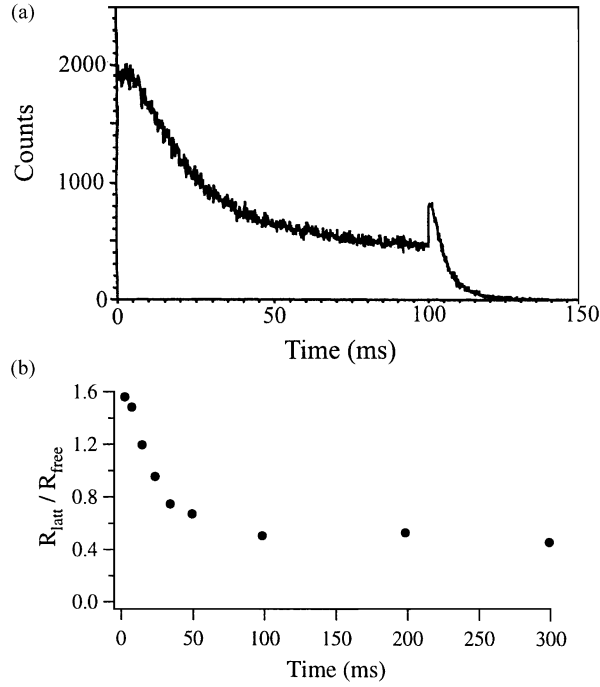


Fig. 49. (a) Penning ionization detected during the lattice phase and afterwards, averaged over 50 cycles. (b) Comparison of collision rate in the lattice to that for free atoms as a function of time. The detuning is $\Delta = -4800\Gamma$ and the intensity is $I = 5 \text{ W/cm}^2$ per beam. From Lawall et al. [169], reproduced by permission of the authors.

this situation, two atoms in the same well can be sufficiently far away so that their interaction remains smaller than the potential depth.

8.2. Study of collisions

In optical lattices, the atoms are strongly localized ($\overline{\delta X} \sim 0.1\lambda$) around the bottom of the potential wells. The question of collisions then arises: does atomic localization reduce the collisional rate by isolating each atom in its own potential well, or does the optical potential channel the atoms towards the wells, making them more probable to collide with one another?

This question was addressed in two experiments performed at the University of Tokyo [168] and at NIST [169]. Both use metastable atoms and detect ionizing collisions, which are dominant [170,171]. The metastable atoms (argon, krypton or xenon) are first cooled in a magneto-optical trap and then transferred into a 3D four-beam optical lattice. After the lattice phase during which the collisional rate is recorded continuously, the lattice beams are shut off. We show in Fig. 49a a typical signal obtained with ^{132}Xe [169]: the collisional rate drops slowly because of the reduction in density due to atomic diffusion and collisions, and also because of localization inside the potential wells. Then the lattice beams are switched off at $t = 100 \text{ ms}$, and the collisional rate increases again, showing that a suppression of collisions indeed occurs in the lattice. The rapid decrease afterwards originates from the ballistic motion of the atoms once in the dark.

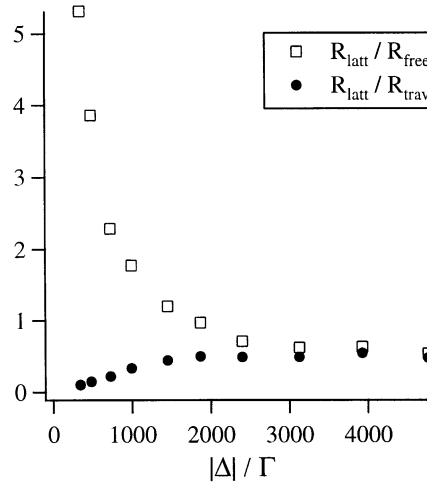


Fig. 50. Open squares: $R_{\text{latt}}/R_{\text{free}}$ versus Δ . Solid circles: $R_{\text{latt}}/R_{\text{trav}}$, where R_{trav} is the measured collision rate for atoms submitted to a travelling wave (i.e. experiencing no optical potential) having an intensity $8I$ equal to that at the bottom of the lattice wells. $I = 5 \text{ W/cm}^2$ per beam. From Lawall et al. [169], reproduced by permission of the authors.

Fig. 49b shows the ratio $R_{\text{latt}}/R_{\text{free}}$ of the collisional rate in the lattice compared to that for free atoms for a similar density (i.e. measured immediately after the lattice beams are shut off), for different lattice durations. As the lattice beams are turned on, the atoms are rapidly channelled into the potential valleys, and thus the peak density is higher than for randomly distributed atoms. Because the binary collision rate is proportional to the square of the density, a modulated density leads to a larger rate than a uniform one. Consequently, it seems that the atomic dynamics in the lattice first enhances collisions, which corresponds to values of $R_{\text{latt}}/R_{\text{free}}$ initially larger than 1 in Fig. 49b. Then $R_{\text{latt}}/R_{\text{free}}$ decreases towards an asymptotic value $R_{\text{latt}}/R_{\text{free}} \simeq 0.5$. This reflects a suppression of collisions when the thermalized atoms are localized inside potential wells [168,169]. This interpretation is supported by the fact that the temperature has the same temporal dependence as $R_{\text{latt}}/R_{\text{free}}$ [169].

Note that the ratio discussed above compares collisional rates in an optical lattice and in the *darkness*. One should however take into account the effect of the excited state population on the mean scattering cross-section, as studied for example in [172], which is not related to the lattice dynamics itself. It can thus be interesting to measure also the collisional rate for atoms in a travelling wave of intensity $8I$, which corresponds to the intensity at the bottom of the wells induced by a 3D four-beam lattice. We show in Fig. 50 both the previous ratio $R_{\text{latt}}/R_{\text{free}}$ and the ratio $R_{\text{latt}}/R_{\text{trav}}$ of collisional rates in the lattice and in the corresponding travelling wave, in steady state, as a function of lattice laser detuning [169].

As expected, for large detunings both ratios correspond, because then the excited state population is negligible. As the detuning decreases however, $R_{\text{latt}}/R_{\text{trav}}$ decreases while $R_{\text{latt}}/R_{\text{free}}$ increases and becomes larger than 1. This shows that the dominant effect for $|\Delta| \leq 2000\Gamma$ is due to resonant enhancement [172] rather than to intrinsic lattice dynamics. Therefore, the detailed analysis of the dependence of $R_{\text{latt}}/R_{\text{free}}$ on the lattice beams intensity and detuning

[168] requires some precautions and a complete theoretical treatment accounting for resonant excitation.

9. Effect of a magnetic field

9.1. Paramagnetism

We have seen in Section 3.1.3 that the optical potential resulting from the $\text{lin} \perp \text{lin}$ configuration has an antiferromagnetic structure, i.e. it exhibits potential wells with alternating σ^+ and σ^- light polarization. In the presence of a small static magnetic field \mathbf{B}_0 along Oz (small meaning here that the maximum Zeeman shift is small compared to the maximum light-shift), this property leads to a paramagnetic behaviour of the atoms in the lattice [145].

Let us consider an atom having an $F \rightarrow F' = F + 1$ transition with $F \geq 1$ in a 1D $\text{lin} \perp \text{lin}$ optical lattice. The eigenstates of light-shift are generally a superposition of several Zeeman sublevels, but at the bottom of σ^\pm potential wells they correspond to pure $|F, m_F = \pm F\rangle$ states. In the absence of any magnetic field, the σ^+ and σ^- potential wells have identical depths and pumping rates. The atoms are thus randomly distributed in the lattice sites, with equal probabilities of occupying a σ^+ or a σ^- well.

On the contrary, if a small static longitudinal magnetic field \mathbf{B}_0 is applied, the Zeeman shift is opposite for $|F, m_F = +F\rangle$ and $|F, m_F = -F\rangle$ sublevels. A typical potential obtained in this configuration is showed in Fig. 51. From statistical physics intuition, one expects the atoms to be transferred to the potential wells corresponding to the lowest energy, leading to a macroscopic magnetization of the lattice. However, atoms in an optical lattice are not coupled to a thermal bath and the occurrence of a magnetization is not obvious.

Most atoms being localized in σ^+ and σ^- wells, they mainly populate the extreme Zeeman sublevels $|F, m_F = +F\rangle$ and $|F, m_F = -F\rangle$, respectively, which have very different absorbing cross-sections for σ^+ and σ^- light: in the case of cesium, for example, the probability for an atom in the $|F=4, m_F = +4\rangle$ sublevel of absorbing a σ^- photon is 45 times smaller than that of absorbing a σ^+ photon for equal incident intensities. Consequently, for atomic transitions with large angular momenta one can consider that a weak σ^+ -polarized beam probes the atoms in σ^+ wells while a σ^- -polarized beam probes those in σ^- wells. The magnetization of the atoms can thus be deduced from the transmission of a circularly polarized probe beam through the atomic cloud [145,173].

Instead of measuring the transmission, it is possible to measure the stimulated Raman gain (or absorption) with a circularly polarized probe in the vicinity of the vibrational resonance (see Section 5.3). The gain for a σ^\pm -polarized probe is proportional to the atomic population Π_\pm in σ^\pm potential wells (provided one neglects the very weak absorption of σ^\pm light by atoms localized in σ^\mp wells). The ratio of the gains found with σ^- and σ^+ probes is then simply equal to Π_-/Π_+ . We show in Fig. 52 this population ratio as a function of the applied magnetic field. The exponential dependence on B_0 of Π_-/Π_+ reminds a thermal dependence and suggests the introduction of a phenomenological spin temperature. This temperature was found to be twice the zero-field kinetic temperature, in good agreement with numerical simulations [145,173]. This difference reflects the well known fact that laser-cooled atoms are not in thermodynamics

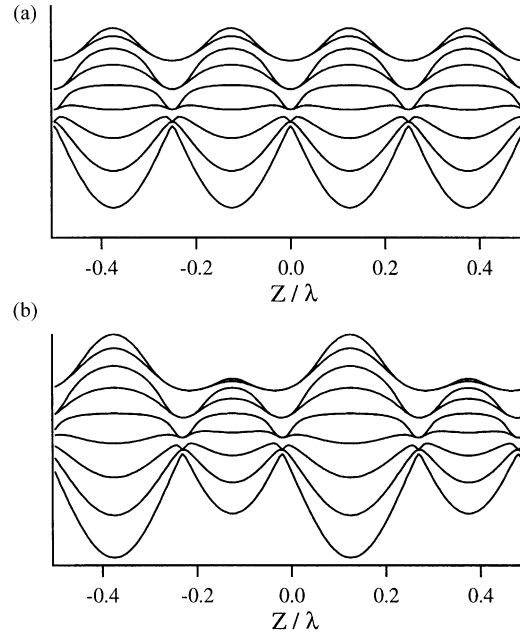


Fig. 51. Optical potential for an atom with a $F=4 \rightarrow F'=5$ transition in the 1D lin \perp lin configuration. (a) In the absence of magnetic field, the σ^+ and σ^- potential wells are identical. (b) With a small static longitudinal magnetic field \mathbf{B}_0 , these potential wells experience opposite Zeeman shifts.

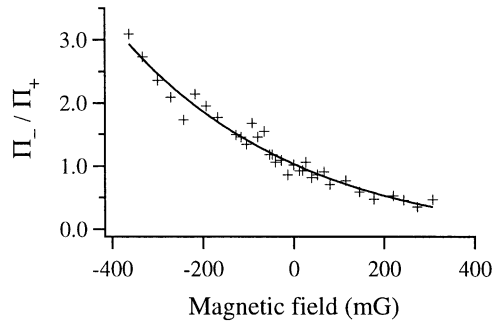


Fig. 52. Ratio Π_-/Π_+ of the population in the σ^- wells to that in the σ^+ wells, versus magnetic field B_0 . The exponential variation permits to define a phenomenological spin temperature. From Meacher et al. [145].

equilibrium. Therefore, it is not surprising that the steady state of the system cannot be described by a unique temperature.

The global magnetization of the atoms increases with the magnetic field until the Zeeman shift becomes on the same order of magnitude as the light-shift. The magnetization then decreases if \mathbf{B}_0 further increases, because then the potential curves are separated and associated to almost pure Zeeman sublevels, so that the situation resembles the $J_g = 1/2 \rightarrow J_e = 3/2$ transition (see comment below).

The dynamics of magnetization, which is strongly correlated to localization, can also yield some information on the local character of the cooling process. We have seen in Section 3.1.2 that for a $J_g = 1/2 \rightarrow J_e = 3/2$ transition, Sisyphus cooling can occur only when the atoms jump between differently polarized potential wells. On the contrary, for atomic transitions with higher angular momenta a local cooling mechanism is also possible (see Fig. 13). Measuring both the cooling time constant and the magnetization (i.e. localization) time constant can thus help determining whether local processes play an important role in the cooling dynamics of “realistic” atoms. Such a dynamical study was performed with cesium atoms by Phillips and coworkers [173]. They first localize the atoms in an optical lattice with a small magnetic field and then switch off the magnetic field and measure the transmission of a weak circularly polarized probe beam. The magnetization time constant was found to be on the order of $100 \mu\text{s}$, around 3 times longer than the cooling time constant which was measured independently by Bragg reflection (see Section 7). This shows that it is not necessary for an atom to hop from one well to a distant one to dissipate energy. It indicates that for atoms with high angular momenta, local cooling plays a significant role in the Sisyphus process efficiency.

Comments: (i) For an atom having a $J_g = 1/2 \rightarrow J_e = 3/2$ transition, no paramagnetic behaviour is expected in the $\text{lin} \perp \text{lin}$ configuration. The eigenstates of the light-shift operator are indeed the Zeeman sublevels $|J, m_J = \pm J\rangle$, which are also eigenstates of J_z . Thus neither the eigenstates nor the pumping rates are modified by the addition of a magnetic field: the only effect of \mathbf{B}_0 consists of shifting globally both potential curves in opposite directions, without affecting the atomic dynamics.

(ii) For $J \rightarrow J$ and $J \rightarrow J - 1$ transitions (see Section 9.2), a paramagnetic behaviour is also expected and observed [69,70]. The magnetization increases linearly with magnetic field for small B_0 , and then decreases towards zero for large B_0 .

9.2. Antidot lattices

In Section 2.3.4, we found that under some circumstances, an antidot lattice can be achieved with a far blue-detuned lattice beam. We show here that the optical potential of a grey molasses (see Section 3.4) in the presence of a static magnetic field generally consists of antidots rather than wells [105]. In an antidot lattice, there is no bound state and all the atoms are free. In fact, atoms undergo an erratic motion in the lattice by occasionally bouncing on the antidots in a manner similar to a ball in a pinball game [26].

Consider the situation of a 1D $\text{lin} \perp \text{lin}$ lattice (Section 3.1.1) in the presence of a static magnetic field \mathbf{B}_0 applied along the Oz axis. If the lattice beams are tuned on the blue side of a transition connecting a ground state of angular momentum F to an excited state of angular momentum F or $F - 1$, Sisyphus cooling can be achieved [85]. In fact, the cooling is most efficient for low B_0 and for high B_0 [105]. We consider this last case in the remaining of the section. The Zeeman splitting $2F\Omega_0$ between the extreme Zeeman sublevels of the ground state is assumed to be larger than the light shift Δ' . Therefore, the light-shift can be treated as a perturbation compared to the Zeeman effect and the magnetic quantum numbers can be used to label the potential surfaces. In this situation, a majority of atoms are found in the extreme Zeeman sublevels ($m_F = \pm F$ for transitions $F \rightarrow F$ and $m_F = \pm F, \pm F - 1$ for transitions $F \rightarrow F - 1$) and the cooling occurs through the mechanism shown in Fig. 53. The dependence

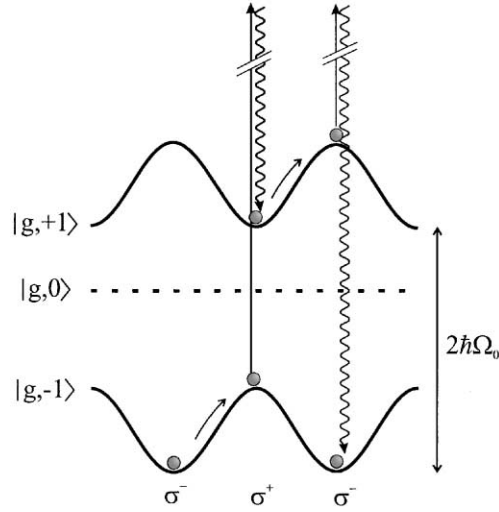


Fig. 53. Sisyphus cooling in a 1D lin \perp lin lattice with a magnetic field \mathbf{B}_0 . The potentials correspond to a blue detuning from a $F_g=1 \rightarrow F_e=1$ transition. The atom climbs a potential hill before being optically pumped into another Zeeman sublevel where it also climbs a potential hill.

of the temperature T with Δ' and Ω_0 was studied theoretically [69] and experimentally [70]. In particular, for a fixed value of Ω_0 , T is a linear function of Δ' .

In the 1D case, the potential curves resulting from the combined effect of the Zeeman shifts and of the light-shifts exhibit potential wells (Fig. 53). Note that the light-shift vanishes at the bottom of the wells associated with the extreme Zeeman sublevels. An atom localized around these points is very weakly coupled to the incident beams. In higher dimensions, the potential surfaces generally exhibit antidots rather than wells, as shown in Fig. 54a where a section in the xOy plane of the $m_F = -1$ potential surface for a $F_g=1 \rightarrow F_e=1$ transition is shown. This surface was obtained for a four-beam lin \perp lin lattice (Section 3.3.4) and a field \mathbf{B}_0 along Oz . The shape of the antidot potential suggests that most of the atoms should be located near the bottom of the valleys between the antidots, where the potential is minimum and where the optical pumping rate vanishes (these lines are associated with a pure circular polarization of the lattice field). The steady-state atomic density in the xOy plane is shown in Fig. 54b. This density is calculated using a semi-classical Monte-Carlo simulation (Section 4.3) for the $F_g=1 \rightarrow F_e=1$ transition. As expected, the density is maximum in the valleys between the antidots.

A precise examination of a single semi-classical trajectory shows that a ballistic motion over several wavelengths is a relatively seldom event. In most circumstances, the atoms diffuse in the lattice by repeatedly bouncing on the antidots as shown in Fig. 54c. Hence, the antidots act as pinball bumpers for the atoms. Because the height of the antidots is on the order of Δ' , one expects that the typical frequency for an atom bouncing back and forth between two antidots should be on the order of $\sqrt{\Delta'}$ (as for the vibration motion considered in Section 5.3). To excite these transient oscillations between antidots, a probe beam of frequency $\omega_p = \omega + \delta$

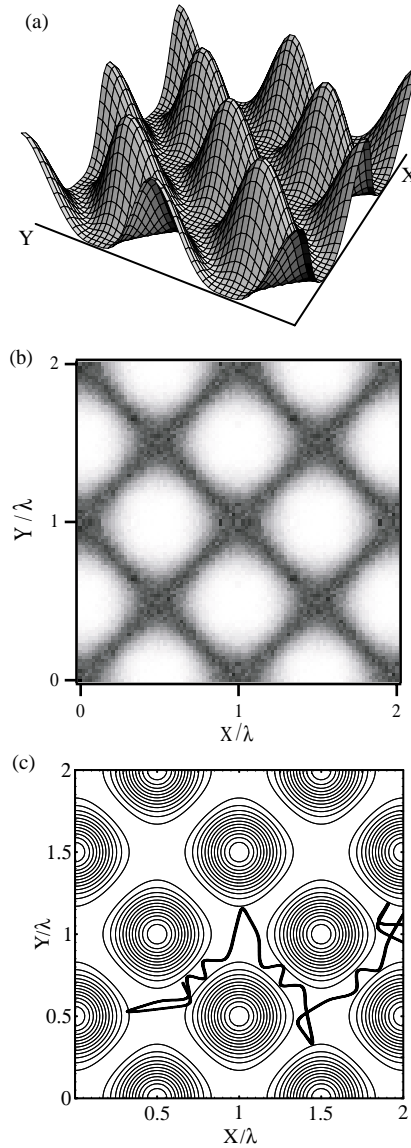


Fig. 54. Antidot optical lattice. The calculations are made in the case of a four beam $\text{lin} \perp \text{lin}$ lattice with $\theta_x = \theta_y = \theta = 30^\circ$ in the presence of a large static magnetic field applied along the Oz axis. The data correspond to the $m_F = -1$ potential surface for a $F_g = 1 \rightarrow F_e = 1$ transition. (a) Section of the potential in the xOy plane. (b) Distribution of the atomic density. The dark zones which correspond to increased density are found near the valleys of the potential. (c) Typical semi-classical trajectory showing the bouncing of an atom between antidots. From Petsas et al. [26].

can be added to shake the optical potential at frequency δ . Raman resonances characteristic of this bouncing motion are found in the probe transmission spectrum both in the experiment and in the numerical simulation. These resonances were extensively studied in [26]. They are

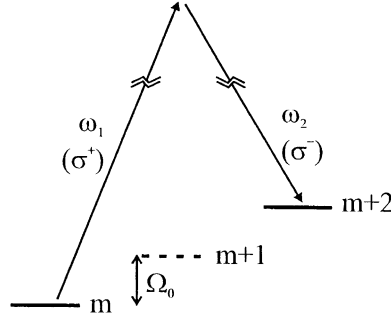


Fig. 55. Raman resonances between Zeeman sublevels in the case where the light beams have only σ^+ and σ^- components with respect to \mathbf{B}_0 . The resonance occurs for $\omega_1 - \omega_2 \simeq \pm 2\Omega_0$.

broadener than the vibrational resonances shown in Section 5.3 because of the short duration of these transient oscillations.

Comments: (i) A similar dynamical behaviour has been previously reported for electrons in 2D antidot semiconductor superlattices [174–176]. However, one main difference with the solid-state experiments is that there is not a simple parameter (such as the magnetic field for electrons) to act on the atomic motion. Some interesting developments inspired by the solid-state physics experiments can nonetheless be considered. For example, it was shown that the dynamics of electrons is different in square and in hexagonal antidot superlattices [177] because of the possible weak localization of electrons in the latter case [178,179]. An analogous study in an optical lattice has not yet been performed.

(ii) Although antidot lattices are generally encountered in the case of a 3D grey molasses with magnetic field, it is also possible to achieve a lattice exhibiting wells in some field configurations [180].

9.3. Lattice in momentum space

The localization of atoms on a lattice in the momentum space can also be found when a static magnetic field is added to a grey molasses or to a bright lattice [181,182]. The origin of this effect and the construction of the lattice in the momentum space are described in this section.

Sisyphus cooling originates from a redistribution of photons between the cooling beams (a process known as two-beam coupling or stimulated Rayleigh scattering, see Section 3.2.2). In the case of free atoms, two-beam coupling is resonant around frequencies ω_1 and ω_2 for the laser beams such as $\omega_1 - \omega_2 \simeq 0$ (Rayleigh resonance) and $\omega_1 - \omega_2 \simeq \omega_{gg'}$ where $\omega_{gg'}$ coincides with an atomic Bohr frequency (Raman resonance) [51,183]. If we consider a ground state having an angular momentum F and a Landé factor g_F , the Raman resonance (Fig. 55) occurs for $\omega_1 - \omega_2 \simeq \pm 2\Omega_0$ (with $\Omega_0 = g_F \mu_B B_0$) if all the field polarizations are perpendicular to \mathbf{B}_0 . (In the case where the light field has σ^+ , σ^- and π components with respect to \mathbf{B}_0 , the resonance condition becomes $\omega_1 - \omega_2 \simeq \pm \Omega_0$.) In most cases, experiments are performed with fields having the same frequency ω . However in the atomic frame, for an atom with a velocity \mathbf{v} , these fields are Doppler-shifted ($\omega_i = \omega - \mathbf{k}_i \cdot \mathbf{v}$ where \mathbf{k}_i is the wavevector of the beam i).

As a result, the Rayleigh and Raman two-beam couplings exhibit resonances for the velocity groups that satisfy:

$$(\mathbf{k}_i - \mathbf{k}_j) \cdot \mathbf{v} = p2\Omega_0 \quad (p = -1, 0, 1). \quad (133)$$

These conditions determine the velocity groups around which the velocity damping occurs. In the 1D case with two counter-propagating beams ($\mathbf{k}_1 = k\mathbf{e}_z, \mathbf{k}_2 = -k\mathbf{e}_z$), the bunching occurs around three velocities $v_z = -\Omega_0/k, 0, \Omega_0/k$ proportional to B_0 . This was observed by Van der Straten et al. [184,185] and Valentin et al. [186].

If the beam geometry makes use of the minimum number of beams (i.e. 4 in 3D), a periodic optical lattice with a basis $\{\mathbf{a}_1, \mathbf{a}_2, \mathbf{a}_3\}$ in the direct space is found. This basis is related to the vectors $\mathbf{a}_{j-1}^* = \mathbf{k}_1 - \mathbf{k}_j$ of the reciprocal lattice by the relations $\mathbf{a}_j^* \cdot \mathbf{a}_l = 2\pi\delta_{l,j}$ (see Eqs. (28)). The comparison between these equations and Eq. (133) shows that the velocities are located on a lattice with a basis $\mathbf{v}_l = \mathbf{a}_l\Omega_0/\pi$ with ($l = 1, 2, 3$) [181].

To have a better insight, we present the localization found in the 2D case when the cooling originates from three beams $\mathbf{k}_1, \mathbf{k}_2, \mathbf{k}_3$ (Fig. 56a). The basis of the reciprocal lattice (\mathbf{a}_1^* and \mathbf{a}_2^*) and of the direct lattice (\mathbf{a}_1 and \mathbf{a}_2) are shown in Fig. 56b. Consider for example the bunching of velocities around $\mathbf{v}_1 = \mathbf{a}_1\Omega_0/\pi$. It results from a Rayleigh two-beam coupling originating from beams 1 and 3 ($\mathbf{a}_2^* \cdot \mathbf{v}_1 = 0$) and from Raman two-beam couplings originating, respectively, from beams 1 and 2 ($\mathbf{a}_1^* \cdot \mathbf{v}_1 = 2\Omega_0$) and from beams 2 and 3 ($(\mathbf{a}_2^* - \mathbf{a}_1^*) \cdot \mathbf{v}_1 = -2\Omega_0$). The three pairs of beams thus create a 2D restoring force that pulls the nearby velocity towards \mathbf{v}_1 . There are seven velocity groups ($\mathbf{0}, \pm\mathbf{v}_1, \pm\mathbf{v}_2, \pm(\mathbf{v}_1 + \mathbf{v}_2)$) that share this property (see Fig. 56c). Actually we have plotted in Fig. 56d all the lines for which two pairs of beams create a damping force that attracts the atoms along these lines. The seven velocity groups mentioned above correspond to the intersection of these lines.

The experimental observation of this bunching in momentum space was performed by Triché et al. [181] using a 3D four-beam lin \perp lin lattice and by Rauner et al. [182] in the case of a 2D lattice. We give some details about this last experiment which is performed starting from a beam of cold metastable neon atoms prepared in a tilted magneto-optical funnel [187]. This beam is normal to the lattice plane xOy defined by two orthogonal standing waves of same frequency, linearly polarized in the plane (see Sections 2.3.3 and 3.3.3). The beams are tuned to the red side of the $3S_{3/2}(J=2) \rightarrow 3P_{5/2}(J'=3)$ transition and the magnetic field \mathbf{B}_0 has components along the three $\mathbf{e}_x, \mathbf{e}_y$ and \mathbf{e}_z axis. After travelling a distance of 24 cm from the molasses, the metastable neon atoms are detected using a microchannel plate with an adjacent phosphor screen and a CCD camera. A direct 2D image of the transverse atomic distribution is thus obtained as shown in Fig. 57a. The bunching of atoms along a few directions is clearly observed. These directions correspond to transverse velocities located on a lattice with a basis $\mathbf{v}_l = \mathbf{a}_l\Omega_0/2\pi$ (the factor $\frac{1}{2}$ with respect to the previous formula arises from the additional effect of π photons in the Raman resonance condition). Indeed, the expected pattern shown in Fig. 57b is in perfect agreement with the experiment.

In both experiments [181,182], it was also shown that the size of the basis vectors of the lattice in momentum space increases proportionally to B_0 , as expected. Note finally that this lattice can be found both in the case of a bright lattice [182] and in the case of a grey molasses (the experiment of Triché et al. was performed on the blue side of the $6S_{1/2}(F=3) \rightarrow 6P_{3/2}(F'=2)$ transition of cesium) [181].

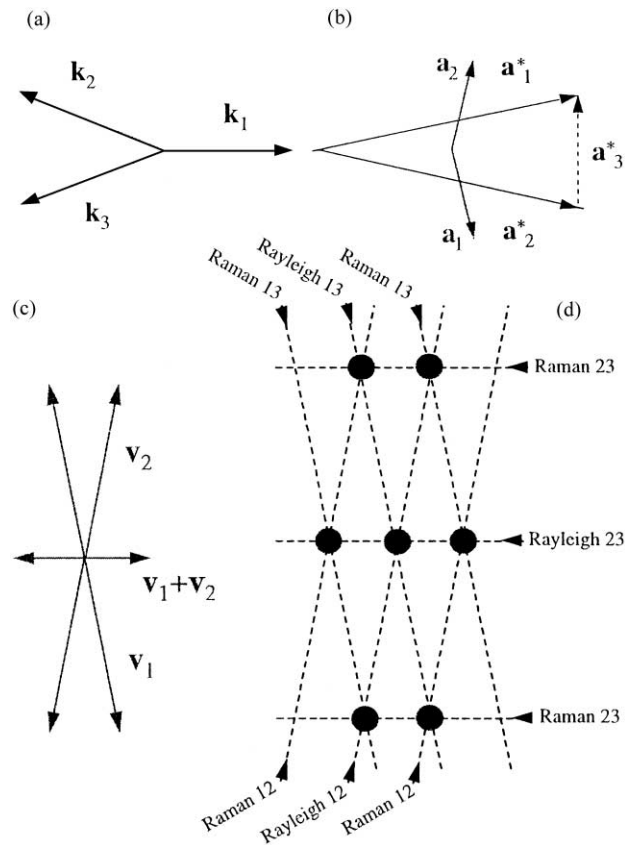


Fig. 56. Bunching of the velocities in a three-beam 2D lattice. (a) Wavevectors of the incident field. (b) Basis vectors in the reciprocal space and in the direct space. (c) Velocity groups around which bunching occurs. Note that \mathbf{v}_1 and \mathbf{v}_2 are parallel to \mathbf{a}_1 and \mathbf{a}_2 . (d) The velocity groups around which bunching occurs are found at the intersection of three lines corresponding to a Rayleigh or a Raman resonance. The splitting between the lines is proportional to B_0 .

9.4. The asymmetric optical lattice: an analogue to molecular motors

Combining light-shift and Zeeman shift, one can tailor nearly any potential shape, thus modelling very different physical situations. For example, the addition of a small static magnetic field \mathbf{B}_0 along the direction of propagation of two laser beams in the $\text{lin } \theta \text{ lin}$ configuration (see Section 3.4.2 and Fig. 58a) gives rise to a potential curve which is periodic but asymmetric (Fig. 58b). The light frequency is set a few Γ above atomic resonance, so that the internal dark state (see Section 3.4) existing for the $F = 1 \rightarrow F' = 1$ transition considered here has the lowest potential energy. This potential energy is modulated by the small magnetic field, which gives rise to the sawtooth potential of Fig. 58b.

In fact, the physical situation realized here models that of molecular motors in biological cells, which are proteins moving along protein fibers [188,189]. Proteins being polar molecules,

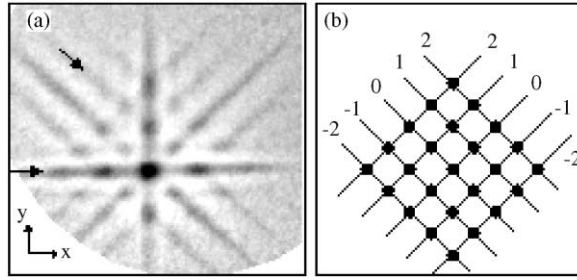


Fig. 57. Bunching of the velocities in a four-beam 2D lattice [182]. The experiment is performed with a cold and slow beam of metastable neon (frequency detuning from the $J=2 \rightarrow J'=3$ transition $\Delta = -9\Gamma$, saturation parameter $s = 2.6 \times 10^{-3}$, static field $B_0 = 0.21$ G). (a) Experimental observation of the momentum distribution. Dark regions correspond to increased atomic density. The extension of the image is $\sim 44\hbar k$. (b) Expected pattern. From Rauner et al. [182], reproduced by permission of the authors.

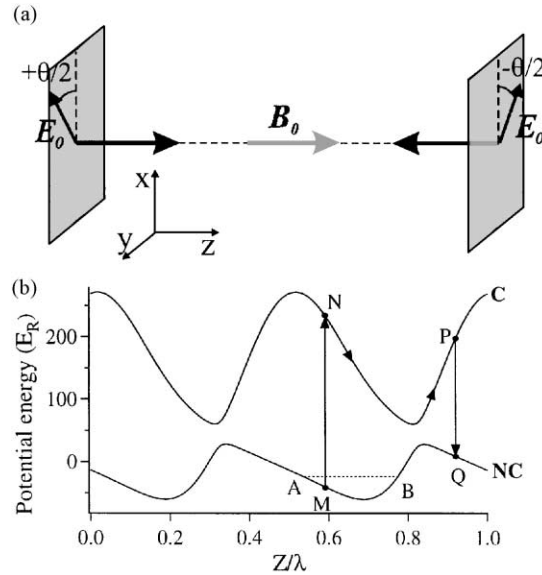


Fig. 58. (a) Beam configuration used to create an asymmetric potential and consisting of two counter-propagating beams with linear polarizations making an angle θ . A small magnetic field \mathbf{B}_0 is added along the propagation axis. (b) Resulting potential for an atom having a $F=1 \rightarrow F'=1$ transition and for blue-detuned light. The arrows indicate the jumping process inducing a net movement of the atoms. The potential curve corresponding to the $m_g = 0$ state is not represented because this state is not populated by optical pumping.

the potential experienced by a motor due to the fiber has a sawtooth shape, i.e. it is periodic but asymmetric. Although the periodicity of the potential ensures that no macroscopic force acts on the motors, a deterministic flux of particles is obtained in the presence of dissipation, which arises from ATP burning. More generally, a net movement requires the breaking of spatial and temporal symmetries [190]. In optical lattices, the spatial symmetry breaking comes from the

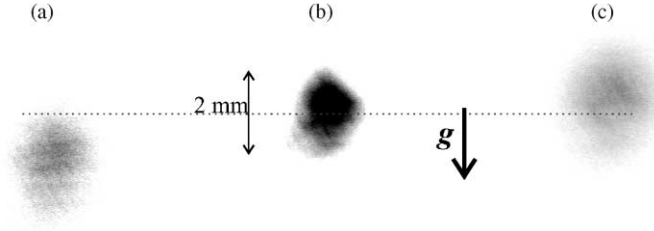


Fig. 59. Experimental images obtained for $\theta = 45^\circ$, $\Delta = 2\Gamma$ and $\Delta'_0 \simeq 100\omega_R$, after 6 ms of asymmetric optical lattice, for $B_0 = 0.5$ G (a), $B_0 = 0$ (b) and $B_0 = -0.5$ G (c). Because of gravity \mathbf{g} , the cloud has moved less in (c) than in (a). From Mennerat-Robilliard et al. [191].

simultaneous use of light and magnetic fields, and dissipation originates from optical pumping that transfers the atoms from one potential curve to the other.

The process leading to a net atomic flux is represented in Fig. 58b: in the first step, the atom is localized in a potential well of the internal dark state where it oscillates (A–B in Fig. 58b). It is then transferred to the coupled state by an optical pumping process (M–N) where it starts oscillating (N–P) before being optically pumped back to the lowest potential surface (P–Q). As the potential minima of the two curves are shifted with respect to one another, the probability that the atom has moved towards the well located on the right of the initial well is larger than the probability that it jumped into the well situated on the left. This simple theoretical model is confirmed by semi-classical numerical simulations [191]. Although the occurrence of a directed motion looks obvious in this scheme, a detailed inspection shows that it is not the case. In fact, the directed motion is closely related to the optical pumping rates between the internal dark state and the coupled state. When the transition rates are forced to obey the detailed balance, the directed motion disappears. The motion exists because the atoms are not at thermodynamic equilibrium.

The experimental study was performed with rubidium atoms (^{87}Rb) [191]. We show in Fig. 59 images of the atomic cloud for different values of \mathbf{B}_0 : the image (b) corresponds to a zero magnetic field, and thus to a symmetric potential. In this case the cloud does not move. In images (a) and (c), the atoms have moved in opposite directions because they correspond to opposite magnetic fields, i.e. to opposite asymmetries. The mean velocity of the atoms in the optical lattice is on the order of $10 v_R$ (v_R being the recoil velocity).

Provided that the axis of the lattice is chosen vertical, one can also measure the momentum distribution of the atoms, using a time-of-flight technique (see Section 6.1). We show in Fig. 60 the signals obtained for $B_0 = 0$ (Fig. 60b) and for $B_0 = \pm 0.5$ G (Fig. 60a and c) [191]. As expected, the momentum distribution corresponding to a symmetric potential is symmetric while the distributions (Fig. 60a and c), which are obtained for opposite magnetic fields, exhibit opposite asymmetries. From the shape of the distributions one can infer that the atoms are most of the time localized in a potential well where their average velocity is zero, and they hop only from time to time, then contributing to the asymmetric wing of the distribution.

Finally, the need of spatial symmetry breaking appears in the fact that for all parameters leading to a symmetrical potential ($B_0 = 0$ or $\theta = 0$ or $\pi/2$ for example), no net flux is observed. The role of dissipation can also be studied by varying both the light intensity and the detuning

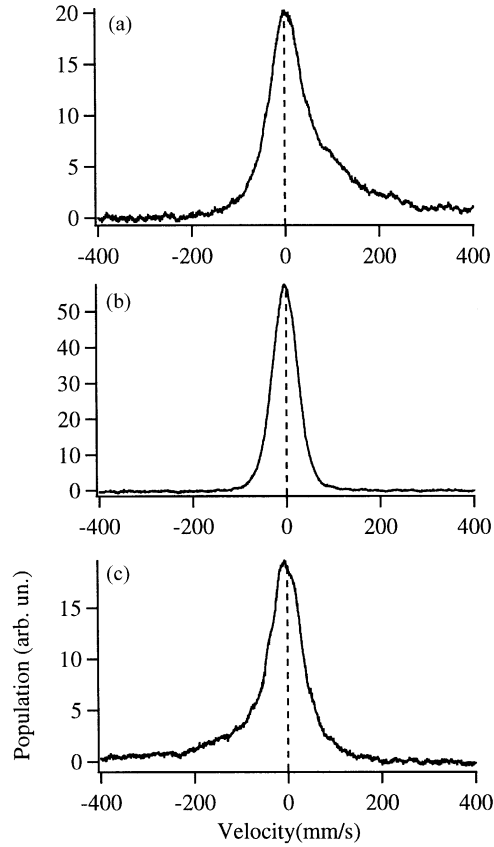


Fig. 60. Experimental momentum distribution measured with a time-of-flight technique for $\theta = 45^\circ$, $\Delta = 2\Gamma$ and $\Delta'_0 \simeq 200\omega_R$, after 6 ms of asymmetric optical lattice, for $B_0 = 0.5$ G (a), $B_0 = 0$ (b) and $B_0 = -0.5$ G (c). From Mennerat-Robilliard et al. [191].

to keep Δ'_0 constant while varying the optical pumping rate: as expected, the mean velocity increases with dissipation [191].

10. Nanolithography

Nanolithography is the most developed application of optical lattices to date. The ability of designing and fabricating devices on the nanometer scale is indeed one of the very important technological and industrial challenges of the time. Various technologies are presently under development, but none offers yet both a resolution in the tens of nanometers and the possibility of a parallel fabrication. For example, the resolution of electron or ion beam lithography goes down to the 10-nm range [192], but massive fabrication is still difficult to implement. The STM (scanning tunneling microscopy) technology has also been adapted several years ago for very high resolution lithography [193], and it becomes now possible to design very small active

devices by positioning the atoms one by one. However, this kind of technique is not suited for industrial fabrication yet.

The idea thus arises to use the natural periodicity of light interference patterns to make light masks for atoms. Compared with traditional material masks [194], these light masks offer an almost perfect periodicity and an appreciable robustness.

We first present the principle of an atom nanolithography experiment (Section 10.1). In a second paragraph, we discuss the main experimental achievements (Section 10.2) and we finally sketch the present research directions concerning laser-controlled nanolithography (Section 10.3).

10.1. *The principles of atomic nanolithography*

The first idea of focusing atoms on a nanometer-scale with near-resonant light was proposed by Balykin and Letokhov [195]. More precisely, they suggested to use a focused doughnut mode (TEM_{01}^*) laser beam as a lens for neutral atoms, similarly to magnetic lenses for charged particles. Experimentally, the atoms are rather focused in a laser standing wave, which allows for an intrinsic massive parallelism.

Fig. 61 shows the schematic of an experiment. An atomic beam is collimated by transverse laser cooling and is then focused in a standing wave just before depositing on a substrate. Depending on the sign of the light mask detuning with respect to atomic resonance, the atoms are channelled along the maximum or minimum intensity lines.

Using an atom optics approach, one can describe each node of the standing wave as a lens and predict the first order properties and aberrations of this lens, either with a time-dependent trajectory analysis [196] or with a particle optics approach [197]. Numerical simulations can also be useful to go beyond the first order approximation. We show in Fig. 62 the trajectories resulting from an exact numerical solution of the equation of motion for an atom in a Gaussian standing wave [197]. The flux appears to be very well focused. However, such results are not obtained in practice, partly because the initial velocity distribution is usually thermal and mainly because the incoming beam is not perfectly collimated. Other technical reasons also contribute to broaden the atomic flux, such as vibrations of the apparatus or atomic mobility on the substrate.

10.2. *Experimental achievements*

The first focusing experiment with a laser light field consisted of focusing a beam of metastable He atoms on a single period of a large period standing light wave. This allowed the imaging of an object with this neutral atoms lens [198]. Shortly afterwards, a one-dimensional standing light wave was used to focus an atomic beam before deposition on a substrate, first with sodium atoms [199,200], and then also with chromium [201,202] and aluminium [203] atoms. A two-step laser-controlled atom nanolithography process is also possible, by using either metastable [204–206] or cesium atoms [207] that react on a self-assembled monolayer (SAM). A subsequent chemical etching engraves the substrate where the SAM was exposed.

In all these experiments, the period of the deposited line-pattern is $\lambda/2$, thus on the order of a few hundreds of nanometers. However, one can overcome this limitation by taking into account the polarizations of the laser beams: for a $\text{lin} \perp \text{lin}$ configuration and an atomic transition

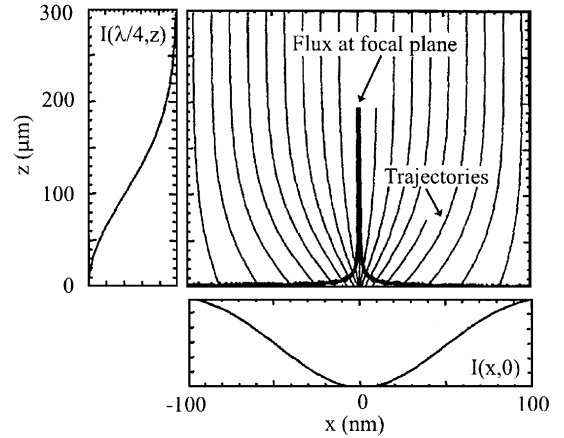
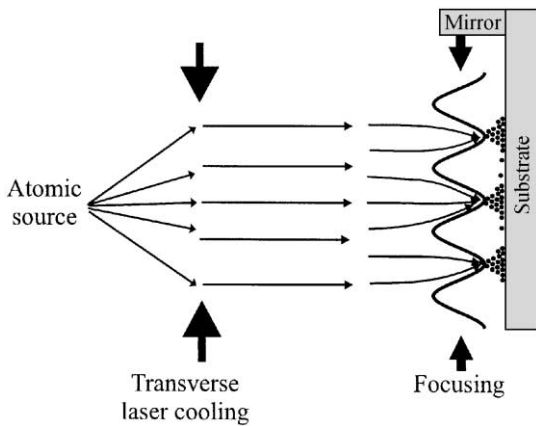


Fig. 61. Schematic of a laser-controlled nanolithography experiment. An atomic beam is collimated by laser techniques before being focused by a standing wave and deposited on a substrate. Note that the mirror retro-reflecting the beam is usually glued on the substrate itself, to prevent the deposited pattern from being washed out by vibrations.

Fig. 62. Exact trajectory calculation of laser focusing of chromium atoms in a standing wave with a Gaussian envelope. A series of trajectories are shown for varying initial x values. All trajectories are given for the same initial velocity of 926 m/s and a zero initial angle relative to the z axis. Also shown is a plot of the atomic flux at the focal plane, assuming a uniform flux entering the lens, and laser beam profiles $I(x, z)$ along x (bottom) and z (left). The laser intensity and detuning are chosen to satisfy the condition required for focusing at the center of the beam [197]. From McClelland [197], reproduced by permission of the author.

$J = 1/2 \rightarrow J' = 3/2$, the distance between two adjacent potential wells is $\lambda/4$ (see Section 3.1.2). For $J \rightarrow J + 1$ atomic transitions with $J \geq 1$, the anticrossings of adiabatic potentials (see Fig. 12a) give rise to supplementary potential minima for the upper potential curves, where the atoms can also be focused. A $\lambda/8$ period was achieved this way by the group of McClelland [208]. In order to populate more efficiently the potential wells of the upper potential curves, one can also use a static homogeneous magnetic field perpendicular to the light mask plane: the induced mixing of levels splits the potential curves and makes the adiabatic approximation easier to fulfil, even at anticrossing points. As a result, the atoms follow their own adiabatic curve without undergoing any nonadiabatic transition and can populate the secondary potential wells more efficiently [209].

Another extension of this technique consists of using two-dimensional standing light waves. One then obtains square lattices [210] or honey-comb [211] structures, depending on the number and the geometry of the laser beams. We show in Fig. 63 atomic force microscope pictures of two-dimensional chromium nanostructures. The atoms are focused by a standing wave resulting from the interference of three coplanar beams with wavevectors making 120° angles. Fig. 63a was obtained for red-detuned laser beams (thus the atoms are focused on the antinodes of the light field) while Fig. 63b corresponds to the same geometry, with a blue detuning (the atoms are focused on the nodes of the field).

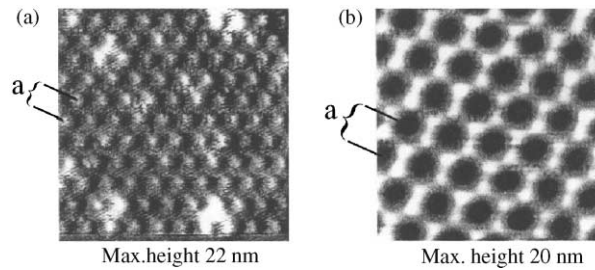


Fig. 63. AFM pictures of chromium nanostructures obtained by focusing on a 2D standing light wave resulting from the interference of three coplanar beams propagating with angle 120° with respect to each other. (a) The laser is red-detuned, so that the atoms are attracted into high intensity regions. (b) The laser is blue-detuned. The atoms are expelled from the points of highest intensity. From Drodofsky et al. [211], reproduced by permission of the authors.

10.3. Latest research directions

The ability of depositing nanoscale patterns of neutral atoms with light masks is now well established. Three main research axes develop now. First, one must reduce further the width of the deposited features, in order to improve the resolution and to be competitive with other techniques [212]. This requires a good understanding of the growth process and a precise control of the deposition conditions. The second axis aims at depositing arbitrary figures, which is a necessary step before considering an industrial development. One can think of using holographic techniques or photorefractive materials to generate an arbitrary light pattern onto which the atoms are focused. A third research direction consists of fabricating with the existing technique “useful” nanostructures: for instance, one can think of depositing isolated dots of a magnetic atom to make magnetic memories. Another idea would be to take advantage of the material selectivity of laser-controlled nanolithography to deposit complex three-dimensional structures, for example one atomic species homogeneously and another according to a light mask [213]. This would result in a material with a nanostructured doping, i.e. a candidate for a photonic crystal.

11. Conclusion

We have presented in this review what we believe to be the most interesting results concerning dissipative optical lattices. In fact, this is a timely period to write a review. This subject is now mature and the probability to find a totally unexpected and interesting result is rather low. Although the subject is still active, most of the present researches tend to improve our knowledge about phenomena that have not been studied yet with enough precision. This is for example the case of spatial diffusion and of nonlinear atom dynamics. However, it should also be kept in mind that optical lattices are a fantastic scale model to study processes found in solid-state materials and in statistical physics, but with totally different scales. Furthermore, there is a relatively large flexibility in the design of the optical potentials. This flexibility was

used to produce for example an atomic motor and can be adapted tomorrow to many other problems.

Nevertheless, those who wish to find a major breakthrough have probably more chances to reach their goal by studying far off resonant optical lattices or perhaps mesoscopic optical lattices. Because of their vanishingly small dissipation, far off resonant lattices are particularly well adapted to quantum studies about the external degrees of freedom. A few spectacular effects, such as Bloch oscillations [75], quantum chaos [214,215] and mesoscopic quantum coherence [219], are examples of what can be expected in this direction. Still more interesting are the effects that could be observed by filling an optical lattice with a Bose condensate [216,217] or a degenerate Fermi gas. But this is another world, beyond the scope of this paper.

Acknowledgements

The authors are indebted to all the physicists that share their interest on optical lattices and had a discussion with them during the last years. In particular, they would like to acknowledge daily enlightening conversations and meetings with their colleagues from the ENS and most particularly with Claude Cohen-Tannoudji, Yvan Castin, Jean-Yves Courtois, Jean Dalibard, Christophe Salomon, Philippe Verkerk, Peter Horak, David M. Lucas, David R. Meacher, Samuel Guibal, Luca Guidoni, Brahim Lounis, Konstantinos I. Petsas and Christine Triché. The friendly competition with the groups of William D. Phillips and Theodor W. Hänsch was another source of inspiration. Finally, fruitful discussions with distinguished colleagues during visits or conferences were also extremely helpful. Among them the authors wish especially to thank William D. Phillips, Alain Aspect, Paul R. Berman, Harold J. Metcalf, Jacques Vigué, Herbert Walther and all their colleagues from the TMR network “Quantum Structures” (European Commission contract FRMX-CT96-0077).

Laboratoire Kastler Brossel is an unité de recherche de l’Ecole Normale Supérieure, de l’Université Pierre et Marie Curie et du CNRS (UMR 8552). Laboratoire Collisions, Agrégats, Réactivité is an unité de recherche de l’Université Paul Sabatier et du CNRS (UMR 5589).

Appendix A. Index of notations

Notation Definition

a	amplitude of the vibration motion
\mathbf{a}_i	primitive translation of the optical lattice
\mathbf{a}_i^*	primitive translation of the reciprocal lattice
a_M	transverse spatial period (Talbot lattice)
\mathbf{A}_t	topological vector potential
\mathbf{d}	electric dipole moment
\hat{d}	reduced dipole operator
\mathbf{d}^\pm	upwards (downwards) component of the atomic dipole
D	momentum diffusion coefficient

\mathcal{D}	reduced matrix element of the atomic dipole
D_{sp}	spatial diffusion coefficient
\mathbf{e}_{\pm}	unit vectors for the circular polarizations
E_0	field amplitude of a single lattice beam
$E_0(\mathbf{R})$	lattice field amplitude in \mathbf{R}
E^{\pm}	circular components of the field
E^{π}	lattice field component along Oz
$E^{(\pm)}$	positive (negative) frequency component of the field
E_{p}	probe beam amplitude
$E_{\text{R}} = \hbar^2 k^2 / 2M$	recoil energy
E_n	energy of the vibrational state $ \psi_n\rangle$
$\mathbf{F}'(\mathbf{R})$	reactive (dipole) force
$\mathbf{F}''(\mathbf{R})$	dissipative force (radiation pressure)
$\bar{\mathbf{F}}$	average value of the dipole force (multilevel atom)
\mathbf{G}	vector of the reciprocal lattice
$H_{\text{eff}} = P^2 / 2M + \hat{U}$	Hamiltonian (external degrees of freedom)
$I^{\pm} = E^{\pm} ^2$	intensity of the circular component of the field
I	field intensity
\mathbf{k}_i	wavevector of a lattice beam
$k = \omega/c$	modulus of the wavevector of a lattice beam
\mathbf{k}_{p}	probe beam wavevector
k_{B}	Boltzmann constant
$K_{\perp} = k \sin \theta$	transverse spatial frequency
$K = k(1 - \cos \theta)$	longitudinal spatial frequency (3-beam lattice)
$K_{x,y} = k \sin \theta_{x,y}$	transverse spatial frequency (3D 4-beam lattice)
$K_{\pm} = k(\cos \theta_x \pm \cos \theta_y)/2$	longitudinal spatial frequency (3D 4-beam lattice)
L	length of the atomic cloud
m_{e}	electron mass
$ m\rangle$	Zeeman substate
$ n\rangle_{\text{ho}}$	eigenstate of the harmonic oscillator
M	atomic mass
\mathbf{P}	atom momentum
\mathcal{P}	atomic polarization
$\hat{\mathcal{P}}$	effective coupling operator (external state variables)
q_{e}	electron charge
\mathbf{r}_{e}	electron position in the atomic rest frame
\mathbf{R}	atom position
s_0	saturation parameter for a single beam
$s(\mathbf{R})$	saturation parameter in \mathbf{R}
S	structure factor
$\tilde{S}(t), S(\Omega)$	transient probe emission (time and frequency domain)
T	kinetic temperature
$\hat{u}(\mathbf{R})$	dimensionless light-shift Hamiltonian

$U(\mathbf{R})$	dipole potential
\hat{U}	light-shift Hamiltonian
U_{\pm}, U_n	eigenvalues of the light-shift (adiabatic energies)
$U_0 = -4\hbar\Delta'_0/3$	depth of the 1D lin \perp lin lattice
U_t	scalar topological potential
$U_{\pm}^{(p)}$	shift of the optical potential induced by the probe
v	atomic velocity
\bar{v}	average atomic velocity
$v_R = \hbar k/M$	recoil velocity
$V_m = \langle m \hat{U} m \rangle$	diabatic potentials
\hat{V}_{AL}	electric dipole interaction
$W(\mathbf{R}, \mathbf{P}, t)$	Wigner representation of the atomic density matrix σ
z_T	Talbot length
α	friction coefficient
α_0	atomic polarizability
β	Debye–Waller factor
Γ	radiative width of the upper level
Γ_p	optical pumping rate
$\Gamma'_0 = \Gamma s_0/2$	photon scattering rate per beam
$\Gamma'(\mathbf{R}) = \Gamma s(\mathbf{R})/2$	photon scattering rate in \mathbf{R}
Γ'	photon scattering rate at a point where the lattice field is σ^{\pm}
$\delta = \omega_p - \omega$	probe–lattice frequency detuning
δ_L	frequency difference between lattice beams
$\Delta'_0 = \Delta s_0/2$	light-shift per beam
$\Delta'(\mathbf{R}) = \Delta s(\mathbf{R})/2$	light-shift in \mathbf{R}
Δ'	light-shift at a point where the lattice field is σ^{\pm}
\mathbf{e}_i	polarization of a lattice beam
$\mathbf{e}(\mathbf{R})$	local polarization of the field
η	planar density of atoms
$\theta, \theta_{x,y}$	angles between lattice beams
$\lambda = 2\pi/k$	wavelength of a lattice beam
$\lambda_{x,y} = \lambda / \sin \theta_{x,y}$	transverse spatial period (3D 4-beam lattice)
$\lambda_{+}/2 = \lambda / (\cos \theta_x + \cos \theta_y)$	longitudinal spatial period (3D 4-beam lattice)
$\lambda_{\perp} = \lambda / \sin \theta$	transverse spatial period
$\Lambda = \lambda / (1 - \cos \theta)$	longitudinal spatial period
ξ_v	shift of the vibrational resonance caused by anharmonicity
$\pi(n)$	population of the vibrational level (band) n
Π_{\pm}	population of the Zeeman substates ($J = 1/2$)
Π_n	population of the adiabatic state $ \Phi_n\rangle$
ρ	atomic density matrix
σ	reduced atomic density matrix (ground state)
σ^{\pm}	circular polarizations
ϕ_i	phase of a lattice beam

$ \Phi_n\rangle$	adiabatic states
$ \Phi_{\text{NC}}\rangle$	internal dark state
χ	atomic susceptibility
$ \psi_n\rangle$	vibrational eigenstate
ω	frequency of a lattice beam
ω_0	atomic resonance frequency
$\omega_p = \omega + \delta$	probe beam frequency
$\omega_R = E_R + \hbar$	recoil frequency
Ω_1	resonant Rabi frequency for a single beam
Ω_v	vibration frequency
$\Omega_{x,y,z}$	vibrational frequency along x, y, z
Ω_B	Brillouin resonance
Ω_0	Zeeman splitting

References

- [1] G. Grynberg, P. Verkerk, J.-Y. Courtois, C. Salomon, B. Lounis, Oscillation of atoms in a wavelength-size optical potential: observation by Raman spectroscopy, in *International Conference on Quantum Electronics Technical Digest Series*, Vol. 9 (1992) p. 348.
- [2] P. Verkerk, B. Lounis, C. Salomon, C. Cohen-Tannoudji, J.-Y. Courtois, G. Grynberg, Dynamics and spatial order of cold cesium atoms in a periodic optical potential, *Phys. Rev. Lett.* 68 (1992) 3861.
- [3] P.S. Jessen, C. Gerz, P.D. Lett, W.D. Phillips, S.L. Rolston, R.J.C. Spreeuw, C.I. Westbrook, Observation of quantized motion of Rb atoms in an optical field, *Phys. Rev. Lett.* 69 (1992) 49.
- [4] J. Dalibard, C. Cohen-Tannoudji, Laser cooling below the Doppler limit by polarization gradients: simple theoretical models, *J. Opt. Soc. Am. B* 6 (1989) 2023.
- [5] P.J. Ungar, D.S. Weiss, E. Riis, S. Chu, Optical molasses and multilevel atoms: theory, *J. Opt. Soc. Am. B* 6 (1989) 2058.
- [6] P.D. Lett, R.N. Watts, C.I. Westbrook, W.D. Phillips, P.L. Gould, H.J. Metcalf, Observation of atoms laser cooled below the Doppler limit, *Phys. Rev. Lett.* 61 (1988) 169.
- [7] C.I. Westbrook, R.N. Watts, C.E. Tanner, S.L. Rolston, W.D. Phillips, P.D. Lett, P.L. Gould, Localization of atoms in a three-dimensional standing wave, *Phys. Rev. Lett.* 65 (1990) 33.
- [8] R.H. Dicke, The effect of collisions upon the Doppler width of spectral lines, *Phys. Rev.* 89 (1953) 472.
- [9] S. Chu, L. Hollberg, J.E. Bjorkholm, A. Cable, A. Ashkin, Three-dimensional viscous confinement and cooling of atoms by resonance radiation pressure, *Phys. Rev. Lett.* 55 (1985) 48.
- [10] C. Cohen-Tannoudji, J. Dupont-Roc, G. Grynberg, *Atom-Photon Interactions: Basic Processes and Applications*, Wiley Science Paperback Series, New York, 1998.
- [11] M.M. Burns, J.-M. Fournier, J.A. Golovchenko, Optical matter: crystallization and binding in intense optical fields, *Science* 249 (1990) 749.
- [12] M. Campbell, D.N. Sharp, M.T. Harrison, R.G. Denning, A.J. Turberfield, Fabrication of photonic crystals for the visible spectrum by holographic lithography, *Nature* 404 (2000) 53.
- [13] G. Grynberg, B. Lounis, P. Verkerk, J.-Y. Courtois, C. Salomon, Quantized motion of cold cesium atoms in two- and three-dimensional optical potentials, *Phys. Rev. Lett.* 70 (1993) 2249.
- [14] K.I. Petsas, A.B. Coates, G. Grynberg, Crystallography of optical lattices, *Phys. Rev. A* 50 (1994) 5173.
- [15] Nobel lectures: S. Chu, The manipulation of neutral particles, *Rev. Mod. Phys.* 70 (1998) 685; C. Cohen-Tannoudji, Manipulating atoms with photons, *ibid.*, p. 707; W.D. Phillips, Laser cooling and trapping of neutral atoms, *ibid.*, p. 721.
- [16] C. Cohen-Tannoudji, Atomic motion in laser light, in: J. Dalibard, J.-M. Raimond, J. Zinn-Justin (Eds.), *Fundamental Systems in Quantum Optics*, Les Houches Summer School of Theoretical Physics 1990, Session LIII, Elsevier Science, Amsterdam, 1992.

- [17] E. Arimondo, Coherent population trapping in laser spectroscopy, in: E. Wolf (Ed.), *Progress in Optics*, Vol. XXXV, North-Holland, Amsterdam, 1996, pp. 257–354.
- [18] J.-P. Barrat, C. Cohen-Tannoudji, Etude du pompage optique dans le formalisme de la matrice densité. *J. Phys. (Paris)* 22 (1961) 329; *ibid.* (1961) 443.
- [19] C. Cohen-Tannoudji, J. Dupont-Roc, G. Grynberg, *Atoms and Photons—Introduction to Quantum Electrodynamics*, Wiley, New York, 1989.
- [20] C. Cohen-Tannoudji, J. Dupont-Roc, Experimental study of Zeeman light-shifts in weak magnetic fields, *Phys. Rev. A* 5 (1972) 968.
- [21] A. Ashkin, Acceleration and trapping of particles by radiation pressure, *Phys. Rev. Lett.* 24 (1970) 156.
- [22] V.S. Letokhov, V.G. Minogin, B.D. Pavlik, Cooling and trapping atoms and molecules by a resonant laser field, *Opt. Commun.* 19 (1976) 72.
- [23] T.W. Hänsch, A.L. Schawlow, Cooling of gases by laser radiation, *Opt. Commun.* 13 (1975) 68.
- [24] C. Salomon, J. Dalibard, A. Aspect, H. Metcalf, C. Cohen-Tannoudji, Channeling atoms in a laser standing wave, *Phys. Rev. Lett.* 59 (1987) 1659.
- [25] A. Hemmerich, T.W. Hänsch, Two-dimensional atomic crystal bound by light, *Phys. Rev. Lett.* 70 (1993) 410.
- [26] K.I. Petsas, C. Triché, L. Guidoni, C. Jurczak, J.-Y. Courtois, G. Grynberg, Pinball atom dynamics in an antidot optical lattice, *Europhys. Lett.* 46 (1999) 18.
- [27] L. Guidoni, P. Verkerk, Direct observation of atomic localization in atomic superlattices, *Phys. Rev. A* 57 (1998) R1501.
- [28] C. Kittel, *Introduction to Solid State Physics*, 6th Ed., Wiley, New York, 1986.
- [29] N.W. Ashcroft, N.D. Mermin, *Solid State Physics*, HRW International Editions, New York, 1976.
- [30] P.J. Steinhardt, S. Ostlund (Eds.), *The Physics of Quasicrystals*, World Scientific, Singapore, 1987.
- [31] D.P. DiVincenzo, P.J. Steinhardt (Eds.), *Quasicrystals, the State of the Art*, World Scientific, Singapore, 1991.
- [32] F. Hippert, D. Gratias (Eds.), *Lectures on Quasicrystals*, Les Editions de Physique, Paris, 1994.
- [33] See for example J.-P. Pouget, *Solid State Phase Transformations in Metals and Alloys*, Les Editions de Physique, Les Ulis, 1978.
- [34] D. Shechtman, I. Blech, D. Gratias, J.W. Cahn, Metallic phase with long-range orientational order and no translational symmetry, *Phys. Rev. Lett.* 53 (1984) 1951.
- [35] H. Bohr, *Acta Math.* 45 (1924) 29; *ibid.* 46 (1925) 101; *ibid.* 47 (1926) 237.
- [36] A. Katz, D. Gratias, Tilings and quasicrystals, in: F. Hippert, D. Gratias (Eds.), *Lectures on quasicrystals*, Les Editions de Physique, Paris, 1994, p. 187.
- [37] J.E.S. Socolar, P.J. Steinhardt, D. Levine, Quasicrystals with arbitrary orientational symmetry, *Phys. Rev. B* 32 (1985) 5547.
- [38] L. Guidoni, C. Triché, P. Verkerk, G. Grynberg, Quasiperiodic optical lattices, *Phys. Rev. Lett.* 79 (1997) 3363.
- [39] A. Janner, T. Janssen, Symmetry of periodically distorted crystals, *Phys. Rev. B* 15 (1977) 643.
- [40] R. Penrose, *Bull. Inst. Math. Appl.* 10 (1974) 266.
- [41] A. Hemmerich, C. Zimmermann, T.W. Hänsch, Sub-kHz Rayleigh resonance in a cubic atomic crystal, *Europhys. Lett.* 22 (1993) 89.
- [42] P. Verkerk, D.R. Meacher, A.B. Coates, J.-Y. Courtois, S. Guibal, B. Lounis, C. Salomon, G. Grynberg, Designing 3D optical lattices—an investigation with cesium atoms, *Europhys. Lett.* 26 (1994) 171.
- [43] F. Talbot, Facts relating to optical science. N°4'', *Philos. Mag.* 9 (1836) 401.
- [44] K. Patorski, The self-imaging phenomenon and its applications, in: E. Wolf (Ed.), *Progress in Optics*, Vol. XXVII, North-Holland, Amsterdam, 1989, pp. 1–110.
- [45] P. Latimer, R.F. Crouse, Talbot effect reinterpreted, *Appl. Opt.* 31 (1992) 80–89.
- [46] C. Mennerat-Robilliard, D. Boiron, J.-M. Fournier, A. Aradian, P. Horak, G. Grynberg, Cooling cesium atoms in a Talbot lattice, *Europhys. Lett.* 44 (1998) 442.
- [47] D. Boiron, A. Michaud, J.-M. Fournier, L. Simard, M. Sprenger, G. Grynberg, C. Salomon, Cold and dense cesium clouds in far-detuned dipole traps, *Phys. Rev. A* 57 (1998) R4106.

- [48] D. Boiron, C. Mennerat-Robilliard, J.-M. Fournier, L. Guidoni, C. Salomon, G. Grynberg, Trapping and cooling cesium atoms in a speckle field, *Eur. Phys. J. D* 7 (1999) 373.
- [49] A. Kastler, Quelques suggestions concernant la production optique et la détection optique d'une inégalité de population des niveaux de quantification spatiale des atomes. Application à l'expérience de Stern et Gerlach et à la résonance magnétique, *J. Phys. Rad.* 11 (1950) 255.
- [50] C. Cohen-Tannoudji, Théorie quantique du cycle de pompage optique, *Ann. Phys. (Paris)* 7 (1962) 423.
- [51] G. Grynberg, M. Vallet, M. Pinard, Redistribution of photons and frequency mixing with cross-polarized beams in sodium, *Phys. Rev. Lett.* 65 (1990) 701.
- [52] K.I. Petsas, G. Grynberg, J.-Y. Courtois, Semi-classical Monte-Carlo approaches for realistic atoms in optical lattices, *Eur. Phys. J. D* 6 (1999) 29.
- [53] R. Dum, M. Ol'Shanii, Gauge structures in atom-laser interaction: Bloch oscillations in a dark lattice, *Phys. Rev. Lett.* 76 (1996) 1788.
- [54] G. Alzetta, A. Gozzini, L. Moi, G. Orriols, An experimental method for the observation of R.F. transitions and laser beat resonances in oriented Na vapour, *Nuova Cimento B* 36 (1976) 5.
- [55] E. Arimondo, G. Orriols, Nonabsorbing atomic coherences by coherent two-photon transitions in a three-level optical pumping, *Lett. Nuovo Cimento* 17 (1976) 333.
- [56] H.R. Gray, R.M. Whitley, C.R. Stroud Jr., Coherent trapping of atomic populations, *Opt. Lett.* 3 (1978) 218.
- [57] M.S. Shahriar, P.R. Hemmer, M.G. Prentiss, P. Marte, J. Mervis, D.P. Katz, N.P. Bigelow, T. Cai, Continuous polarization gradient precooling-assisted velocity-selective coherent population trapping, *Phys. Rev. A* 48 (1993) R4035.
- [58] P. Marte, R. Dum, R. Taïeb, P. Zoller, M.S. Shahriar, M. Prentiss, Polarization-gradient-assisted subrecoil cooling: quantum calculations in one dimension, *Phys. Rev. A* 49 (1994) 4826.
- [59] M. Weidemüller, T. Esslinger, M.A. Ol'shanii, A. Hemmerich, T.W. Hänsch, A novel scheme for efficient cooling below the photon recoil limit, *Europhys. Lett.* 27 (1994) 109.
- [60] A. Aspect, E. Arimondo, R. Kaiser, N. Vansteenkiste, C. Cohen-Tannoudji, Laser cooling below the one-photon recoil energy by velocity-selective coherent population trapping, *Phys. Rev. Lett.* 61 (1988) 826.
- [61] J.P. Gordon, A. Ashkin, Motion of atoms in a radiation trap, *Phys. Rev. A* 21 (1980) 1606.
- [62] T.W. Hodapp, C. Gerz, C. Furthlehner, C.I. Westbrook, W.D. Phillips, J. Dalibard, Spatial diffusion in 3D optical molasses, *Appl. Phys. B* 60 (1995) 135.
- [63] S. Marksteiner, K. Ellinger, P. Zoller, Anomalous diffusion and Lévy walks in optical lattices, *Phys. Rev. A* 53 (1996) 3409.
- [64] J.-Y. Courtois, G. Grynberg, Stimulated Rayleigh resonances and recoil-induced effects, *Adv. Atom. Mol. Opt. Phys.* 36 (1996) 88–140.
- [65] Y. Castin, J. Dalibard, C. Cohen-Tannoudji, The limits of Sisyphus cooling, in: L. Moi, S. Gozzini, C. Gabbanini, E. Arimondo, F. Strumia (Eds.), *Light induced kinetic effects on atoms, ions and molecules*, Proceedings of the LIKE Workshop, E.T.S. Editrice, Pisa, 1991.
- [66] R. Dum, P. Zoller, H. Ritsch, Monte Carlo simulation of the atomic master equation for spontaneous emission, *Phys. Rev. A* 45 (1992) 4879.
- [67] Y. Castin, J. Dalibard, Quantization of atomic motion in optical molasses, *Europhys. Lett.* 14 (1991) 761.
- [68] R. Taïeb, P. Marte, R. Dum, P. Zoller, Spectrum of resonance fluorescence and cooling dynamics in quantized one dimensional molasses; effects of laser configuration, *Phys. Rev. A* 47 (1993) 4986.
- [69] K.I. Petsas, J.-Y. Courtois, G. Grynberg, Temperature and magnetism of gray optical lattices, *Phys. Rev. A* 53 (1996) 2533.
- [70] C. Triché, P. Verkerk, G. Grynberg, Blue-Sisyphus cooling in cesium gray molasses and antidot lattices, *Eur. Phys. J. D* 5 (1999) 225.
- [71] D. Lucas, P. Horak, G. Grynberg, Sisyphus cooling of rubidium atoms on the $D_2(F=1 \rightarrow F'=1)$ line: the role of the neighbouring transitions, *Eur. Phys. J. D* 7 (1999) 261.
- [72] J.-Y. Courtois, G. Grynberg, Probe transmission in one-dimensional optical molasses: Theory for linearly cross-polarized cooling beams, *Phys. Rev. A* 46 (1992) 7060.
- [73] B.P. Anderson, T.L. Gustavson, M.A. Kasevich, Atom trapping in nondissipative optical lattices, *Phys. Rev. A* 53 (1996) R3727.

- [74] S.R. Wilkinson, C.F. Bharucha, K.W. Madison, Qian Niu, M.G. Raizen, Observation of atomic Wannier-Stark ladders in an accelerating optical potential, *Phys. Rev. Lett.* 76 (1996) 4512.
- [75] M. Ben Dahan, E. Peik, J. Reichel, Y. Castin, C. Salomon, Bloch oscillations of atoms in an optical potential, *Phys. Rev. Lett.* 76 (1996) 4508.
- [76] D.L. Haycock, S.E. Hamann, G. Klose, P.S. Jessen, Atom trapping in deeply bound states of a far-off-resonance optical lattice, *Phys. Rev. A* 55 (1997) R3991.
- [77] T. Müller-Seydlitz, M. Hartl, B. Brezger, H. Hänsel, C. Keller, A. Schnetz, R.J.C. Spreeuw, T. Pfau, J. Mlynek, Atoms in the Lowest Motional Band of a Three-dimensional Optical Lattice, *Phys. Rev. Lett.* 78 (1997) 1038.
- [78] S. Friebe, C. D'Andrea, J. Walz, M. Weitz, T.W. Hänsch, CO₂-laser optical lattice with cold rubidium atoms, *Phys. Rev. A* 57 (1998) R20.
- [79] S.L. Winoto, M.T. DePue, N.E. Bramall, D.S. Weiss, Laser cooling at high density in deep far-detuned optical lattices, *Phys. Rev. A* 59 (1999) R19.
- [80] R.L. Mossbauer, Rückstoßfreie Kernresonanzabsorption von Gammastrahlung, in *Les Prix Nobel 1961*, pp. 136–151, Norstedt, Stockholm, 1962; see also in: H. Fraunfelder (Ed.), *The Mossbauer effect*, Benjamin, New York, 1962.
- [81] A. Abragam, *The Mossbauer Effect*, Gordon and Breach, New York, 1964.
- [82] W.E. Lamb Jr., Capture of neutrons in a crystal, *Phys. Rev.* 55 (1939) 190.
- [83] J.-Y. Courtois, Spectroscopie Raman et Rayleigh stimulée des mélasses optiques unidimensionnelles, *Ann. Phys. (France)* 21 (1996) 1–265.
- [84] P.M. Visser, G. Nienhuis, Geometric potentials for subrecoil dynamics, *Phys. Rev. A* 57 (1998) 4581.
- [85] G. Grynberg, J.-Y. Courtois, Proposal for a magneto-optical lattice for trapping atoms in nearly-dark states, *Europhys. Lett.* 27 (1994) 41.
- [86] C. Cohen-Tannoudji, Atomes ultra-froids, approches statistiques et perspectives nouvelles, *Cours de physique atomique et moléculaire*, Collège de France (1995–1996).
- [87] C. Salomon, J. Dalibard, W.D. Phillips, A. Clairon, S. Guellati, Laser cooling of cesium atoms below 3 μ K, *Europhys. Lett.* 12 (1990) 683.
- [88] H. Schadwinkel, U. Reiter, V. Gomer, D. Meschede, Magneto-optical trap as an optical lattice, *Phys. Rev. A* 61 (2000) 013409.
- [89] C. Mennerat-Robilliard, L. Guidoni, K.I. Petsas, P. Verkerk, J.-Y. Courtois, G. Grynberg, Bright optical lattices in a longitudinal magnetic field, Experimental study of the oscillating and jumping regimes, *Eur. Phys. J. D* 1 (1998) 33.
- [90] B. Sheehy, S.-Q. Shang, P. Van Der Straten, S. Hatamian, H. Metcalf, Magnetic-Field-Induced Laser Cooling below the Doppler limit, *Phys. Rev. Lett.* 64 (1990) 858.
- [91] G. Nienhuis, P. van der Straten, S.-Q. Shang, Operator description of laser cooling below the Doppler limit, *Phys. Rev. A* 44 (1991) 462.
- [92] Y. Castin, Les limites du refroidissement laser dans les mélasses optiques à une dimension, Thèse de l'Université Pierre et Marie Curie, Paris, 1992.
- [93] Y. Castin, K. Berg-Sørensen, J. Dalibard, K. Mølmer, Two-dimensional Sisyphus cooling, *Phys. Rev. A* 50 (1994) 5092.
- [94] K. Berg-Sørensen, Y. Castin, K. Mølmer, J. Dalibard, Cooling and tunneling of atoms in a 2D laser field, *Europhys. Lett.* 22 (1993) 663.
- [95] K. Berg-Sørensen, Two-dimensional Sisyphus cooling in a three-beam laser configuration, *Phys. Rev. A* 49 (1994) R4297.
- [96] J.-Y. Courtois, S. Guibal, D.R. Meacher, P. Verkerk, G. Grynberg, Propagating elementary excitation in a dilute optical lattice, *Phys. Rev. Lett.* 77 (1996) 40.
- [97] C. Jurczak, B. Desruelle, K. Sengstock, J.-Y. Courtois, C.I. Westbrook, A. Aspect, Atomic transport in an optical lattice: an investigation through polarization-selective intensity correlations, *Phys. Rev. Lett.* 77 (1996) 1727.
- [98] I.H. Deutsch, J. Grondalski, P.M. Alsing, Local dynamics of laser cooling in an optical lattice, *Phys. Rev. A* 56 (1997) R1705.

- [99] S. Guibal, C. Mennerat-Robilliard, D. Larousserie, C. Triché, J.-Y. Courtois, G. Grynberg, Radiation pressure in a rubidium optical lattice: an atomic analog to the photorefractive effect, *Phys. Rev. Lett.* 78 (1997) 4709.
- [100] J. Dalibard, Y. Castin, K. Mølmer, Wave-function approach to dissipative processes in quantum optics, *Phys. Rev. Lett.* 68 (1992) 580.
- [101] P. Marte, R. Dum, R. Taïeb, P. Zoller, Resonance fluorescence from quantized one-dimensional molasses, *Phys. Rev. A* 47 (1993) 1378.
- [102] Y. Castin, K. Mølmer, Monte Carlo wave-function analysis of 3D optical molasses, *Phys. Rev. Lett.* 74 (1995) 3772.
- [103] D. Grison, B. Lounis, C. Salomon, J.-Y. Courtois, G. Grynberg, Raman spectroscopy of cesium atoms in a laser trap, *Europhys. Lett.* 15 (1991) 149.
- [104] J.W.R. Tabosa, G. Chen, Z. Hu, R.B. Lee, H.J. Kimble, Nonlinear spectroscopy of cold atoms in a spontaneous-force optical trap, *Phys. Rev. Lett.* 66 (1991) 3245.
- [105] C. Triché, D. Boiron, S. Guibal, D.R. Meacher, P. Verkerk, G. Grynberg, Cesium atoms in grey optical lattices. Study of temperature and capture efficiency, *Optics Commun.* 126 (1996) 49.
- [106] G. Grynberg, C. Triché, Atoms in optical lattices, in: A. Aspect, W. Barletta, R. Bonifacio (Eds.), *Coherent and collective interactions of particles and radiation beams, Proceedings of the International School of Physics “Enrico Fermi” 1995*, Course CXXXI, North-Holland, Amsterdam, 1996, p. 243.
- [107] O. Morsch, P.H. Jones, D.R. Meacher, Coherent transients in optical lattices, *Phys. Rev. A* 61 (2000) 23 410.
- [108] M. Gatzke, G. Birkl, P.S. Jessen, A. Katsberg, S.L. Rolston, W.D. Phillips, Temperature and localization of atoms in three-dimensional optical lattices, *Phys. Rev. A* 55 (1997) R3987.
- [109] G. Raithel, W.D. Phillips, S.L. Rolston, Collapse and Revivals of Wave Packets in Optical Lattices, *Phys. Rev. Lett.* 81 (1998) 3615.
- [110] A. Hemmerich, T.W. Hänsch, Line strengths in vibrational spectra of a two-dimensional optical crystal, *Phys. Rev. A* 48 (1993) R1753.
- [111] L.D. Landau, E.M. Lifshitz, *Mechanics*, Butterworth–Heinemann, Oxford, 1976.
- [112] P.M. Visser, G. Grynberg, Mechanical bistability in an optical lattice, *Eur. Phys. J. D* 12 (2000) 403.
- [113] C. Mennerat-Robilliard, L. Guidoni, J.-Y. Courtois, G. Grynberg, Cooling and trapping cesium atoms in π -polarized potential wells: the jumping regime of optical lattices, *Europhys. Lett.* 38 (1997) 429.
- [114] A. Abragam, *The Principles of Nuclear Magnetism*, Chapter X, Oxford University Press, Oxford, 1961.
- [115] Y.R. Shen, *The Principles of Non-linear Optics*, Wiley-Interscience, New York, 1984.
- [116] R.W. Boyd, *Nonlinear optics*, Academic Press, New York, 1992.
- [117] R. Benzi, A. Sutera, A. Vulpiani, The mechanism of stochastic resonances, *J. Phys. A* 14 (1981) L453.
- [118] C. Triché, Refroidissement et dynamique d’atomes dans des potentiels lumineux: mélasses grises, réseaux de plots et réseaux brillants, Ph.D. Thesis, École Polytechnique, Palaiseau, 1997.
- [119] H. Katori, S. Schlipf, H. Walther, Anomalous Dynamics of a Single Ion in an Optical Lattice, *Phys. Rev. Lett.* 79 (1997) 2221.
- [120] J. Guo, P.R. Berman, B. Dubetsky, G. Grynberg, Recoil-induced resonances in nonlinear spectroscopy, *Phys. Rev. A* 46 (1992) 1426.
- [121] J. Guo, P.R. Berman, Recoil-induced resonances in pump-probe spectroscopy including effects of level degeneracy, *Phys. Rev. A* 47 (1993) 4128.
- [122] J.-Y. Courtois, G. Grynberg, B. Lounis, P. Verkerk, Recoil-induced resonances in cesium: an atomic analog to the free-electron laser, *Phys. Rev. Lett.* 72 (1994) 3017.
- [123] D.R. Meacher, D. Boiron, H. Metcalf, C. Salomon, G. Grynberg, Method for velocimetry of cold atoms, *Phys. Rev. A* 50 (1994) R1992.
- [124] J. Feinberg, D. Heiman, A.R. Tanguay Jr., R.W. Hellwarth, Photorefractive effects and light-induced charge migration in barium titanate, *J. Appl. Phys.* 51 (1980) 1297.
- [125] N.V. Kukhtarev, V.B. Markov, S.G. Odulov, M.S. Soskin, V.L. Vinetskii, Holographic storage in electro-optic crystals. I. Steady-state, *Ferroelectrics* 22 (1979) 949.
- [126] B. Lounis, J.-Y. Courtois, P. Verkerk, C. Salomon, G. Grynberg, Measurement of the friction coefficient in 1D corkscrew optical molasses by stimulated Rayleigh spectroscopy, *Phys. Rev. Lett.* 69 (1992) 3029.

- [127] J.-Y. Courtois, G. Grynberg, Probe transmission in one-dimensional optical molasses: theory for circularly cross-polarized cooling beams, *Phys. Rev. A* 48 (1993) 1378.
- [128] R.G. Brewer, Coherent optical spectroscopy, in: R. Balian, S. Haroche, S. Liberman (Eds.), *Frontiers in Laser Spectroscopy*, Les Houches Summer School of Theoretical Physics 1975, Session XXVII, North-Holland, Amsterdam, 1977, p. 341, and references therein.
- [129] C. Triché, L. Guidoni, P. Verkerk, G. Grynberg, Coherent transients in optical lattices, in: K. Burnett (Ed.), *Trends in Optics and Photonics 1996: Ultracold atoms and Bose–Einstein Condensation*, Vol. 7, Optical Society of America, Washington DC, 1997, p. 82.
- [130] M. Kozuma, Observation of a transient response of recoil-induced resonance: a method for the measurement of atomic motion in an optical standing wave, *Phys. Rev. A* 52 (1995) R3421.
- [131] M. Kozuma, K. Nakagawa, W. Jhe, M. Ohtsu, Observation of temporal behavior of an atomic wave packet localized in an optical potential, *Phys. Rev. Lett.* 76 (1996) 2428.
- [132] P. Rudy, R. Egnisman, N.P. Bigelow, Fluorescence investigation of parametrically excited motional wave packets in optical lattices, *Phys. Rev. Lett.* 78 (1997) 4906.
- [133] N.A. Kurnit, I.D. Abella, S.R. Hartmann, Observation of a photon echo, *Phys. Rev. Lett.* 13 (1964) 567.
- [134] F.B.J. Buchkremer, R. Dumke, H. Levsen, G. Birkl, W. Ertmer, Wave packet echoes in the motion of trapped atoms, *Phys. Rev. Lett.* 85 (2000) 3121.
- [135] A.E. Kaplan, Hysteresis in cyclotron resonance based on weak relativistic-mass effects of the electron, *Phys. Rev. Lett.* 48 (1982) 138.
- [136] A.E. Kaplan, Relativistic nonlinear optics of a single cyclotron electron, *Phys. Rev. Lett.* 56 (1986) 456.
- [137] G. Gabrielse, H. Dehmelt, W. Kells, Observation of a relativistic, bistable hysteresis in the cyclotron motion of a single electron, *Phys. Rev. Lett.* 54 (1985) 537.
- [138] G. Grynberg, C. Triché, L. Guidoni, P.M. Visser, Mechanical Bistability of Cesium Atoms in an Optical Lattice, *Europhys. Lett.* 51 (2000) 506.
- [139] L.A. Lugiato, The theory of optical bistability, in: E. Wolf (Ed.), *Progress in Optics*, Vol. XXI, North-Holland, Amsterdam, 1984.
- [140] A. Hemmerich, C. Zimmermann, T.W. Hänsch, Multiphoton transitions in a spin-polarized 3D optical lattice, *Phys. Rev. Lett.* 72 (1994) 625.
- [141] P.D. Lett, W.D. Phillips, S.L. Rolston, C.E. Tanner, R.N. Watts, C.I. Westbrook, Optical molasses, *J. Opt. Soc. Am. B* 6 (1989) 2084.
- [142] D.S. Weiss, E. Riis, Y. Shevy, P.J. Ungar, S. Chu, Optical molasses and multilevel atoms: experiment, *J. Opt. Soc. Am. B* 6 (1989) 2072.
- [143] C. Gerz, T.W. Hodapp, P. Jessen, K.M. Jones, W.D. Phillips, C.I. Westbrook, K. Mølmer, The temperature of optical molasses for two different angular momenta, *Europhys. Lett.* 21 (1993) 661.
- [144] A. Kastberg, W.D. Phillips, S.L. Rolston, R.J. Spreeuw, Adiabatic cooling of cesium to 700 nK in an optical lattice, *Phys. Rev. Lett.* 74 (1995) 1542.
- [145] D.R. Meacher, S. Guibal, C. Mennerat, J.-Y. Courtois, K.I. Petsas, G. Grynberg, Paramagnetism in a cesium optical lattice, *Phys. Rev. Lett.* 74 (1995) 1958.
- [146] C. Jurczak, K. Sengstock, R. Kaiser, N. Vansteenkiste, C.I. Westbrook, A. Aspect, Observation of intensity correlations in the fluorescence from laser cooled atoms, *Opt. Commun.* 115 (1995) 480.
- [147] C. Jurczak, J.-Y. Courtois, B. Desruelle, C.I. Westbrook, A. Aspect, Spontaneous light scattering from propagating density fluctuations in an optical lattice, *Eur. Phys. J. D* 1 (1998) 53.
- [148] C.I. Westbrook, The spectrum of light emitted by laser-cooled atoms, in: A. Aspect, W. Barletta, R. Bonifacio (Eds.), *Coherent and collective interactions of particles and radiation beams*, *Proceedings of the International School of Physics “Enrico Fermi”* 1995, Course CXXXI, North-Holland, Amsterdam, 1996, pp. 583–600.
- [149] L. Guidoni, B. Dépret, A. di Stefano, P. Verkerk, Atomic diffusion in an optical quasicrystal with five-fold symmetry, *Phys. Rev. A* 60 (1999) R4233.
- [150] G. Grynberg, P. Horak, C. Mennerat-Robilliard, Spatial diffusion of atoms cooled in a speckle field, *Europhys. Lett.* 49 (2000) 424.
- [151] G. Birkl, M. Gatzke, I.H. Deutsch, S.L. Rolston, W.D. Phillips, Bragg scattering from atoms in optical lattices, *Phys. Rev. Lett.* 75 (1995) 2823.

- [152] M. Weidemüller, A. Hemmerich, A. Görlitz, T. Esslinger, T.W. Hänsch, Bragg diffraction in an atomic lattice bound by light, *Phys. Rev. Lett.* 75 (1995) 4583.
- [153] M. Weidemüller, A. Görlitz, T.W. Hänsch, A. Hemmerich, Local and global properties of light-bound atomic lattices investigated by Bragg diffraction, *Phys. Rev. A* 58 (1998) 4647.
- [154] B. Lounis, P. Verkerk, J.-Y. Courtois, C. Salomon, G. Grynberg, Quantized atomic motion in 1D cesium molasses with magnetic field, *Europhys. Lett.* 21 (1993) 13.
- [155] A. Hemmerich, M. Weidemüller, T.W. Hänsch, Four-wave mixing in a 3D optical lattice, *Europhys. Lett.* 27 (1994) 427.
- [156] G. Grynberg, D. Boiron, J.-Y. Courtois, B. Lounis, D.R. Meacher, C. Salomon, P. Verkerk, Four-wave mixing and Bragg scattering in two and three-dimensional optical lattices, *Nonlinear Opt.* 12 (1995) 353.
- [157] J.M. Cowley, *Diffraction Physics*, North-Holland, Amsterdam, 1981.
- [158] G. Raithel, G. Birkel, A. Kastberg, W.D. Phillips, S.L. Rolston, Cooling and localization dynamics in optical lattices, *Phys. Rev. Lett.* 78 (1997) 630.
- [159] A. Görlitz, M. Weidemüller, T.W. Hänsch, A. Hemmerich, Observing the position spread of atomic wave packets, *Phys. Rev. Lett.* 78 (1997) 2096.
- [160] G. Raithel, G. Birkel, W.D. Phillips, S.L. Rolston, Compression and parametric driving of atoms in optical lattices, *Phys. Rev. Lett.* 78 (1997) 2928.
- [161] I.H. Deutsch, R.J.C. Spreeuw, S.L. Rolston, W.D. Phillips, Photonic band gaps in optical lattices, *Phys. Rev. A* 52 (1995) 1394.
- [162] C. Boisseau, J. Vigué, Laser-dressed molecular interactions at long range, *Opt. Commun.* 127 (1996) 251.
- [163] M.T. DePue, C. McKormick, S.L. Winoto, S. Oliver, D.S. Weiss, Unity occupation of sites in a 3D optical lattice, *Phys. Rev. Lett.* 82 (1999) 2262.
- [164] D.W. Sesko, T.G. Walker, C.E. Wieman, Behavior of neutral atoms in a spontaneous force trap, *J. Opt. Soc. Am. B* 8 (1991) 946.
- [165] A.M. Smith, K. Burnett, Analytical study of long-range collisions between two atoms undergoing laser cooling, *J. Opt. Soc. Am. B* 9 (1992) 1256.
- [166] K. Ellinger, J. Cooper, P. Zoller, Light-pressure force in N-atom systems, *Phys. Rev. A* 49 (1994) 3909.
- [167] Y. Castin, J.I. Cirac, M. Lewenstein, Reabsorption of light by trapped atoms, *Phys. Rev. Lett.* 80 (1998) 5305.
- [168] H. Kunugita, T. Ido, F. Shimizu, Ionizing collisional rate of metastable rare-gas atoms in an optical lattice, *Phys. Rev. Lett.* 79 (1997) 621.
- [169] J. Lawall, C. Orzel, S.L. Rolston, Suppression and enhancement of collisions in optical lattices, *Phys. Rev. Lett.* 80 (1998) 480.
- [170] M. Walhout, H.J.L. Megens, A. Witte, S.L. Rolston, Magneto-optical trapping of metastable xenon: Isotope-shift measurements, *Phys. Rev. A* 48 (1993) R879.
- [171] H. Katori, F. Shimizu, Laser-induced ionizing collisions of ultracold krypton gas in the $1s_5$ metastable state, *Phys. Rev. Lett.* 73 (1994) 2555.
- [172] M. Walhout, U. Sterr, C. Orzel, M. Hoogerland, S.L. Rolston, Optical control of ultracold collisions in metastable xenon, *Phys. Rev. Lett.* 74 (1995) 506.
- [173] G. Raithel, W.D. Phillips, S.L. Rolston, Magnetization and spin-flip dynamics of atoms in optical lattices, *Phys. Rev. A* 58 (1998) R2660.
- [174] K. Ensslin, T. Schlosser, *Phys. Scripta* T 66 (1996) 135.
- [175] D. Weiss, M.L. Roukes, A. Menschig, P. Grambow, K. von Klitzing, G. Weimann, Electron pinball and commensurate orbits in a periodic array of scatterers, *Phys. Rev. Lett.* 66 (1991) 2790.
- [176] R. Fleischmann, T. Geisel, R. Ketzmerick, Magnetoresistance due to chaos and nonlinear resonances in lateral surface superlattices, *Phys. Rev. Lett.* 68 (1992) 1367.
- [177] F. Nihey, S.W. Hwang, K. Nakamura, Observation of large $\hbar/2e$ oscillations in semiconductor antidot lattices, *Phys. Rev. B* 51 (1995) 4649.
- [178] B.L. Al'tshuler, A.G. Aranov, B.Z. Spivak, The Aaronov–Bohm effect in disordered conductors, *JETP Lett.* 33 (1981) 94.
- [179] G. Bergmann, Physical interpretation of weak localization: a time-of-flight experiment with conduction electrons, *Phys. Rev. B* 28 (1983) 2914.

- [180] A. Hemmerich, M. Weidemuller, T. Esslinger, C. Zimmerman, T.W. Hänsch, Trapping atoms in a dark optical lattice, *Phys. Rev. Lett.* 75 (1995) 37.
- [181] C. Triché, F. Chevy, G. Grynberg, Localization of cesium atoms on a three-dimensional lattice in momentum space, *Phys. Rev. A* 58 (1998) R38.
- [182] M. Rauner, S. Kuppens, M. Schiffer, G. Birkel, K. Sengstock, W. Ertmer, Atomic lattice structures in two-dimensional momentum space, *Phys. Rev. A* 58 (1998) R42.
- [183] M. Vallet, M. Pinard, G. Grynberg, Two-wave mixing with cross-polarized beams in Sodium: a quantitative investigation, *Opt. Commun.* 87 (1992) 340.
- [184] P. Van der Straten, S.-Q. Shang, B. Sheehy, H. Metcalf, G. Nienhuis, Laser cooling at low intensity in a strong magnetic field, *Phys. Rev. A* 47 (1993) 4160.
- [185] S.-Q. Shang, B. Sheehy, H. Metcalf, P. Van der Straten, G. Nienhuis, Velocity-selective resonances and sub-Doppler laser cooling, *Phys. Rev. Lett.* 67 (1991) 1094.
- [186] C. Valentin, M.-C. Gagné, J. Yu, P. Pillet, One-dimension sub-Doppler molasses in the presence of static magnetic field, *Europhys. Lett.* 17 (1992) 133.
- [187] M. Schiffer, M. Christ, G. Wokurka, W. Ertmer, Temperatures near the recoil limit in an atomic funnel, *Opt. Commun.* 134 (1997) 423.
- [188] Molecular motors, See the special issue of *Biophys. J.*, 1995.
- [189] F. Jülicher, A. Ajdari, J. Prost, Modeling molecular motors, *Rev. Mod. Phys.* 69 (1997) 1269 and references therein.
- [190] P. Curie, Sur la symétrie dans les phénomènes physiques, symétrie d'un champ électrique et d'un champ magnétique, *J. Phys. (Paris)* 3 (1894) 393.
- [191] C. Mennerat-Robilliard, D.M. Lucas, S. Guibal, J. Tabosa, C. Jurczak, J.-Y. Courtois, G. Grynberg, A ratchet for cold rubidium atoms: the asymmetric optical lattice, *Phys. Rev. Lett.* 82 (1999) 851.
- [192] J. Gierak, C. Vieu, M. Schneider, H. Launois, G. Ben Assayag, A. Septier, Optimization of experimental operating parameters for very high resolution focused ion beam applications, *J. Vac. Sci. Technol. B* 15 (1997) 2373.
- [193] M.A. McCord, D.P. Kern, T.H.P. Chang, Direct deposition of 10-nm metallic features with the scanning tunneling microscope, *J. Vac. Sci. Technol. B* 6 (1988) 1877.
- [194] K.S. Johnson, K.K. Berggren, A. Black, C.T. Black, A.P. Chu, N.H. Dekker, D.C. Ralph, J.H. Thywissen, R. Younkin, M. Tinkham, M. Prentiss, G.M. Whitesides, Using neutral metastable argon atoms and contamination lithography to form nanostructures in silicon, silicon dioxide, and gold, *Appl. Phys. Lett.* 69 (1996) 2773.
- [195] V.I. Balykin, V.S. Letokhov, The possibility of deep laser focusing of an atomic beam into the Å-region, *Opt. Commun.* 64 (1987) 151.
- [196] K.K. Berggren, M. Prentiss, G.L. Timp, R.E. Behringer, Calculation of atomic positions in nanometer-scale direct-write optical lithography with an optical standing wave, *J. Opt. Soc. Am. B* 11 (1994) 1166.
- [197] J.J. McClelland, Atom-optical properties of a standing-wave light field, *J. Opt. Soc. Am. B* 12 (1995) 1761.
- [198] T. Sleator, T. Pfau, V. Balykin, J. Mlynek, Imaging and focusing of an atomic beam with a large period standing light wave, *Appl. Phys. B* 54 (1992) 375.
- [199] G. Timp, R.E. Behringer, D.M. Tennant, J.E. Cunningham, M. Prentiss, K.K. Berggren, Using light as a lens for submicron, neutral-atom lithography, *Phys. Rev. Lett.* 69 (1992) 1636.
- [200] V. Natarajan, R.E. Behringer, D.M. Tennant, G. Timp, Nanolithography using a laser focused neutral atom beam, *J. Vac. Sci. Technol. B* 6 (1995) 2823.
- [201] J.J. McClelland, R.E. Scholten, E.C. Palm, R.J. Celotta, Laser-focused atomic deposition, *Science* 262 (1993) 877.
- [202] U. Drodofsky, J. Stuhler, B. Brezger, T. Schulze, M. Drewsen, T. Pfau, J. Mlynek, Nanometer-scale lithography with chromium atoms using light forces, *Microelectron. Eng.* 35 (1997) 285.
- [203] R.W. McGowan, D.M. Giltner, Siu Au Lee, Light force cooling, focusing and nanometer-scale deposition of aluminium atoms, *Opt. Lett.* 20 (1995) 2535.
- [204] K.K. Berggren, A. Bard, J.L. Wilbur, J.D. Gillapsy, A.G. Helg, J.J. McClelland, S.L. Rolston, W.D. Phillips, M. Prentiss, G.M. Whitesides, Microlithography by using neutral metastable atoms and self-assembled monolayers, *Science* 269 (1995) 1255.

- [205] B. Brezger, T. Schulze, U. Drodofsky, J. Stuhler, S. Nowak, T. Pfau, J. Mlynek, Nanolithography with neutral chromium and helium atoms, *J. Vac. Sci. Technol. B* 15 (1997) 2905.
- [206] S.J. Rehse, A.D. Glueck, S.A. Lee, A.B. Goulakov, C.S. Menoni, D.C. Ralph, K.S. Johnson, M. Prentiss, Nanolithography with metastable neon atoms: Enhanced rate of contamination resist formation for nanostructure fabrication, *Appl. Phys. Lett.* 71 (1997) 1427.
- [207] R. Younkin, K.K. Berggsen, K.S. Johnson, M. Prentiss, D.C. Ralph, G.M. Whitesides, Nanostructure fabrication in silicon using cesium to pattern a self-assembled monolayer, *Appl. Phys. Lett.* 71 (1997) 1261; F. Lison, H.-J. Adams, D. Haubrich, M. Kreis, S. Nowak, D. Meschede, Nanoscale atomic lithography with a cesium atom beam, *Appl. Phys. B* 65 (1997) 419.
- [208] R. Gupta, J.J. McClelland, M. Marte, R.J. Celotta, Raman-induced avoided crossings in adiabatic optical potentials: observation of $\lambda/8$ spatial frequency in the distribution of atoms, *Phys. Rev. Lett.* 76 (1996) 4689.
- [209] B. Brezger, Th. Schulze, P.O. Schmidt, R. Mertens, T. Pfau, J. Mlynek, Polarization gradient light masks in atoms lithography, *Europhys. Lett.* 46 (1999) 148.
- [210] R. Gupta, J.J. McClelland, Z.J. Jabbour, R.J. Celotta, Nanofabrication of a two-dimensional array using laser-focused atomic deposition, *Appl. Phys. Lett.* 67 (1995) 1378.
- [211] U. Drodofsky, J. Stuhler, Th. Schulze, M. Drewsen, B. Brezger, T. Pfau, J. Mlynek, Hexagonal structures generated by light masks for neutral atoms, *Appl. Phys. B* 65 (1997) 755.
- [212] W.R. Anderson, C.C. Bradley, J.J. McClelland, R.J. Celotta, Minimizing feature width in atom optically fabricated chromium nanostructures, *Phys. Rev. A* 59 (1999) 2476.
- [213] V. Sandoghdar, U. Drodofsky, Th. Schulze, B. Brezger, M. Drewsen, T. Pfau, J. Mlynek, Lithography using nano-lens arrays made of light, *J. Mod. Opt.* 44 (1997) 1883.
- [214] F.L. Moore, J.C. Robinson, C. Bharucha, P.E. Williams, M.G. Raizen, Observation of dynamical localization in atomic momentum transfer: A new testing ground for quantum chaos, *Phys. Rev. Lett.* 73 (1994) 2974.
- [215] J.C. Robinson, C. Bharucha, F.L. Moore, R. Jahnke, G.A. Georgakis, Q. Niu, M.G. Raizen, Study of quantum dynamics in the transition from classical stability to chaos, *Phys. Rev. Lett.* 74 (1995) 3963.
- [216] B.P. Anderson, M.A. Kasevich, Macroscopic quantum interference from atomic tunnel arrays, *Science* 282 (1998) 1686.
- [217] D.-I. Choi, Q. Niu, Bose-Einstein condensates in an optical lattice, *Phys. Rev. Lett.* 82 (1999) 2022.
- [218] S.K. Dutta, B.K. Teo, G. Raithel, Tunnelling dynamics and gauge potentials in optical lattices, *Phys. Rev. Lett.* 83 (1999) 1934.
- [219] D.L. Haycock, P.M. Alsing, I.H. Deutsch, J. Grondalski, P.S. Jessen, Mesoscopic quantum coherence in an optical lattice, *Phys. Rev. Lett.* 85 (2000) 3365.